

**AN INDUCTIVE POWER TRANSFER SYSTEM
WITH A HIGH-Q RESONANT TANK FOR
PORTABLE DEVICE CHARGING**

LI QIFAN

(B. Eng., XJTU, P.R. China)

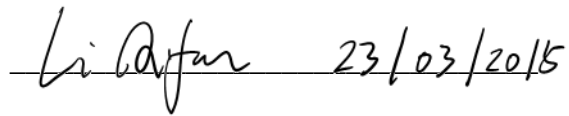
**A THESIS SUBMITTED
FOR THE DEGREE OF MASTER OF ENGINEERING
DEPARTMENT OF ELECTRICAL & COMPUTER
ENGINEERING
NATIONAL UNIVERSITY OF SINGAPORE**

2015

DECLARATION

I hereby declare that this thesis is my original work and it has been written by me in its entirety. I have duly acknowledged all the sources of information which have been used in the thesis.

This thesis has also not been submitted for any degree in any university previously.

Handwritten signature of Li Qifan and the date 23/03/2015, written in black ink over a horizontal line.

Li Qifan

23 March 2015

Acknowledgements

I would like to express my deepest gratitude to my supervisor Professor Liang Yung Chii, for his invaluable guidance, suggestions, and support throughout all my master's study and research. As his master's student, I am always appreciating the time and patience he spent on me. His passion and enthusiasm for research are of great inspiration to me during the master's time and will be a source of encouragement in my future study.

I am also grateful to lab officers Mr. Teo Thiam Teck of Power Electronics Lab, and Mr. Malcolm Hu of Keio-NUS CUTE Center for their kind help with equipment and material purchase.

I would like to thank my colleagues and friends, Dr. Huang Huolin, Mr. Wang Yun-Hsiang, Ms. Zhang Yuan, Mr. Sun Ruize, and Mr. Pan Xuewei, for their friendship. Life with them at NUS is full of joyful and pleasant memory. I would like to give my special thanks to my girlfriend, Ms. Yu Feiyu, who gave me a lot of accompany and encouragement when I was down.

Last but not least, I am very grateful to my parents Mr. Li Jinsheng and Mrs. Wang Liying for loving me, encouraging me and supporting me all the time.

Table of Contents

Declaration	i
Acknowledgements	ii
Table of Contents	iii
Summary	vi
List of Tables	viii
List of Figures	ix
List of Acronyms	xiii
Chapter 1 Background and Problem Definition	1
1.1 Background	1
1.2 Review on WPT for Portable Device Charging	3
1.3 Problem Definitions and Research Objectives	7
1.4 Thesis Contributions.....	9
1.5 Thesis Outline.....	10
Chapter 2 Theoretical Analysis of Inductive Power Transfer	12
2.1 Introduction	12
2.2 Ampère's Circuital Law and Faraday's Law of Induction	13
2.3 Magnetic Material Characteristics.....	15
2.4 RLC Resonant Circuit	18
2.5 Circuit Model of Coupled Inductors	23
2.5.1 General Coupled Inductors	23
2.5.2 Transformer.....	25
2.6 Reflected Impedance Model.....	28
2.7 Capacitive Compensation.....	31
2.7.1 Secondary Compensation.....	33
2.7.2 Primary Compensation.....	34
2.8 Energy Losses.....	36
2.8.1 Skin Effect	36

Table of Contents

2.8.2	Proximity Effect.....	39
2.8.3	Core Losses.....	40
2.9	Summary	42
Chapter 3 Design and Fabrication of the High-Q Resonant Coil.....		44
3.1	Introduction	44
3.2	Structure of the Resonant Coil	44
3.3	Circuit Analysis of the Resonant Coil	47
3.3.1	Current Distribution of the Resonant Coil.....	47
3.3.2	Equivalent Circuit Model for Unit Structure	50
3.3.3	Equivalent Circuit Model for Section Structure	53
3.3.4	Resonant Frequency of the Resonant Coil.....	54
3.4	Materials Selection	56
3.4.1	Conductor Layer	56
3.4.2	Dielectric Layer	57
3.4.3	Ferrite Core	59
3.5	Prototypes of the Resonant Coil.....	59
3.6	Summary	63
Chapter 4 Design and Construction of the IPT System		65
4.1	Introduction	65
4.2	Structure of the IPT System	66
4.3	Drive Circuit.....	67
4.3.1	Half-Bridge Circuit.....	67
4.3.2	Power MOSFETs	70
4.3.3	Gate Drive Circuit.....	70
4.4	Resonant Tank	71
4.5	Frequency Tracking Unit.....	72
4.5.1	Phase Properties of the Resonant Circuit.....	72
4.5.2	Phase-Locked Loop	73
4.5.3	PLL Chip.....	74
4.6	Standby Unit.....	79
4.7	Secondary Coil	81

4.8	Full-Wave Rectifier	82
4.9	DC/DC Converter.....	84
4.10	Summary	85
Chapter 5 Experimental Results and Discussion		87
5.1	Introduction	87
5.2	Hardware Implementation.....	87
5.3	System Testing.....	89
5.3.1	Testing of the Half-Bridge Circuit and the Resonant Tank..	89
5.3.2	Testing of the Frequency Tracking Unit	90
5.3.3	Testing of the Secondary Circuit.....	92
5.4	Efficiency of the IPT System	92
5.5	Evaluation of the IPT System.....	94
5.6	Summary	95
Chapter 6 Conclusions and Future Work.....		97
6.1	Conclusions	97
6.2	Future Work.....	98
References.....		100
List of Publications		107
Appendix.....		108

Summary

Wireless power transfer (WPT) has received great interest by researchers and industries since the beginning of 20th century. As the soaring market size for portable electronic and communication devices, WPT as a novel charging technology is applied due to many advantages. Inductive power transfer (IPT) as one of the wireless charging methods, which delivers energy from a primary side to a secondary side through an air gap by electromagnetic induction, is widely investigated. The main objective of this thesis is to build an IPT system with a specially designed resonant coil implemented, which has a significantly high quality factor (Q), to charge portable devices at high power transfer efficiency and good transmission capability.

Firstly, basic electromagnetic laws and circuit models for coupled inductors are introduced. Based on the analysis using the reflected impedance method, it is necessary to adopt capacitive compensation in both primary and secondary side and operate at the resonant frequency to achieve maximum power transfer efficiency and minimum VA rating of the supply.

Then, a novel design on the structure of resonant coil is proposed in order for high Q. To overcome the disadvantages of low Q and high cost of traditional resonant coil made of litz wire, the resonant coil has a structure of alternately stacked C-shaped conductor layers and toroid-shaped dielectric layers. The stack usually contains several repeating sections and only the top conductor layer of each section has terminals connected to the external circuit. According to the simulation results on current distribution, a lumped circuit model for the defined unit structure is established and used as a basic component to build the circuit model for the whole stack. Based on this model, the function between

resonant frequency and number of units is derived and verified by simulations and experiments. A 16-unit, 8-section resonant coil with a measured Q of 1200 at the resonant frequency of 550 kHz is prototyped and applied to the IPT system.

Next, the IPT system for portable device charging is designed. It consists of a primary circuit and a secondary circuit connected by inductive coupling. Energy from a DC power supply at the primary side is converted by a half-bridge circuit to a high-frequency magnetic field. The induced AC voltage across the secondary coil is converted to a DC voltage by a four-diode full-wave rectifier and further regulated by a DC/DC converter for a constant 5 V output. Both primary and secondary coils are compensated by capacitors to a same resonant frequency. A frequency tracking unit is implemented to cater the change of the resonant frequency to keep resonant status and a standby unit is implemented to reduce the power consumption when the secondary coil is absent.

Finally, the hardware is built on two separate PCBs, 5 W power can be delivered at the highest overall power transfer efficiency of 87% at the resonant frequency of 106 kHz. The proposed IPT system, which has a maximum air-gap distance to coil diameter ratio of 1.46, is compared with other related works to demonstrate effective power transfer for portable device charging.

List of Tables

Table 1.1 Comparison of different WPT technologies.....	2
Table 1.2. Market size for some portable electronic products [23].	4
Table 2.1. Skin depth of some conductive materials.	38
Table 3.1. Resistivity and skin depth of some common conductors.....	57
Table 3.2. Main properties of NOMEX [®] Type 410 insulation paper.....	59
Table 3.3. Main properties of EPCOS [®] N87 MnZn ferrite.....	59
Table 3.4. Main parameters of the resonant coil.....	59
Table 4.1. Dynamic electrical characteristics of IRF640N [71].	70
Table 4.2. Electrical properties of the secondary coil [75].	82

List of Figures

Fig. 1.1. Applications using WPT technology: (a) portable devices, (b) electric vehicles, (c) implantable devices, (d) underwater environment, (e) industrial environment, and (f) outer space.	3
Fig. 1.2. World markets revenue in WPT by application [26].	5
Fig. 1.3. Block diagram of an IPT system.	6
Fig. 2.1. Ampère's circuital law: (a) the magnetic \mathbf{B} field around current I , and (b) the line integral of the magnetic \mathbf{B} field around an arbitrary closed curve \mathcal{C}	13
Fig. 2.2. Magnetic flux density \mathbf{B} through a surface \mathcal{S} bounded by loop \mathcal{L} . ..	14
Fig. 2.3. The circular current I induced by the increasing magnetic flux produced by a moving magnet in the given direction.	15
Fig. 2.4. Magnetization curve of a typical ferromagnetic material.	18
Fig. 2.5. RLC resonant circuit: (a) series RLC, and (b) parallel RLC.	18
Fig. 2.6. The impedance of series RLC circuit versus frequency: (a) magnitude, and (b) phase.	19
Fig. 2.7. The magnitude of current flowing through a series RLC circuit versus frequency.	20
Fig. 2.8. Parallel RLC resonant circuit with non-negligible winding resistance.	21
Fig. 2.9. Circuit model for two coupled inductors.	24
Fig. 2.10. Equivalent T-circuit model for two coupled inductors.	25
Fig. 2.11. Circuit model for an ideal transformer.	26
Fig. 2.12. Circuit models for a real transformer.	27
Fig. 2.13. Circuit model for coupled windings using CCVS.	28
Fig. 2.14. Circuit model for coupled inductors using reflected impedance.	29

List of Figures

Fig. 2.15. Four types of compensating topologies: (a) SS, (b) SP, (c) PS, and (d) PP.....32

Fig. 2.16. Equivalent circuits using C CVS for (a) series secondary compensation, and (b) parallel secondary compensation.33

Fig. 2.17. Equivalent circuits with reflected impedance for (a) series primary compensation, and (b) parallel primary compensation.35

Fig. 2.18. Schematic diagram of current distribution in a cylindrical conductor caused by the skin effect, with dark color showing high current density.37

Fig. 2.19. Schematic diagram of current distribution in parallel cylindrical conductors caused by the proximity effect, with dark color showing high current density.40

Fig. 2.20. Eddy currents in (a) a solid core block, and (b) a laminated core. ..42

Fig. 3.1. Schematic diagram with exaggerated thickness of layers of the resonant coil.....45

Fig. 3.2. The structure of a section.....46

Fig. 3.3. The structure of a unit.....47

Fig. 3.4. Distributed RLC model for one section of the resonant coil.48

Fig. 3.5. Normalized magnitude of currents in two conductor layers of a unit versus angular position.49

Fig. 3.6. Normalized magnitude of current density per angle in the dielectric layer of a unit versus angular position.50

Fig. 3.7. Lumped circuit model for a unit.51

Fig. 3.8. Lumped circuit model for a section.....53

Fig. 3.9. Equivalent circuit for a resonant coil using reflected impedance.....54

Fig. 3.10. Parallel-plate capacitor.58

Fig. 3.11. The resonant frequency versus the number of coil units by theoretical calculations, simulations and experimental measurements.61

Fig. 3.12. The resonant frequency versus the number of coil units by theoretical calculations, simulations, experimental measurements, and adjusted simulations by decrease of self-inductance.62

Fig. 3.13. Photograph of a 16-unit resonant coil prototype.62

Fig. 3.14. Q of 1200 measured at the resonant frequency of 550 kHz.63

Fig. 4.1. Block diagram of the IPT system consisting of a primary circuit subsystem and a secondary circuit subsystem.66

Fig. 4.2. Half-bridge circuit with a series RLC load.....67

Fig. 4.3. Operating waveforms of the half-bridge circuit.68

Fig. 4.4. Operating status and current paths (red) of the half-bridge circuit: (a) Zone I ($t_0\sim t_1$), (b) Zone II ($t_1\sim t_2$), (c) Zone III ($t_2\sim t_3$), (d) Zone IV ($t_3\sim t_4$), (e) Zone V ($t_4\sim t_5$), and (f) Zone VI ($t_5\sim t_6$).68

Fig. 4.5. Input and output logic timing of IR2111.71

Fig. 4.6. Schematic diagram of the gate driver and the half-bridge with a series RLC load.....71

Fig. 4.7. Operating frequency versus the phase difference between the voltage source and capacitor in a series RLC circuit.....73

Fig. 4.8. Block diagram of the PLL.74

Fig. 4.9. Block diagram of the PLL chip CD4046B.75

Fig. 4.10. Input and output waveforms of the phase comparator I.75

Fig. 4.11. The average output voltage of the phase comparator I versus the input phase difference.76

Fig. 4.12. Passive, first-order low-pass RC filter.....76

Fig. 4.13. The VCO output frequency versus the input voltage (a) without offset, and (b) with offset.77

Fig. 4.14. The VCO output frequency versus the input phase difference (a) without offset, and (b) with offset.....77

Fig. 4.15. Combined characteristic curves of the resonant tank and the frequency tracking unit.78

Fig. 4.16. Schematic diagram of the standby unit.....79

Fig. 4.17. Operating waveforms of the dual-limit window comparator.....79

Fig. 4.18. Dimensions of the secondary coil (mm) [77].	81
Fig. 4.19. Photograph of the secondary coil.	81
Fig. 4.20. Full-wave rectifier: (a) bridge configuration using four diodes, and (b) input and output waveforms.	83
Fig. 4.21. The output waveform of the full-wave rectifier (black) and the waveform after smoothed (red).	84
Fig. 4.22. Schematic diagram of LM2576 for a fixed 5 V output.	85
Fig. 5.1. Photograph of the hardware implementation of the IPT system.	88
Fig. 5.2. Measured voltage waveforms of the high-side (upper trace, 5 V/div) and low-side (lower trace, 5 V/div) of the gate driver with a measured dead-time of 291.6 ns.	89
Fig. 5.3. Measured voltage waveforms across the resonant tank (upper trace, 10 V/div) and compensating capacitor (lower trace, 2 V/div), and the current waveforms (middle trace, 500 mA/div) through the resonant tank at time scale of 4 μ s/div.	90
Fig. 5.4. The VCO output frequency versus the phase difference between input voltages.	91
Fig. 5.5. The resonant frequency and the tracking frequency versus the coil distance.	91
Fig. 5.6. Measured AC voltage across the secondary coil (upper trace, 5 V/div) and DC voltage across the output of DC/DC converter (lower trace, 5 V/div) at the time scale of 4 μ s/div.	92
Fig. 5.7. The coupling efficiency and the overall power transfer efficiency versus the coil distance.	93
Fig. 5.8. Load power versus the distance between two coils.	94
Fig. 5.9. The comparison of the maximum power efficiency and transmission distance ratio with related works from [80]-[87].	95

List of Acronyms

AC	Alternating Current
CCVS	Current-Controlled Voltage Source
DC	Direct Current
emf	Electromotive Force
IPT	Inductive Power Transfer
LF	Loop Filter
PD	Phase Detector
PLL	Phase-Locked Loop
Q	Quality Factor
VCO	Voltage-Controlled Oscillator
WPC	Wireless Power Consortium
WPT	Wireless Power Transfer
ZCS	Zero Current Switching
ZVS	Zero Voltage Switching

Chapter 1

Background and Problem Definition

1.1 Background

Wireless power transfer (WPT) is a power transmission technology to transfer electrical power from a power source to an electrical load without using solid wires or conductors. It has continuously attracted interest from both academic and industrial communities since 19th centuries. In 1862 James Clerk Maxwell derived Maxwell's equation which is the basis for modern electromagnetics, and in 1884 John Henry Poynting developed equations for the flow of power in an electromagnetic field. At the turn of the 20th century, Serbian-American inventor Nikola Tesla performed the first experiment in WPT and successfully demonstrated the use of a pair of coils to wirelessly power a lighting device [1]. In 1901, Tesla began construction of a large high-voltage coil facility, the Wardenclyffe Tower at Shoreham, New York, intended as a prototype transmitter for a "World Wireless System" which was to transmit power worldwide, but by 1904 his investors had pulled out, and the facility was never completed. The modern history of WPT began with the Raytheon Airborne Microwave Platform (RAMP) Project initiated by the US Army in the 1950's. The project was led to a demonstration of a helicopter platform which flew at an altitude of 18 m while being powered exclusively through a microwave beam from the ground [2]. In the past few decades, a considerable amount of research has been done in the field of WPT. There are two distinct

scenarios for WPT, namely near field and far field. The near field is referred to as a non-radiative type which occurs at a distance smaller than one wavelength between the transmitter and receiver, while the far field is considered to be a radiative type which propagates starting from a distance equal to two wavelengths to infinity between the transmitter and receiver. Different technologies are used for WPT in these two regions. As for near field, inductive coupling, capacitive coupling and magnetodynamic coupling are mainly applied. For far field, microwaves and lasers are utilized. Table 1.1 compares the features of these technologies. Since the 1990s, near field WPT systems have been widely investigated, particularly for applications in charging electric vehicles [3-10] and portable equipment, such as laptop computers [11-12] and mobile phones [13-22]. Fig. 1.1 shows various applications using WPT technology nowadays.

Table 1.1 Comparison of different WPT technologies.

Technology	Range	Frequency	Antenna devices
Inductive coupling	Short	Hz-MHz	Wire coils
Capacitive coupling	Short	kHz-MHz	Electrodes
Magnetodynamic	Short	Hz	Rotating magnets
Microwaves	Long	GHz	Parabolic dishes, phased arrays, rectennas
Light waves	Long	\geq THz	Laser, photocells, lenses, telescopes

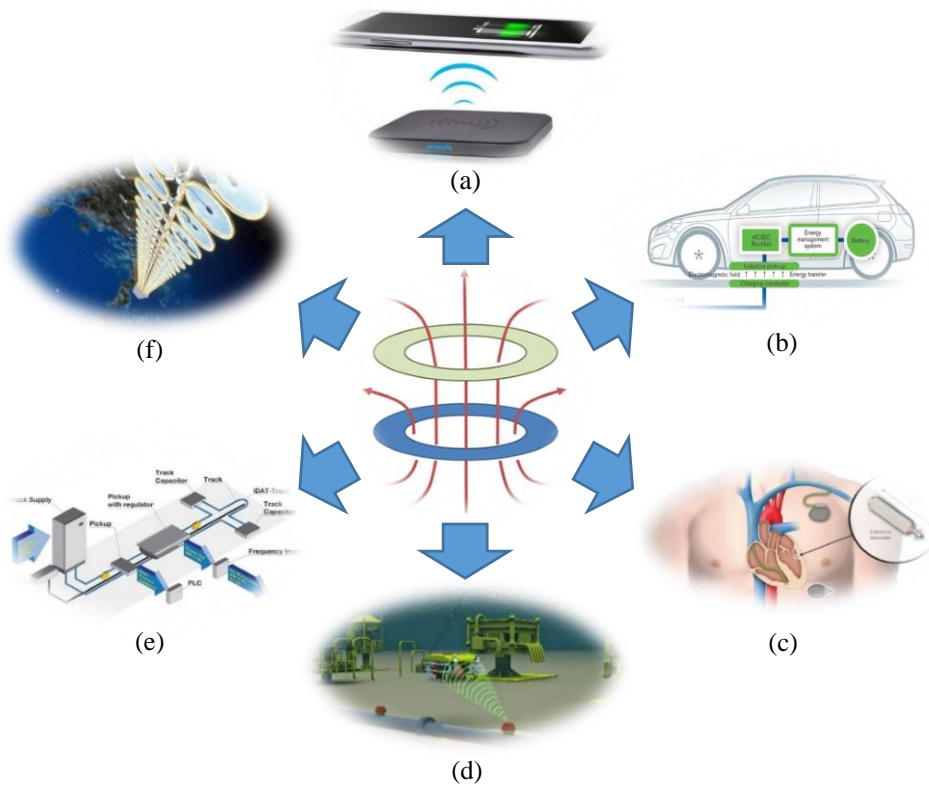


Fig. 1.1. Applications using WPT technology: (a) portable devices, (b) electric vehicles, (c) implantable devices, (d) underwater environment, (e) industrial environment, and (f) outer space.

1.2 Review on WPT for Portable Device Charging

The dawn of portable electronic and communication devices since the 1980s has brought huge benefits to human society [23]. A variety of portable devices, such as smart phones, Bluetooth headsets and tablet computers, have come out in the last ten years. The market size for a range of portable electronic products from 2009 to 2016 are shown in Table 1.2. Among these portable electronic products, the market size of mobile phones alone is expected to exceed 2.2 billion by 2015, which is over 50% growth of that in 2009. The emergence of tablets also accelerates the market expansion of portable electronic products.

Table 1.2. Market size for some portable electronic products [23].

Portable Products	Market Size (Million Units)							
	2009	2010	2011	2012	2013	2014	2015	2016
Mobile Phones	1421	1696	1841	1963	2069	2160	2236	2291
Bluetooth Headsets	62	65	45	50	60	85	110	150
Tablets	0	16.7	60	90	130	185	241	300
Notebook Computers	135	164	189	210	232	280	315	380
Digital Cameral	120	118	127	131	140	145	159	169
Portable DVD	22	20	27	32	28	34	38	43
Nintendo DS	31	27	17	14	12	10	10	10
PSP	16	14	9	15	18	18	18	18

However, booming consumption on portable battery-powered products with private chargers comes along with an increasing electronic waste issue [24]. Great efforts have been made by the Groupe Speciale Mobile Association (GSMA) in promoting the use of micro-USB to standardize the cord-based charging interface. Besides the standard cord-based charging option, WPT technology has emerged as an attractive and user-friendly solution to a common charging platform for a wide range of portable devices. It offers advantages such as minimum or no external charging accessories, availability for multiple devices simultaneously and a lower risk of electric shock in harsh environment. Such advantageous features have attracted over 135 worldwide companies to form the Wireless Power Consortium (WPC), which launched the first interface standard “Qi” for wireless charging in 2009 [25]. It marks that WPT technology for portable device charging has reached commercialization stage. So far, WPT has grown from a fledgling technological case to a \$1 billion industry around the world [26] and the world markets for WPT—encompassing mobile devices, consumer electronics, industrial applications, infrastructure devices and electric vehicles—will triple over the next few years, growing from \$4.9 billion in

revenue in 2012 to \$15.6 billion in 2020, according to a report by Pike Research as shown in Fig 1.2 [26].

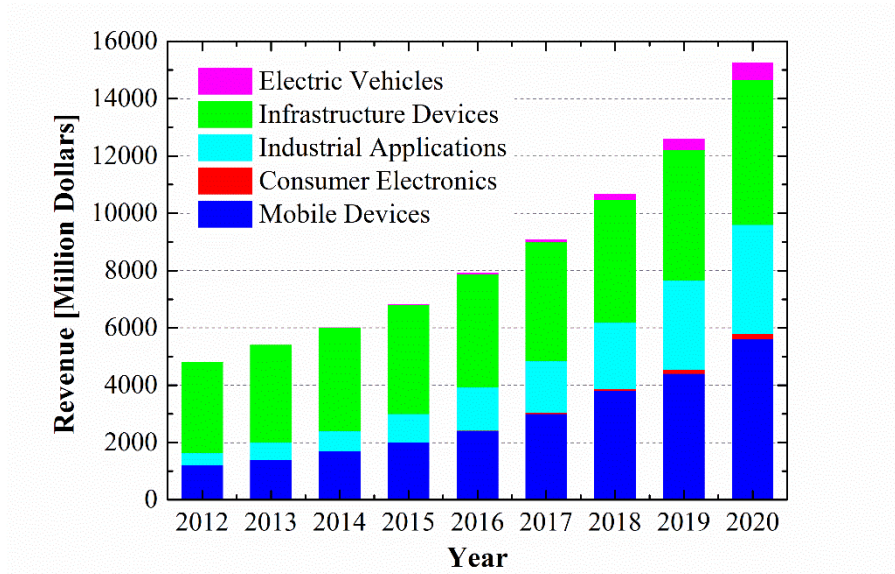


Fig. 1.2. World markets revenue in WPT by application [26].

In all near-field WPT technologies thus far, energy is coupled from a primary side to a secondary side through an air gap. Especially in inductive power transfer (IPT) systems, energy is transferred between inductively coupled windings based on the principle of electromagnetic induction. An IPT system is essentially a specially structured transformer which contains two or more windings separated by air gaps instead of wrapped around a closed magnetic core in a conventional transformer. When a varying current flows in the primary winding, a varying magnetic flux is created throughout the winding and impinges on the secondary winding. The varying magnetic flux induces a varying electromotive force in the secondary winding. Thus, the energy consumed by the load on the secondary side is from that of the source output on the primary side which flows through the transmitter circuit, the air gap and the receiver circuit, and finally reaches the load. A typical IPT system is illustrated in Fig. 1.3.

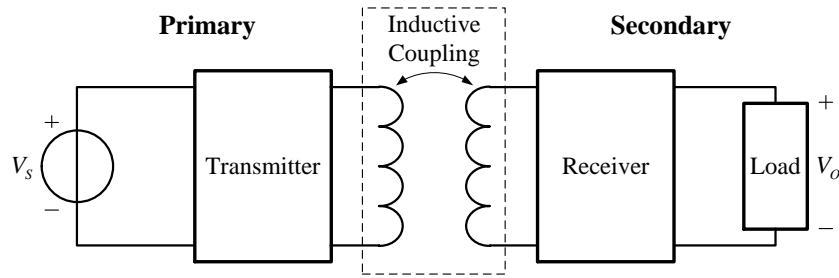


Fig. 1.3. Block diagram of an IPT system.

The overall efficiency of the IPT system greatly depends on the capability of energy transmission from the primary winding to the secondary winding. Due to a separation between these two windings, a larger portion of the magnetic flux generated by the primary winding cannot be received by the secondary winding. The portion will significantly increase if the windings are placed far apart or aligned with an angle. Therefore, the overall efficiency of IPT systems is not high when a large separation between the primary winding and the secondary winding exists.

In order to increase the overall efficiency of IPT systems, researchers focus on two main aspects. One is to improve the design of windings [27-48]. For example, a uniform magnetic field distribution in a planar wireless charging platform contributes to small efficiency discrepancy between best and worst positions of secondary windings. As for the shape of planar windings, X. Liu investigated the magnetic field distribution of both circular structure and rectangular structure [27]. W. X. Zhong derived optimal dimensional relationship between the planar transmitter winding array and the receiver winding to achieve effective area coverage [28]. U. M. Jow presented an optimal design methodology for an overlapping hexagonal planar winding array for creation of a homogenous magnetic field [29]. The structure of magnetic core is also an important part of coil design. Pot type [30], plate type [31], bar type [33], cylinder type [32], E type [34], loop type [35] and dipole type [36] of ferrite cores are implemented in different applications to maximize power

transmission efficiency, respectively. Besides magnetic structure, enhanced magnetic material is a topic in IPT [48].

The other aspect is to improve the circuit design of IPT systems [49-61]. In an IPT system, compensating circuits are always implemented in primary and secondary to achieve resonant status. Characteristics of different structures of compensating capacitors are presented and their influence on power transmission efficiency is analyzed [49-51]. In [51], Q. W. Zhu proposed a method to optimize four compensating capacitors used in a 3.3 kW IPT system for electric vehicle. The structure of four compensating capacitors were also used by R. Azambuja [52] and their value were computed using a search algorithm based on Monte Carlo, which significantly improved the efficiency and output power. Moreover, an IPT system is typically operated at from several hundred kHz up to tens of MHz. Therefore, soft switching technique contributes greatly to the decrease of switching losses. Zero voltage switching (ZVS) or zero current switching (ZCS) is widely applied in many applications [54-58].

1.3 Problem Definitions and Research Objectives

Unlike charging with wires, the design of an IPT system has many special considerations. Major requirements for an IPT system for portable device charging applications are summarized as follows:

- 1) **High efficiency:** Power transfer efficiency is the most important parameter and determines the performance of an IPT system. High power transfer efficiency is a basic requirement.
- 2) **High transmission capability:** Higher transmission capability means further transmission distance with the same coil dimension. It is a

typical feature of wireless charging and useful when a large air gap between the primary and secondary coil exists.

- 3) Operating at resonance: At resonant status, a strong magnetic field links the primary and secondary coil so that energy is transferred from the source to the load to its greatest extent.
- 4) Coil aligning: Guided positioning uses magnetic attraction to align and fix the secondary coil with the primary coil. Free positioning uses either a mechanically movable primary coil underneath the surface of charging platform, or a primary winding array to align an arbitrarily placed secondary coil.
- 5) Low weight and small volume suitable for embedded in portable devices.
- 6) Low cost and easy fabrication.

In existing research, coils implemented are made of litz wire, which usually have a quality factor (Q) of several hundred. It limits both power transfer efficiency and fabrication cost. Moreover, resonance are not effectively preserved when operating conditions, such as the distance between the primary and secondary coils, change. To overcome these disadvantages, this research has the following specific objectives:

- 1) Design a novel structure of resonant coil to achieve a significantly high value of Q . Based on simulations and circuit analysis, prototypes are fabricated to verify predicted properties.
- 2) Design an IPT system with the proposed high- Q resonant coil implemented for portable device charging applications. It has both a high power transfer efficiency and a good transmission capability.

- 3) Apply a frequency control unit in the IPT system to maintain resonant status by adjusting the operating frequency following the varying resonant frequency when working conditions change.
- 4) Apply a standby unit in the IPT system to minimize energy consumption when the secondary side is absent.

1.4 Thesis Contributions

The major contributions of the thesis are summarized as follows:

- 1) A novel design on the structure of resonant coil is proposed. This new structure is a stack of thin conductor and dielectric layers filling the winding area of an open pot core. It helps greatly to increase the Q of resonant coil over 1000, which is significantly higher than the Q of several hundred of conventional windings made of litz wire. It reduces the fabrication cost of the resonant coil, since litz wire is more expensive than cooper sheets to mitigate the skin effect and proximity effect losses, especially when the strand diameter is required below 50 μm at high frequencies of MHz.
- 2) An IPT system for portable device charging application is proposed. The system consists of a primary circuit subsystem and a secondary circuit subsystem, both compensated by capacitors in order to maximize the power transfer efficiency at the resonant frequency. A frequency tracking unit is implemented in the primary circuit to tune the operating frequency following the varying resonant frequency, which is caused by changing working conditions. With the specially designed resonant coil applied in the primary circuit, energy can be transferred from the primary side to the secondary side at a high

efficiency when resonance occurs, and the capability of transmission distance, defined as the ratio of the maximum transmission distance to the coil dimension, is better than most of other IPT systems.

1.5 Thesis Outline

The thesis is divided into six chapters. The layout of the thesis is given as follows.

In Chapter 2, the fundamental electromagnetic theory of IPT, including Ampère's circuital law and Faraday's law of induction, and the characteristics of ferromagnetic materials are introduced. Circuit analysis for basic RLC resonant circuits and coupled inductors are presented. The reflected impedance approach used for solving coupled inductors suggests that capacitive compensation are needed to increase the power transfer efficiency. Therefore, four types of capacitive compensating topologies are proposed and equations for choice of the values of compensating capacitors are derived, respectively. Losses in real coupled inductors, including skin effect, proximity effect and magnetic core, are introduced and approaches to diminish these losses are also discussed.

In Chapter 3, a novel design on the structure of high-Q resonant coil is comprehensively introduced. Based on the proposed stacked topology, simulations are performed to investigate the current distribution in conductor layers and dielectric layers. According to the simulation results, the distributed circuit model for the resonant coil can be simplified by using a lumped circuit model. With this lumped circuit model, the formula of resonant frequency of the resonant coil is derived. Prototypes are fabricated using copper sheets,

insulation paper and high-permeability ferrite cores, and are measured to verify the resonant frequency and effectively high Q.

In Chapter 4, the IPT system for portable device charging is designed. It consists of a primary subsystem and a secondary subsystem. In the primary circuit, a DC voltage is converted to a high-frequency square wave by the half-bridge inverter, and then the square-wave voltage is applied across the resonant tank. The operating frequency is controlled by a frequency tracking unit to ensure that the resonant status is always maintained. In the secondary circuit, the induced AC voltage across the secondary coil is converted to a pulsating DC voltage by a full-wave rectifier and regulated by a DC/DC converter, resulting in a constant and suitable DC voltage for charging. Moreover, a standby mode is designed to minimize energy consumption when the secondary side is absent. For the whole system, design considerations and chip selections are introduced in detail.

In Chapter 5, a prototype of the proposed IPT system for portable device charging is presented. Modules of the system are tested and evaluated based on their waveforms. The performance of frequency tracking unit and the efficiency, including overall power transfer efficiency and coupling efficiency, are measured when the distance between the primary and secondary coil varies. Finally, comparisons between the proposed system and other IPT works are made according to the power transfer efficiency and transmission distance capability.

Chapter 6 gives a summary of the thesis and possible further works to do in the future.

Chapter 2

Theoretical Analysis of Inductive Power Transfer

2.1 Introduction

This chapter mainly focuses on the theoretical analysis of IPT. In Section 2.2, two basic laws in classical electromagnetism, Ampère's circuital law and Faraday's law of induction, are briefly reviewed. The magnetic characteristics of substances and the magnetization curve of ferromagnetic materials are introduced in Section 2.3. Then, in Section 2.4, basic RLC resonant circuits, including series RLC and parallel RLC, are analyzed and parameters describing their characteristics are defined. Next, in Section 2.5, circuit models for coupled inductors are presented, including ideal transformer model and real transformer model. In Section 2.6, a reflected impedance method to solving coupled inductors is given. Based on this method, factors influencing on the power transfer efficiency are investigated. In Section 2.7, four types of capacitive compensating circuit are introduced respectively and equations for choice of the values of compensating capacitors are derived. Finally, in Section 2.8, losses of IPT systems resulting from skin effect, proximity effect and magnetic core are presented and approaches to diminish these losses are also discussed. This chapter is concluded in Section 2.9.

2.2 Ampère's Circuital Law and Faraday's Law of Induction

There are two basic laws which lay the theoretical foundation of IPT. These laws are termed as Ampère's circuital law and Faraday's law of induction, which are part of Maxwell's equations [62].

In classical electromagnetism, Ampère's circuital law, discovered by André-Marie Ampère in 1826, relates magnetic fields to electric currents which produce them. Ampère's circuital law can be written in two forms, the integral form and the differential form, which are equivalent by the Kelvin-Stokes theorem. In its integral form, Ampère's circuital law is a line integral of the magnetic field around an arbitrary closed curve \mathcal{C} . The curve \mathcal{C} in turn bounds a surface \mathcal{S} which the electric current passes through, and encloses the current. As shown in Fig. 2.1, the line integral of the magnetic \mathbf{B} field around the closed curve \mathcal{C} is proportional to the total current $\sum I$ passing through the surface \mathcal{S} enclosed by \mathcal{C} :

$$\oint_{\mathcal{C}} \mathbf{B} \cdot d\boldsymbol{\ell} = \mu_0 \iint_{\mathcal{S}} \mathbf{J} \cdot d\mathbf{S} = \mu_0 \sum I, \quad (2.1)$$

where \mathbf{J} is the free current density, and μ_0 is the magnetic constant.

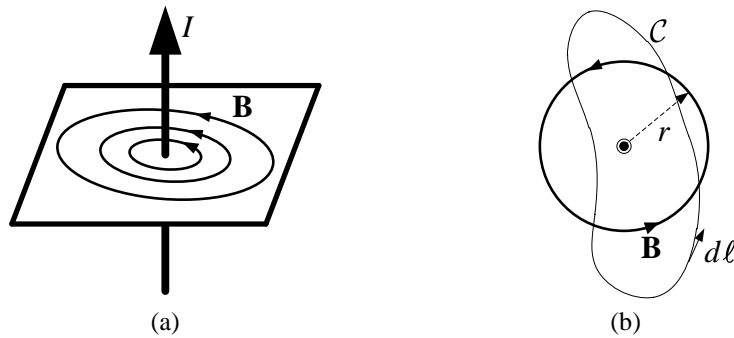


Fig. 2.1. Ampère's circuital law: (a) the magnetic \mathbf{B} field around current I , and (b) the line integral of the magnetic \mathbf{B} field around an arbitrary closed curve \mathcal{C} .

Consider an infinite straight wire in vacuum shown in Fig. 2.1 as a special case. The current is coming out of the page. Due to symmetry, the magnetic field lines are concentric circles in planes perpendicular to the wire and are in the direction the fingers of the right hand curl if the wire was wrapped by them with the thumb in the direction of the current. Suppose that the closed curve \mathcal{C} is a circle of radius r centered on the wire. The magnetic flux density can be calculated by the line integral:

$$\oint_{\mathcal{C}} \mathbf{B} \cdot d\boldsymbol{\ell} = 2\pi r B = \mu_0 I, \quad (2.2)$$

$$B = \frac{\mu_0 I}{2\pi r}. \quad (2.3)$$

According to (2-3), we can easily conclude that the magnetic flux density \mathbf{B} around an infinite straight wire in vacuum is proportional to the current I and inversely proportional to the distance r .

Faraday's law of induction, as a basic law of electromagnetism, implies that an electromotive force, also called emf, is induced in any closed circuit by a time-varying magnetic flux through the circuit. This phenomenon is called electromagnetic induction. Faraday's law of induction makes use of the magnetic flux Φ through a hypothetical surface \mathcal{S} whose boundary is a wire loop \mathcal{L} shown in Fig. 2.2. The magnetic flux is defined by a surface integral:

$$\Phi = \iint_{\mathcal{S}} \mathbf{B} \cdot d\mathbf{S}. \quad (2.4)$$

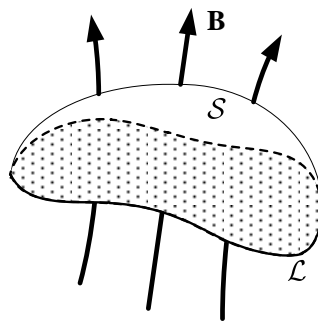


Fig. 2.2. Magnetic flux density \mathbf{B} through a surface \mathcal{S} bounded by loop \mathcal{L} .

The induced emf ε is proportional to the rate of change of the magnetic flux:

$$\varepsilon = -\frac{d\Phi}{dt}. \quad (2.5)$$

The direction of the induced current caused by the emf is given by Lenz's law, which indicates that the magnetic field produced by the induced current opposes the original change in magnetic flux. As an example in Fig 2.3, the movement of the magnet in the given direction will increase the magnetic flux through the conductor loop and induce a circular current whose magnetic field is in the opposite direction to prevent the increasing.

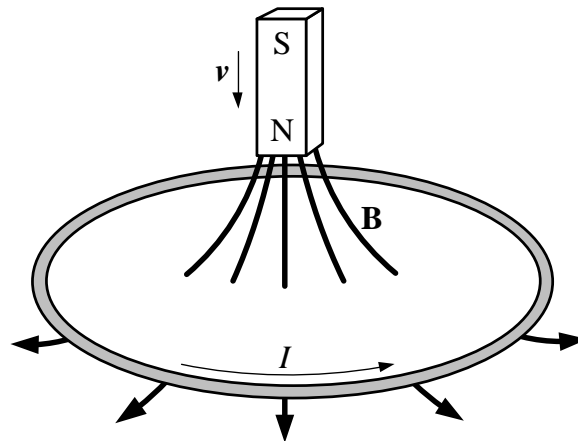


Fig. 2.3. The circular current I induced by the increasing magnetic flux produced by a moving magnet in the given direction.

2.3 Magnetic Material Characteristics

All materials are influenced to some extent by a magnetic field. The overall magnetic behavior of a material can vary widely. Several forms of magnetic behavior have been observed in different materials, including:

- Ferromagnetic and ferrimagnetic materials are attracted to a magnet strongly enough that the attraction can be felt. These materials can

retain magnetization and become magnets even if the magnetic field is withdrawn. Common ferromagnetic materials are iron, nickel cobalt, their alloys, and some alloys of rare earth metals.

- Paramagnetic materials, such as platinum, aluminum and oxygen, are weakly attracted to either pole of a magnet. This attraction is hundreds of thousands of times weaker than that of ferromagnetic materials.
- Diamagnetic substances are repelled by both poles. Compared to paramagnetic and ferromagnetic substances, diamagnetic substances, such as carbon, copper, water and plastic, are even more weakly repelled by a magnet. The permeability of diamagnetic materials is less than the permeability of vacuum.

Ferromagnetic materials play a vital role in a wide variety of applications, such as magnetic recording media, speakers, electric motors, medicine and so on. In the context of electromechanical energy conversion devices, the importance of magnetic materials is twofold. One is to obtain large magnetic flux densities with relatively low levels of magnetizing force. Since magnetic force and energy density increase with increasing flux density, this feature is of great importance in the performance of energy conversion devices. The other is to constrain and direct magnetic fields in well-defined paths. In a transformer, they are used to direct magnetic flux to maximize the coupling between windings. In an electric machine, magnetic materials are used to shape the field to obtain desired torque production.

When an external magnetic field is applied to a ferromagnet, the domain magnetic moments tend to align with the applied field [63]. As a result, the domain magnetic moments add to the applied field, producing a much larger value of flux density than that produced by magnetizing force alone. The effective permeability μ , equal to the ratio of the magnitude of total magnetic

flux density \mathbf{B} to the magnitude of applied magnetic field strength \mathbf{H} , is much larger than compared with the permeability of free space μ_0 . As the magnetizing force is increased, this behavior continues until all the magnetic moments are aligned with the applied field; at this point they can no longer contribute to increasing the magnetic flux density, and the ferromagnet is said to be fully saturated.

When the applied magnetic field is reduced to zero, although domain magnetic moments tend to relax towards their initial orientation, the magnetic dipole moments will no longer be totally random in their orientation and they will retain a net magnetization component along the applied field direction, which is called remanence and denoted as B_r .

When the magnetic field in the opposite direction is applied and increased gradually, the magnetic dipole moments will disorder further and become totally random at some point, where the intensity of the applied magnetic field is called coercivity and denoted as H_c .

The above phenomenon is known as magnetic hysteresis. Due to this hysteresis, the relationship between magnetic flux density \mathbf{B} and magnetic field strength \mathbf{H} for ferromagnetic material is both nonlinear and multivalued. Starting at the origin, the upward dash curve is the initial magnetization curve. The initial magnetization curve increases rapidly at first and then approaches an asymptote called magnetic saturation. If the applied magnetic field changes from one direction to the opposite, then back to the original direction, and the strength of the field varies in a cycle, the H-B curve will form a hysteresis loop, called the main loop, shown in Fig. 2.4. The intercepts of the main loop are remanence B_r and coercivity H_c , respectively.

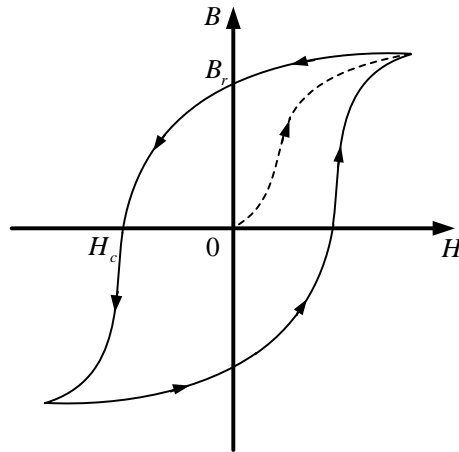


Fig. 2.4. Magnetization curve of a typical ferromagnetic material.

2.4 RLC Resonant Circuit

Electrical resonance occurs in an electric circuit at some particular frequencies, named resonant frequencies, when the imaginary parts of impedances or admittances of circuit elements cancel each other. The simplest resonant circuit is an RLC resonant circuit consisting of a resistor R , an inductor L , and a capacitor C . These three components are connected in series or in parallel, called series RLC circuit or parallel RLC circuit respectively, as shown in Fig. 2.5.

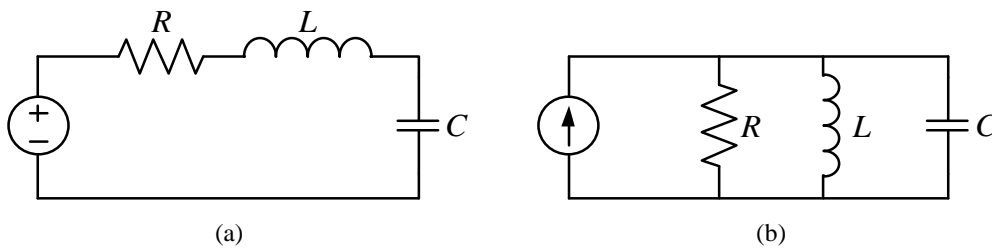


Fig. 2.5. RLC resonant circuit: (a) series RLC, and (b) parallel RLC.

In the series RLC resonant circuit of Fig. 2.5(a), the total impedance seen from the AC voltage source can be calculated as:

$$Z = R + j\omega L + \frac{1}{j\omega C} = R + j\left(\omega L - \frac{1}{\omega C}\right). \quad (2.6)$$

Its magnitude $|Z|$ and phase θ are:

$$|Z| = \sqrt{R^2 + \left(\omega L - \frac{1}{\omega C}\right)^2}, \quad (2.7)$$

$$\theta = \arctan\left(\frac{\omega L - \frac{1}{\omega C}}{R}\right). \quad (2.8)$$

According to the definition of resonant frequency, the resonant frequency of the series RLC circuit $f_{0,s}$ can be derived as:

$$f_{0,s} = \frac{1}{2\pi\sqrt{LC}}. \quad (2.9)$$

The relationships between the magnitude of impedance and frequency, and between the phase of impedance and frequency are shown in Fig. 2.6.

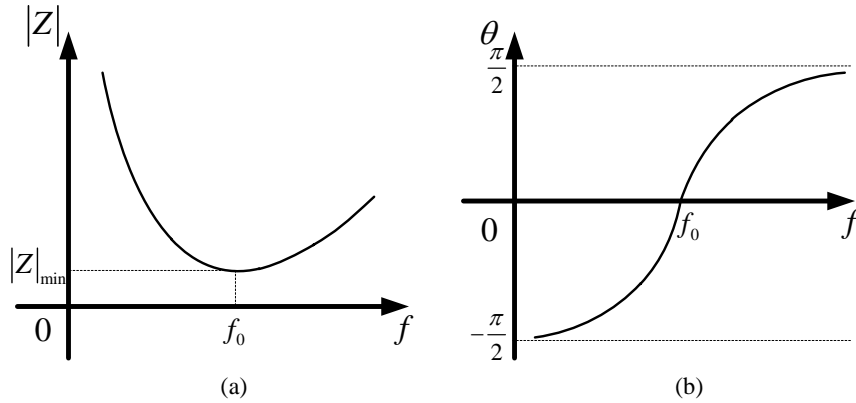


Fig. 2.6. The impedance of series RLC circuit versus frequency: (a) magnitude, and (b) phase.

Thus, the magnitude of current flowing through the series circuit is also a function of frequency:

$$|I| = \frac{|V_s|}{|Z|} = \frac{|V_s|}{\sqrt{R^2 + \left(\omega L - \frac{1}{\omega C}\right)^2}}. \quad (2.10)$$

At the resonant frequency, the current gets its maximum value as:

$$|I|_{\max} = \frac{|V_s|}{R}. \quad (2.11)$$

The relationship between the magnitude of current and frequency is shown in Fig. 2.7.

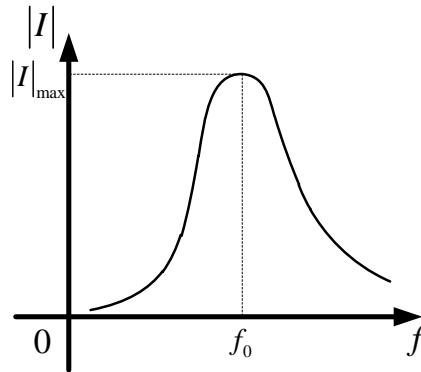


Fig. 2.7. The magnitude of current flowing through a series RLC circuit versus frequency.

Similarly, in the parallel RLC resonant circuit of Fig. 2.5(b), the total admittance seen from the AC current source can be calculated as:

$$Y = G + j\omega C + \frac{1}{j\omega L} = G + j\left(\omega C - \frac{1}{\omega L}\right), \quad (2.12)$$

where G is the conductance. The resonant frequency of the parallel RLC circuit $f_{0,P}$ can be derived as:

$$f_{0,P} = \frac{1}{2\pi\sqrt{LC}}, \quad (2.13)$$

which equals to that of series RLC resonant circuit. At resonant frequency, the voltage across the parallel circuit gets its maximum value as:

$$|V|_{\max} = \frac{|I_s|}{G}. \quad (2.14)$$

As for a parallel RLC resonant circuit, if the resistance of winding R_L is considered as shown in Fig. 2.8, the total admittance seen from the AC current source is:

$$\begin{aligned}
 Y &= \frac{1}{R} + j\omega C + \frac{1}{R_L + j\omega L} \\
 &= \left(\frac{1}{R} + \frac{R_L}{R_L^2 + \omega^2 L^2} \right) + j \left(\omega C - \frac{\omega L}{R_L^2 + \omega^2 L^2} \right)
 \end{aligned}
 \tag{2.15}$$

Thus, the resonant frequency is given by:

$$\begin{aligned}
 f_{0,P} &= \frac{1}{2\pi} \sqrt{\frac{1}{LC} - \left(\frac{R_L}{L} \right)^2} \\
 &= \frac{1}{2\pi} \sqrt{\frac{L - R_L^2 C}{L^2 C}}
 \end{aligned}
 \tag{2.16}$$

The resonance happens only if $L > R_L^2 C$. When

$$\sqrt{\frac{L}{C}} \gg R_L,
 \tag{2.17}$$

the resonant frequency approximately equals to that of the parallel RLC resonant circuit without winding resistance, i.e.,

$$f_{0,P} = \frac{1}{2\pi\sqrt{LC}}.
 \tag{2.18}$$

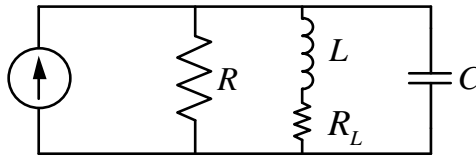


Fig. 2.8. Parallel RLC resonant circuit with non-negligible winding resistance.

The essence of resonance is that energy in a system is stored and transferred easily between two or more different storage modes. For example, in a RLC resonant circuit, resonance occurs because energy is stored in two different ways: in an electric field as the capacitor is charged and in a magnetic field as current flows through the inductor. At resonant status, energy oscillates

significantly back and forth between the capacitor and the inductor within the circuit. The resistance in the circuit damps the oscillation so that energy is dissipated as heat in the resistance per cycle. A physical quantity is to create to describe this characteristic.

The quality factor, Q , is a dimensionless parameter to describe how under-damped an oscillator or resonator is. It is defined in term of the ratio of the peak energy stored in the circuit to the average energy dissipated in it per cycle at resonance:

$$\begin{aligned} Q &= 2\pi \times \frac{\text{Energy stored}}{\text{Energy dissipated per cycle}} \\ &= 2\pi f_0 \times \frac{\text{Energy stored}}{\text{Power loss}} \end{aligned} \quad (2.19)$$

In a series RLC resonant circuit, at its resonant frequency, the average power dissipated by the resistor is given by:

$$P_s = R|I_0|^2, \quad (2.20)$$

where I_0 is the current flowing in the circuit at resonance. The maximum energy stored in the circuit is given by:

$$E_s = L|I_0|^2. \quad (2.21)$$

Thus, the Q factor is:

$$Q = \frac{\omega_0 L}{R}, \quad (2.22)$$

where ω_0 is the resonant angular frequency, and the Q factor is inversely proportional to the resistance R .

Similarly, in a parallel RLC resonant circuit, at its resonant frequency, the average power dissipated by the resistor is given by:

$$P_p = G|V_0|^2, \quad (2.23)$$

where V_0 is the voltage across the resistor at resonance. The maximum energy stored in the circuit is given by:

$$E_p = C|V_0|^2. \quad (2.24)$$

Thus, the Q factor is:

$$Q = \frac{\omega_0 C}{G}, \quad (2.25)$$

where ω_0 is the resonant angular frequency, and the Q factor is proportional to the conductance G .

In an IPT system, a coil with high Q is always needed. A higher value of Q indicates a greater resonant amplitude and a lower rate of energy loss relative to the stored energy in the resonator. A typical value of Q for a coil implemented in an IPT system is at several hundred. In the next chapter, a novel design of the coil structure with a value of Q above 1000 will be introduced and analyzed.

2.5 Circuit Model of Coupled Inductors

2.5.1 General Coupled Inductors

Coupled inductors is a fundamental structure implemented in many electrical circuits and devices, such as transformers which transfers energy between two or more circuit through electromagnetic induction. Since an inductive power transfer system is essentially a transformer, the circuit model for coupled inductors is also applied to IPT analysis.

Fig. 2.9 shows a circuit model for two coupled inductors. Their self-inductance are L_P and L_S respectively, and the mutual inductance between them is M . The dot markings indicate terminals of corresponding polarity, i.e., if currents flow through the primary and secondary inductors from their dot-

marked terminals, the flux generated by each inductor itself will have contributions to the increase of that in the other. According to the theory of circuit, there exists:

$$v_P = L_P \frac{di_P}{dt} - M \frac{di_S}{dt}, \quad (2.26)$$

$$v_S = M \frac{di_P}{dt} - L_S \frac{di_S}{dt}, \quad (2.27)$$

where v_P and v_S are the voltages across the primary inductor and the secondary inductor, respectively, and i_P and i_S are the currents through the primary inductor and the secondary inductor, respectively.

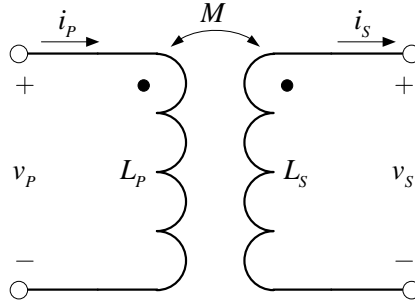


Fig. 2.9. Circuit model for two coupled inductors.

Then, (2.26) and (2.27) can be written as:

$$v_P = (L_P - M) \frac{di_P}{dt} + M \left(\frac{di_P}{dt} - \frac{di_S}{dt} \right), \quad (2.28)$$

$$v_S = M \left(\frac{di_P}{dt} - \frac{di_S}{dt} \right) - (L_S - M) \frac{di_S}{dt}. \quad (2.29)$$

From (2.28) and (2.29), we can equivalently get another circuit model for coupled inductors represented by a T-circuit of inductors as shown in Fig. 2.10.

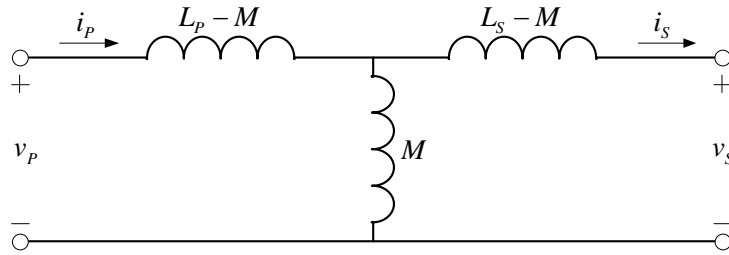


Fig. 2.10. Equivalent T-circuit model for two coupled inductors.

The mutual inductance, M , here is a measure of the coupling between two inductors. It has a relationship with the coupling coefficient k :

$$M = k\sqrt{L_p L_s}. \quad (2.30)$$

Since, the coupling coefficient is always between 0 and 1, it is convenient to use k to specify the relationship between a certain orientation of inductors with arbitrary inductance. When $k = 0$, there is no inductive coupling between two inductors. When $k = 1$, all the lines of flux of one inductor cut all the turns of the other, i.e., the two inductors are perfectly coupled.

2.5.2 Transformer

A transformer is an electrical device which transfers energy between two or more circuits through electromagnetic induction. Coupled inductors play a vital role in a transformer. For simplification or approximation purpose, it is common to analyze the transformer as an ideal transformer model. An ideal transformer is a theoretical, linear transformer which is under the assumption that winding resistances are negligible, that all the flux is confined to the core and links both windings, that there are no losses in the core, and that the permeability of the core is so high that only a negligible exciting magnetomotive force, also called mmf, is required to establish the flux [64]. In an ideal transformer, since flux is completely confined within the magnetic core, all the flux generated by the inductors cuts all the turns of all inductors, i.e., the

coupling coefficient of an ideal transformer is 1. These properties above are closely approached but never actually attained in practical transformers. The circuit model for an ideal transformer is represented in Fig 2.11.

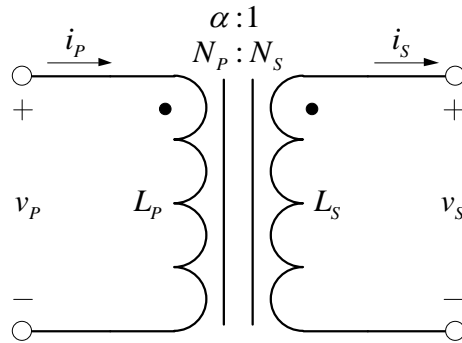


Fig. 2.11. Circuit model for an ideal transformer.

Fig. 2.11 shows an ideal transformer with a primary winding of N_P turns and a secondary winding of N_S turns. The winding turns ratio is denoted as α . According to Faraday's law of induction, since the same magnetic flux passes through both the primary and secondary windings, a voltage is induced in each winding:

$$v_P = -N_P \frac{d\Phi}{dt}, \quad (2.31)$$

$$v_S = -N_S \frac{d\Phi}{dt}. \quad (2.32)$$

Combine ratio (2.31) of (2.32):

$$\frac{v_P}{v_S} = \frac{N_P}{N_S} = \alpha. \quad (2.33)$$

From (2.33), the transformer winding voltage ratio is thus directly proportional to the winding turns ratio. If $\alpha > 1$, it is a step-down transformer. If $\alpha < 1$, it is a step-up transformer.

Since the core permeability is assumed very large, the net exciting mmf acting on the core is negligible. Thus, for the reference directions shown in Fig. 2.11, there exists:

$$N_P i_P - N_S i_S = 0, \quad (2.34)$$

$$\frac{i_P}{i_S} = \frac{N_S}{N_P} = \frac{1}{\alpha}. \quad (2.35)$$

Also notice from (2.33) and (2.35) that

$$v_P i_P = v_S i_S, \quad (2.36)$$

i.e., instantaneous power input to the primary equals the instantaneous power output from the secondary, because all the dissipative and energy storage mechanisms in the transformer have been neglected.

A more complete model for a real transformer must take into account the effects of winding resistances, leakage flux, and finite exciting current due to the finite permeability of the core. Fig. 2.12 shows the equivalent circuit models for a real transformer.

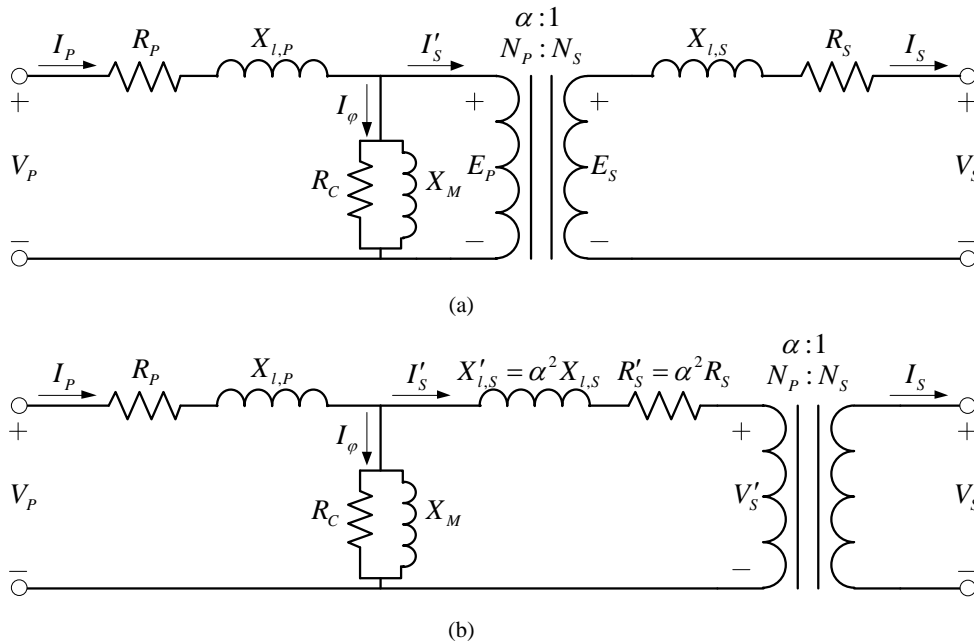


Fig. 2.12. Circuit models for a real transformer.

Referring to Fig. 2.12(a), a real transformer can be seen to be equivalent to an ideal transformer with external impedances. Winding joule losses and leakage reactances are represented by the series loop impedances, R_P and $X_{l,P}$ for the primary winding, and R_S and $X_{l,S}$ for the secondary winding. Core loss and reactance is represented by the shunt leg impedances, R_C for core losses and X_M for magnetizing reactance. By referring all quantities to the primary side, the ideal transformer can be moved out to the right as shown in Fig. 2.12(b), which is called the equivalent-T circuit for a transformer.

2.6 Reflected Impedance Model

A useful approach to analyze coupled windings is reflected impedance model. Fig. 2.13 shows the circuit model for coupled windings using current-controlled voltage sources (CCVS). Assuming sinusoidal voltages and currents are applied. For the reference direction, the values of CCVS are:

$$E_p = -j\omega MI_s, \quad (2.37)$$

$$E_s = j\omega MI_p. \quad (2.38)$$

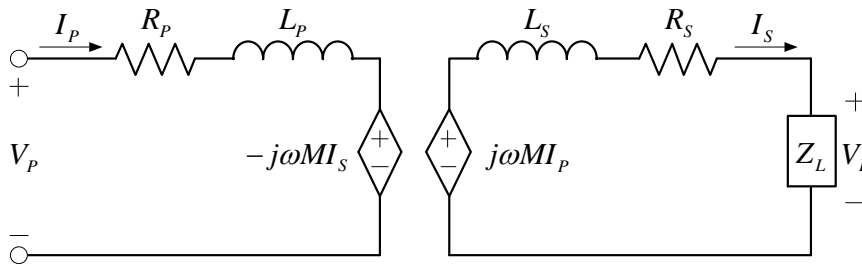


Fig. 2.13. Circuit model for coupled windings using CCVS.

We defined the secondary impedance Z_S as the total impedance as seen from the CCVS, given by:

$$Z_S = R_S + L_S + Z_L, \quad (2.39)$$

where R_S is the winding resistance, L_S is the winding inductance, and Z_L is the load impedance. The secondary current is given by:

$$I_S = \frac{E_S}{Z_S} = \frac{j\omega M I_P}{Z_S}. \quad (2.40)$$

Constituting (2.40) to (2.37):

$$E_P = -j\omega M I_S = \frac{(\omega M)^2}{Z_S} I_P. \quad (2.41)$$

Thus, the reflected impedance in the primary circuit is derived as:

$$Z_r = \frac{(\omega M)^2}{Z_S}. \quad (2.42)$$

From the analysis above, the existence of the load on the secondary side influences the primary circuit as a reflected impedance by voltage drop and power consumption. According to the reflected impedance Z_r , the circuit model for coupled windings with a load can be simplified by removing the secondary circuit as shown in Fig. 2.14.

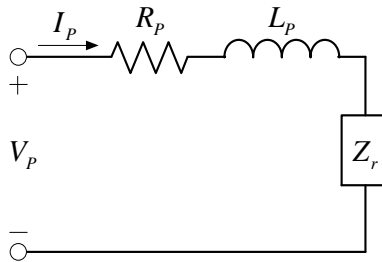


Fig. 2.14. Circuit model for coupled inductors using reflected impedance.

From Fig. 2.14, the real power transferred from the supply to the load is calculated as:

$$\begin{aligned}
 P_L &= \operatorname{Re} \left[\frac{Z_L E_s}{Z_s} \left(\frac{E_s}{Z_s} \right)^* \right] \\
 &= \left| \frac{E_s}{Z_s} \right|^2 \operatorname{Re}(Z_L) \\
 &= \left| \frac{j\omega M I_p}{Z_s} \right|^2 \operatorname{Re}(Z_L) \\
 &= \frac{(\omega M)^2}{|Z_s|^2} |I_p|^2 \operatorname{Re}(Z_L)
 \end{aligned} \tag{2.43}$$

It shows that the real power transferred from the supply to the load is influenced by the total impedance of the secondary circuit besides the impedance of the load. When the resistance of the secondary winding is much smaller compared with that of the load, i.e., $\operatorname{Re}(Z_s) \approx \operatorname{Re}(Z_L)$, the real power transferred is:

$$P_L = |I_p|^2 \operatorname{Re}(Z_r). \tag{2.44}$$

According to (2.44), the real power transferred to the load equals to the real power consumed by the reflected impedance, which proves that the reflected impedance model is also equivalent in terms of power transferred.

The power transfer efficiency is given by:

$$\begin{aligned}
 \eta &= \frac{\operatorname{Re}(Z_L) |I_s|^2}{\operatorname{Re}(Z_L) |I_s|^2 + R_s |I_s|^2 + R_p |I_p|^2} \\
 &= \frac{\operatorname{Re}(Z_L)}{\operatorname{Re}(Z_L) + R_s + R_p \frac{|Z_s|^2}{\omega^2 M^2}}
 \end{aligned} \tag{2.45}$$

As (2.45) suggests, larger load resistance, mutual inductance and operating frequency, and smaller resistances of coupled windings and secondary impedance will have a contribution to the increase of efficiency. In order to attain higher power transfer efficiency, besides reducing the resistances of primary and secondary windings and achieving stronger inductive coupling, an easy approach is to operate at the resonant frequency of the secondary circuit to

minimize the magnitude of the secondary impedance. However, the resonant frequency of the basic secondary circuit could be very high so that at relatively high frequencies, large active power flows in the circuit. Thus, real power supplied will decrease if VA rating is constant or a larger VA rating is needed in order to increase the real power output. This is one of the major disadvantages of using basic IPT configuration for power transfer. To overcome this, capacitive compensation in both primary and secondary circuit is implemented.

2.7 Capacitive Compensation

Capacitive compensation is often used in IPT systems to increase the power transfer efficiency and power transfer capability. Typically, compensating capacitors are implemented in both the primary and secondary circuit of an IPT system. The purpose of the secondary compensating capacitor is to increase the power transfer efficiency and enhance the power transfer capability. The purpose of the primary compensating capacitor is to decrease the VA rating provided by the power supply and ensure a relatively high power factor. Compensating capacitors essentially store and supply reactive power from and to the coupled inductors, reducing the amount of reactive power drawn from the supply [65].

There exist four basic types of compensating topologies. Depending on the serial (S) or parallel (P) connection of compensating capacitors in the primary and secondary circuit, they are SS, SP, PS and PP as shown in Fig. 2.15.

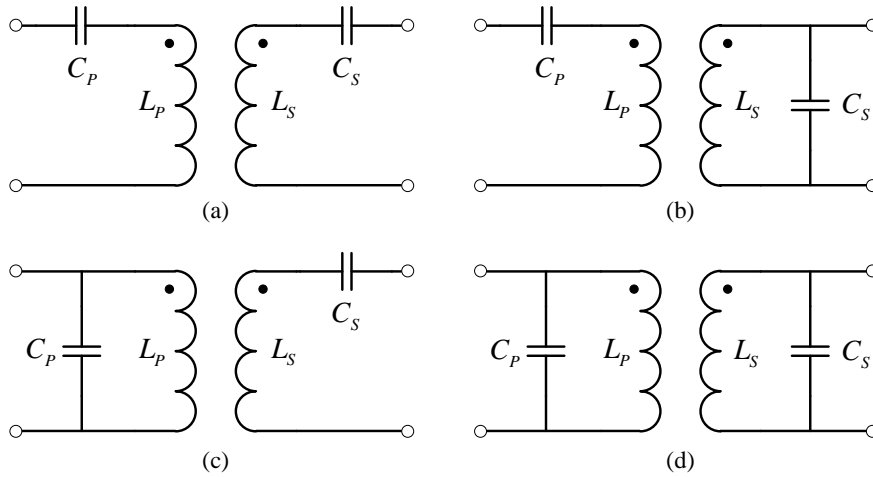


Fig. 2.15. Four types of compensating topologies: (a) SS, (b) SP, (c) PS, and (d) PP.

According to (2.45), no matter which above topology is applied, it is necessary that the IPT system operates at the resonant frequency of the secondary circuit to increase the power transfer efficiency. When operating at this frequency, the inductance of secondary winding is fully compensated by the secondary compensating capacitor and therefore the impedance of the secondary circuit is purely resistive in nature. As for the primary compensating capacitor, in all types of compensation, the value is so chosen that the total impedance as seen from the power supply is purely resistive in nature. It ensures minimum possible VA rating of the power supply and maximum magnitude of current flowing through the primary winding.

In the following sections, both series and parallel compensation in primary and secondary circuit are analyzed and equations are derived for choice of values of compensating capacitors according to reflected impedance method. A pure resistive load is considered and since the resistance of both primary and secondary windings are comparatively small in general, they are ignored through the derivation.

2.7.1 Secondary Compensation

Equivalent circuits using CCVS for both series and parallel secondary compensation are shown in Fig. 2.16. The CCVS is controlled by the current flowing through the primary winding.

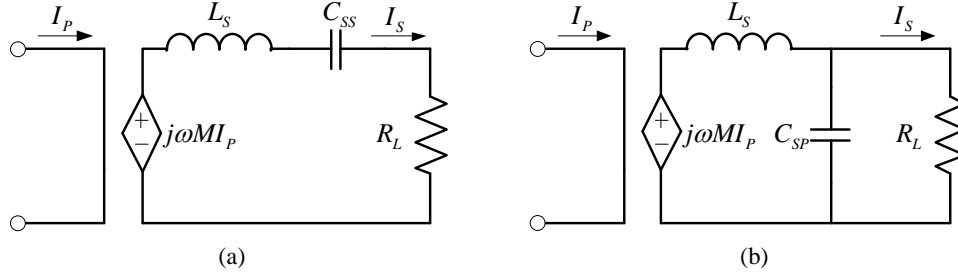


Fig. 2.16. Equivalent circuits using CCVS for (a) series secondary compensation, and (b) parallel secondary compensation.

As for series compensation, the secondary impedance as seen from the CCVS is given by:

$$Z_{SS} = R_L + j\omega L_s + \frac{1}{j\omega C_{SS}}. \quad (2.46)$$

The secondary impedance should be fully compensated to be purely resistive to achieve high efficiency. Thus, the secondary compensating capacitor is given by:

$$C_{SS} = \frac{1}{\omega_0^2 L_s}, \quad (2.47)$$

where ω_0 is the resonant angular frequency of the secondary circuit. When operating at this frequency, the reflected impedance can be calculated according to (2.42):

$$Z_{rS} = \frac{(\omega M)^2}{Z_{SS}} = \frac{(\omega M)^2}{R_L}, \quad (2.48)$$

which is purely resistive.

Similarly, for parallel compensation, the secondary impedance as seen from the CCVS is calculated as:

$$Z_{SP} = \frac{R_L}{1 + \omega^2 C_{SP}^2 R_L^2} + j \left(\omega L_S - \frac{\omega C_{SP} R_L^2}{1 + \omega^2 C_{SP}^2 R_L^2} \right). \quad (2.49)$$

Generally, ω_0 chosen ensures

$$\omega_0^2 C_{SP}^2 R_L^2 \gg 1. \quad (2.50)$$

Let the imaginary part equal to 0. Thus, the secondary compensating capacitor is given by:

$$C_{SP} = \frac{1}{\omega_0^2 L_S}, \quad (2.51)$$

which equals to that of series compensation. Similar to series compensation, when operating at the secondary resonant frequency, the reflected impedance can be calculated as:

$$Z_{rP} = \frac{(\omega M)^2}{Z_{SP}} = \frac{R_L M^2}{L_S^2}, \quad (2.52)$$

which is also purely resistive.

2.7.2 Primary Compensation

Equivalent circuits of both series and parallel primary compensation are shown in Fig. 2.17. The secondary impedance is reflected to the primary based on above discussion.

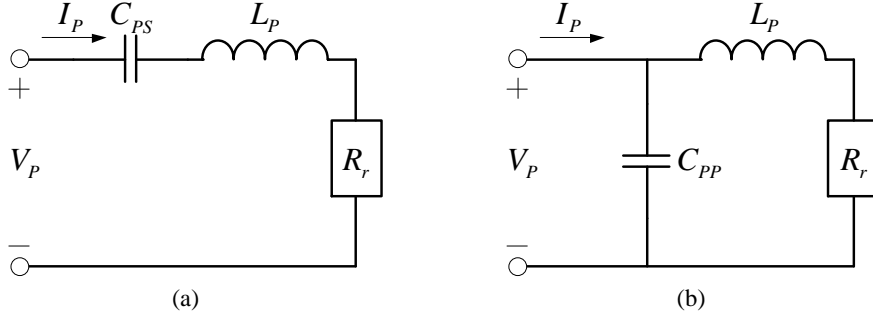


Fig. 2.17. Equivalent circuits with reflected impedance for (a) series primary compensation, and (b) parallel primary compensation.

When operating at the secondary resonant frequency, no matter what type of compensating the secondary uses, the reflected impedance is purely resistive, denoted as R_r . According to (2.48) and (2.52), there exists:

$$R_r = \begin{cases} \frac{(\omega M)^2}{R_L} & \text{if series secondary compensation} \\ \frac{R_L M^2}{L_s^2} & \text{if parallel secondary compensation} \end{cases}. \quad (2.53)$$

In order for minimum possible VA rating of the power supply and maximum magnitude of current flowing through the primary winding, the primary impedance as seen by the power supply should also be fully compensated. As for series compensation, the primary impedance is calculated as:

$$Z_{PS} = R_r + j\omega L_P + \frac{1}{j\omega C_{PS}}. \quad (2.54)$$

Thus, the primary compensating capacitor is given by:

$$C_{PS} = \frac{1}{\omega_0^2 L_P}. \quad (2.55)$$

Similarly, for parallel compensation, the primary impedance as seen from the power supply is given as:

$$Z_{PP} = \frac{R_r}{1 + \omega^2 C_{PP}^2 R_r^2} + j \left(\omega L_P - \frac{\omega C_{PP} R_r^2}{1 + \omega^2 C_{PP}^2 R_r^2} \right). \quad (2.56)$$

Generally, ω_0 chosen ensures

$$\omega_0^2 C_{PP}^2 R_r^2 \gg 1. \quad (2.57)$$

Let the imaginary part equal to 0. Thus, the secondary compensating capacitor is given by:

$$C_{PP} = \frac{1}{\omega_0^2 L_p}. \quad (2.58)$$

To summarize, the secondary compensating capacitor CS is chosen by:

$$C_s = \frac{1}{\omega_0^2 L_s}, \quad (2.59)$$

no matter what type of compensation is applied in the secondary circuit. The primary compensating capacitor CP is chosen by:

$$C_p = \frac{1}{\omega_0^2 L_p}, \quad (2.60)$$

no matter what type of compensation is applied in the primary circuit.

2.8 Energy Losses

2.8.1 Skin Effect

The skin effect, first described in a paper by Horace Lamb in 1883, is the tendency for high-frequency alternating currents to become distributed within a conductor such that the current density is largest near the surface of the conductor, and decrease with greater depths in the conductor. The cause of the skin effect field is electromagnetic induction. An alternating current in a conductor produces an alternating magnetic field in and around the conductor. The change in the magnetic field, in turn, creates an electric field which opposes

the change in the current. This opposing electric field is strongest at the center of the conductor, and forces the conducting electrons to the outside of the conductor, resulting in greatest current density at the surface of the conductor with a reduced magnitude deeper in the conductor. Based on the theory of electromagnetism, the alternating current density J in a conductor decreases exponentially from its value at the surface J_s according to the depth d from the surface, as follows:

$$J = J_s e^{-\frac{d}{\delta}}, \quad (2.61)$$

where δ is called skin depth, defined as the depth below the surface of the conductor at which the current density has fallen to e^{-1} of J_s . In normal cases, it is well approximated as:

$$\delta = \sqrt{\frac{2\rho}{\omega\mu_r\mu_0}}, \quad (2.62)$$

where ρ is resistivity of the conductor, ω is angular frequency of the current, μ_r is relative magnetic permeability of the conductor, and μ_0 is the permeability of free space. Fig. 2.18 gives a schematic diagram of current distribution in a cylindrical conductor caused by the skin effect.

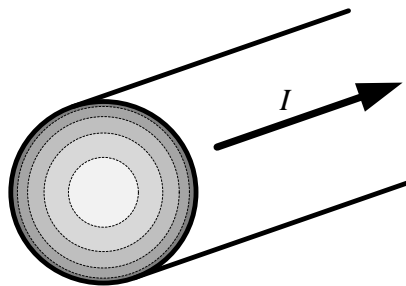


Fig. 2.18. Schematic diagram of current distribution in a cylindrical conductor caused by the skin effect, with dark color showing high current density.

Skin depth is proportional to square root of the resistivity of the conductor, which means that better conductors have a reduced skin depth. Skin effect also varies as the inverse square root of the permeability of the conductor, so a

ferromagnetic conductor typically has a relatively small skin depth. Table 2.1 lists the skin depth of some common conductive materials at different frequencies.

Table 2.1. Skin depth of some conductive materials.

Material	Skin Depth (m)			
	$f=60$ Hz	$f=10^3$ Hz	$f=10^6$ Hz	$f=10^9$ Hz
Copper	8.61×10^{-3}	2.1×10^{-3}	6.7×10^{-5}	2.11×10^{-6}
Iron	6.5×10^{-4}	1.6×10^{-4}	5.03×10^{-6}	1.6×10^{-8}
Seawater	32.5	7.96	0.25	7.96×10^{-3}
Wet Soil	650	159	5.03	0.16

According to (2.61), over 98% of the current flows within a layer 4 times the skin depth from the surface, which is distinct from that of direct current usually distributed evenly over the cross-section of the wire. Therefore, when an AC current flows through a conductor, the skin effect causes the effective resistance of the conductor larger than that when a DC current flows through. At higher frequencies where the skin depth is smaller, the increase of the effective resistance is significant. The effective resistance can be approximately solved as if the current flowed uniformly through a layer of thickness δ based on the DC resistivity. Thus a long cylindrical conductor, such as wire, with a length L and a diameter D much larger compared to δ , has a resistance approximately that of a hollow tube with wall thickness δ carrying DC current:

$$R \approx \frac{L\rho}{\pi(D-\delta)\delta} \approx \frac{L\rho}{\pi D\delta}, \quad (2.63)$$

where ρ is resistivity of the conductor.

To mitigate skin effect, a type of cable called litz wire is used for frequencies of a few kHz to about one MHz. It consists of a number of insulated wire strands woven together in a carefully designed pattern, so that the overall magnetic field acts equally among them. With the skin effect having little effect

on each of the thin strands, the bundle does not suffer the same increase in AC resistance that a solid conductor of the same cross-sectional area would due to the skin effect.

2.8.2 Proximity Effect

The term proximity effect refers to the influence of alternating current in one conductor on the current distribution in another nearby conductor. The reason for proximity effect is also electromagnetic induction.

When an AC current flows through a conductor, it creates an associate alternating magnetic field around it. The alternating magnetic field induces eddy currents in adjacent conductors, altering the overall distribution of current flowing through them. The result is that the current is concentrated to smaller regions. For example, if two wires carrying the same AC current lie parallel to one another, such as a coil used in an inductor or transformer, the magnetic field of one wire will induce longitudinal eddy currents in the adjacent wire, which flow in long loops along the wire, in the same direction as the main current on the side of the wire facing away from the other wire, and back in the opposite direction on the side of the wire facing the other wire. Therefore, the eddy current will reinforce the main current on the side facing away from the first wire, and oppose the main current on the side facing the first wire. The net effect is to redistribute the current in the cross section and result in current crowding on the side facing away from the other wire. This phenomenon is illustrated in Fig. 2.19. Similarly, in two adjacent conductors carrying AC currents flowing in opposite directions, such as power cables and a pairs of bus bars, the current in each conductor is concentrated into a strip on the side facing the other conductor.

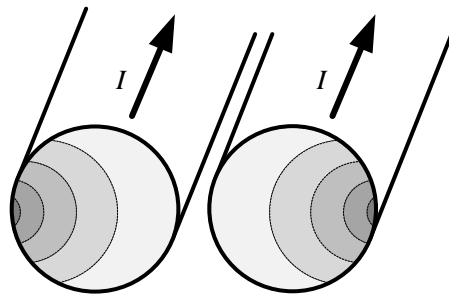


Fig. 2.19. Schematic diagram of current distribution in parallel cylindrical conductors caused by the proximity effect, with dark color showing high current density.

Since the proximity effect can concentrate the current in an adjacent conductor into a small area of the cross section, the AC resistance of the adjacent conductor is increased when compared to its DC resistance. At higher frequencies, the proximity effect will significantly increase. The additional resistance will increase total power losses and reduce the Q factor in inductors. To minimize the proximity effect, special construction is used. The winding is usually limited to a single layer, and the turns are often spaced apart to separate the conductors. In multilayer coils, the successive layers are wound in a crisscross pattern to avoid having wires lying parallel to one another. Since the current flows on the surface of the conductor, high frequency coils are sometimes silver-plated, or made of litz wire.

2.8.3 Core Losses

Ferromagnetic materials are usually used as magnetic cores in inductors or transformers. When the core is subjected to a changing magnetic field caused by AC currents, some of the power is lost in the core, dissipated as heat and sometimes noise. Core losses are often described as being in two categories: hysteresis losses and eddy current losses.

Hysteresis losses are caused by the movement of domain walls in ferromagnetic materials, which changes the magnetization of the material by expansion and contraction of the tiny magnetic domains when the applied

magnetic field through the material changes. When the domain walls move, they get "snagged" on defects in the crystal structure and then "snap" past them, dissipating energy as heat. Hysteresis losses can be seen in the B-H curve of the material, which has the form of a closed loop. The amount of energy lost in the material in one cycle of the applied magnetic field is proportional to the area inside the hysteresis loop. Since the energy lost in each cycle is constant, hysteresis power losses increase proportionally with frequency. Hysteresis losses are given by an approximate formula:

$$P_h \approx W_h f \approx \eta f \beta_{\max}^{1.6}, \quad (2.64)$$

where f is the frequency, η is the hysteresis coefficient, β_{\max} is the maximum flux density, and W_h is the energy lost in one cycle according to Steinmetz's formula:

$$W_h \approx \eta \beta_{\max}^{1.6}. \quad (2.65)$$

The empirical exponent varies from about 1.4 to 1.8, but is often given as 1.6 for iron [66-68].

Eddy current losses are the energy of the eddy current dissipated as heat in the resistance of the core material. Eddy currents are circulating loops of currents induced by the changing magnetic field in the core, due to electromagnetic induction, and the loops of currents flow perpendicular to the magnetic field. The power losses are proportional to the area of the loops and the square of frequency, and inversely proportional to the resistivity of the core material.

To reduce the eddy current losses, special design in transformers is employed to construct the core by stacking layers of thin steel laminations. Each lamination is insulated from its neighbors by a thin non-conducting layer of insulation. The effect of laminations is to confine eddy currents to highly

elliptical paths enclosing little area, which greatly reduces eddy current losses. An illustration showing eddy currents both in a solid core block and a laminated core is given in Fig. 2.20.

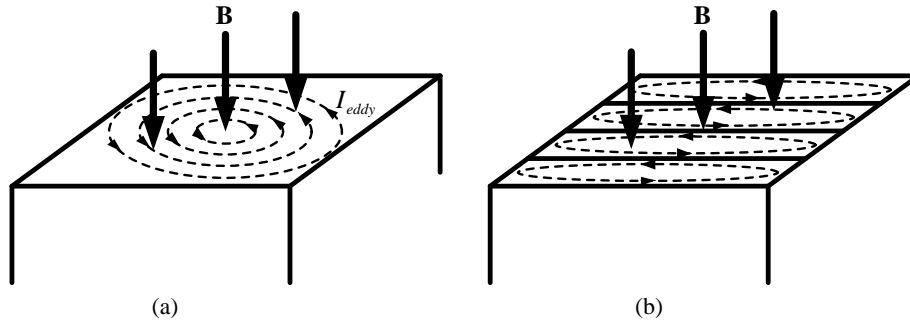


Fig. 2.20. Eddy currents in (a) a solid core block, and (b) a laminated core.

2.9 Summary

In this chapter, the basic laws in of inductive power transfer, which are Ampère's circuital law and Faraday's law of induction, are firstly reviewed. Ampère's law describes the magnetic field produced by current and Faraday's law describes the electromotive force generated by time-varying magnetic flux. The magnetic characteristics of substances, including ferromagnetic, paramagnetic, and diamagnetic is also introduce. Ferromagnetic materials is very important in IPT, which contributes to energy storage and transmission. A phenomenon called magnetic hysteresis exists in ferromagnetic materials and causes the relationship between magnetic flux density \mathbf{B} and magnetic field strength \mathbf{H} nonlinear and multivalued.

Electrical resonance is that energy stored in electric field and magnetic field transfers significantly back and forth between capacitors and inductors. The simplest resonant circuits are series RLC circuit and parallel RLC circuit. Resonance occurs at resonant frequency with strongly magnified current or

voltage. A key parameter of resonant circuit, Q , is defined as the ratio of the peak energy stored to the average energy dissipated in it per cycle at resonance, and high Q indicates great resonant amplitude and low rate of energy loss relative to the stored energy in the resonator.

As a fundamental structure of IPT systems, various circuit models for coupled inductors are introduced. A reflected impedance method, which replaces the secondary circuit with an equivalent impedance in the primary circuit, is applied to analyze coupled inductors. The power transfer efficiency is derived and suggests capacitive compensation both in primary and secondary circuit. Four types of capacitive compensation, i.e., SS, SP, PS, and PP, are introduced, and equations for capacitances are derived. The equations have the same form no matter what type of compensation is applied both in primary and secondary circuit.

In real coupled inductors, skin effect and proximity effect change the distribution of current flowing in a conductor and result in resistance increasing. Litz wire wound in specially designed patterns can mitigate the disadvantages. Core losses in ferromagnetic materials are caused by hysteresis losses and eddy current losses. Low operating frequency and laminated cores help to reduce these losses.

Chapter 3

Design and Fabrication of the High-Q Resonant Coil

3.1 Introduction

In this chapter, a novel design on the structure of resonant coil is introduced. With this special design, the resonant coil can achieve relatively high Q to improve the power transfer capability and the power transfer efficiency of IPT systems. In Section 3.2, the structure of the resonant coil is presented and explained in detail. Then, based on the simulation of current distribution, the equivalent circuit model for the resonant coil is established and the function of resonant frequency is derived in Section 3.3. Next, in Section 3.4, materials for prototypes are carefully selected. Finally, in Section 3.5, prototypes of the resonant coils are fabricated and measured to verify the theoretical derivation and simulation on resonant frequency. This chapter is concluded in Section 3.6.

3.2 Structure of the Resonant Coil

As discussed in the previous chapter, in high frequency transformers, energy losses caused by skin effect and proximity effect can be a problem. Litz wire is often used as a solution. Litz wire is a type of cable which consists of many thin wire strands, individually insulated and twisted or woven together,

following one of several carefully prescribed pattern. The dimension of each thin conductor in the litz wire is less than a skin depth, so an individual strand does not suffer an appreciable skin effect loss. Current is distributed equally among every strand, which allows the interior of the litz wire to contribute to the cable's conductivity. However, coils using litz wire have some limitations. One limitation is that coils made of litz wire cannot achieve very high Q, typically from tens to hundreds. Another limitation is that the fabrication cost of litz wire is high, especially at micrometer level, which results in an increasing unfavorable tradeoff between fabrication cost and energy losses at higher frequencies.

To overcome these limitations and improve the performance of the coil, a new design on the structure of resonant coil is applied [69]. The resonant coil uses thin layers of conductor and dielectric instead of litz wire, which are easier to fabricate and less expensive compared to insulated thin wire strands. It is formed by a stack of thin conductor and dielectric layers filling the winding area of an open pot core illustrated in Fig. 3.1.

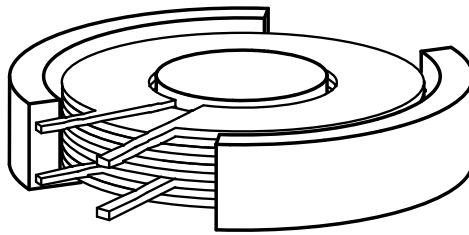


Fig. 3.1. Schematic diagram with exaggerated thickness of layers of the resonant coil.

Usually, a resonant coil carrying high currents consists of several repeating sub-stacks, named sections, of the same topology. In one section, as shown in Fig. 3.2, starting with a conductor layer at the bottom, dielectric layers and conductor layers are alternately stacked above, ending up a with conductor layer on the top, i.e., each two adjacent conductor layers in the section are separated by a dielectric layer in between. The top conductor layer has two terminals for

the connection to external circuits. Aside from the top conductor layer, there are no other electrical contacts, no vias or external connections, in the rest of the structure of a section.

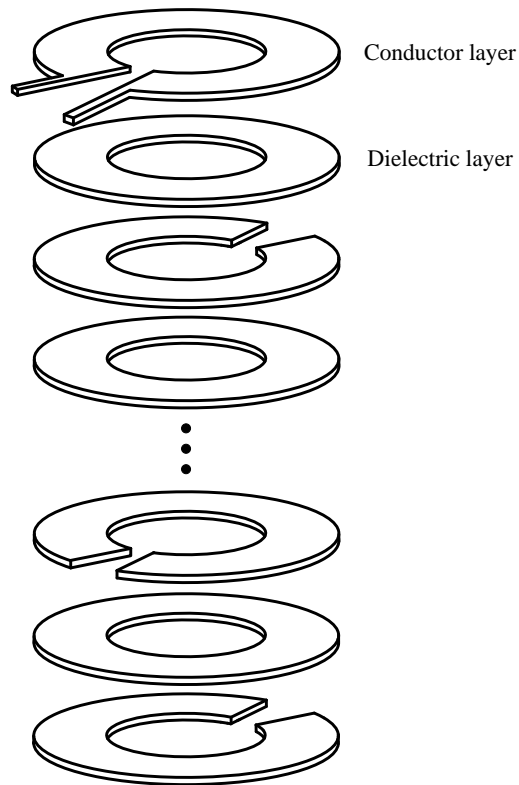


Fig. 3.2. The structure of a section.

The basic components in a section are dielectric layer conductor layer. Each dielectric layer is toroid shaped and each conductor layer is C shaped. The two successive C-shaped conductor layers are placed with the C's facing in opposite orientations. Therefore, two overlapping areas are formed symmetrically between successive conductor layers. A sandwich unit is defined as two successive conductor layers with one dielectric layer in between as shown in Fig. 3.3. This definition is good for circuit analysis which can be seen in following sections. The symmetric overlapping areas are described by a parameter named overlap angle θ , with other parameters of dimension defined in Fig. 3.3. According to above configuration and definitions, a section of the resonant coil can be also seen as a stack of units, each two separated by a

dielectric layer, and only the top conductor layer has the connection to external circuits. Moreover, a resonant coil can be seen as a stack of sections, each two separated by several more dielectric layers which can reduce displacement currents flowing through successive sections.

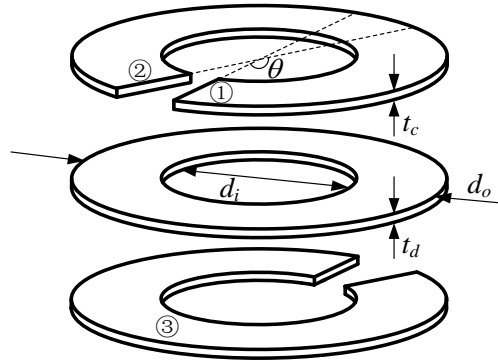


Fig. 3.3. The structure of a unit.

3.3 Circuit Analysis of the Resonant Coil

3.3.1 Current Distribution of the Resonant Coil

In order to explain how this structure works, circuit simulation and analysis are presented in this section. The resonant coil is essentially an integration of resistances, inductances and capacitances. Resistances mainly exist in each conductor layer, resulting in voltage drop along conductor layers. Inductances include self-inductances and mutual inductances, existing in each conductor layer and among conductor layers respectively, and causing voltage drop along conductor layers as well. Due to strong coupling by the ferrite core, mutual inductances are considered between any two conductor layers. Capacitances are formed by the overlapping areas of conductor layers together with the dielectric layer between them, which provide good current sharing between conductor layers. Therefore, resistances, inductances and capacitances distributed in the

resonant coil contribute to currents flowing in two directions: parallel with conductor layers and perpendicular to conductor layers.

For a resonant coil with multiple sections, since each section is in parallel with others, it is sufficient to examine current distribution in just one section. A distributed circuit model for one section of the resonant coil is built in LTspice as shown in Fig. 3.4.

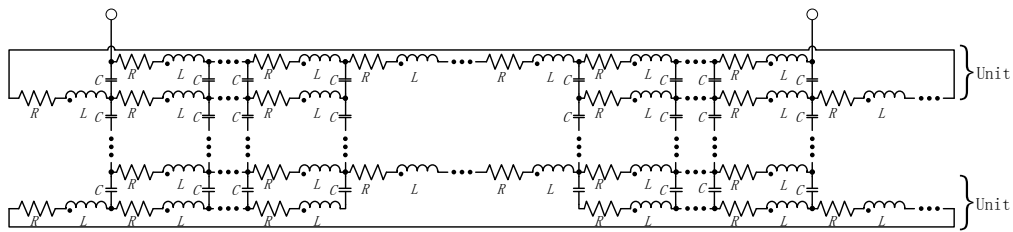


Fig. 3.4. Distributed RLC model for one section of the resonant coil.

In this distributed circuit model, a conductor layer is represented by a row of resistors and inductors alternatively connected in series. Each pair of resistor and inductor is seen as an element of the conductor layer. A dielectric layer is represented by a row of capacitors, which relates two successive conductor layers by connecting the terminals of elements in two conductor layers. The number of elements in conductor layers or the number of capacitors in dielectric layers is determined by accuracy of the simulation. The more elements a model has, the more accurate the simulation results are.

The simulation results of a resonant coil with an overlap angle of 170° show that in a unit, the magnitude of conduction current in the conductor layer increases linearly from one edge to the non-overlapping area opposite to the open slot, and then decreases linearly until reaching the other edge. The maximum magnitude of conduction current which occurs in the non-overlapping area is denoted by I_{\max} . The angular position from 0° to 360° is easily used to describe the ring-shaped unit with 0° referring to the central position of the open slot of the top C-shaped conductor layer of the unit. The

magnitude of conduction current in conductor layers varying with the angular position is caused by displacement current in the capacitors of dielectric layers. From the edge of conductor layer and along the direction of current, displacement currents flow into the conductor layer from the above and below dielectric layers until reaching the non-overlapping area, and then flow out of the conductor layer to the above and below dielectric layers until reaching the other edge. The simulation result on the magnitude of conduction current in the conductor layers of the unit is illustrated in Fig. 3.5, and the result on the magnitude of displacement current density per angle in the dielectric layer of the unit is illustrated in Fig. 3.6. The reference direction in Fig. 3.6 is from Conductor Layer 2 to Conductor Layer 1 as shown in Fig 3.5. All the magnitudes are normalized by I_{\max} .

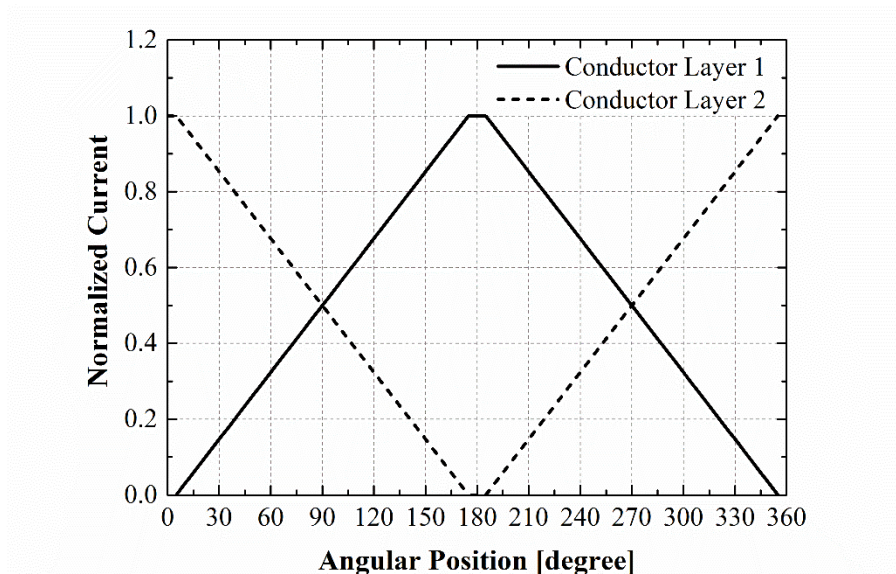


Fig. 3.5. Normalized magnitude of currents in two conductor layers of a unit versus angular position.

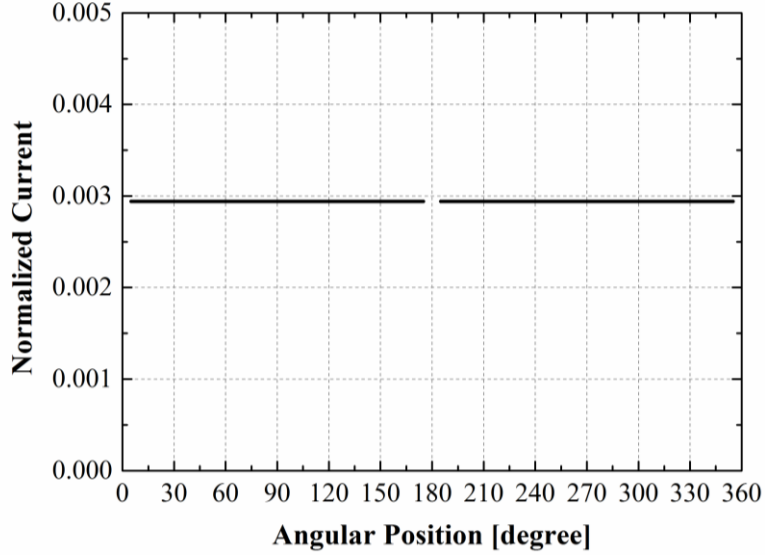


Fig. 3.6. Normalized magnitude of current density per angle in the dielectric layer of a unit versus angular position.

3.3.2 Equivalent Circuit Model for Unit Structure

In a more general case of a unit with an overlap angle θ , the magnitude of conduction current flowing through the Conductor Layer 1, I_{c1} , is given by a function of the angular position φ as follows:

$$I_{c1} = \begin{cases} \frac{I_m}{\theta} \left(\varphi - \frac{\pi - \theta}{2} \right) & \left(\frac{\pi - \theta}{2} \leq \varphi < \frac{\pi + \theta}{2} \right) \\ I_m & \left(\frac{\pi + \theta}{2} \leq \varphi \leq \frac{3\pi - \theta}{2} \right) \\ -\frac{I_m}{\theta} \left(\varphi - \frac{3\pi + \theta}{2} \right) & \left(\frac{3\pi - \theta}{2} < \varphi \leq \frac{3\pi + \theta}{2} \right) \end{cases} . \quad (3.1)$$

Similarly, the magnitude of conduction current flowing through the Conductor Layer 2, I_{c2} , is given by:

$$I_{c2} = \begin{cases} I_m & \left(0 \leq \varphi \leq \frac{\pi - \theta}{2}, \frac{3\pi + \theta}{2} \leq \varphi < 2\pi \right) \\ -\frac{I_m}{\theta} \left(\varphi - \frac{\pi + \theta}{2} \right) & \left(\frac{\pi - \theta}{2} < \varphi \leq \frac{\pi + \theta}{2} \right) \\ \frac{I_m}{\theta} \left(\varphi - \frac{3\pi - \theta}{2} \right) & \left(\frac{3\pi - \theta}{2} \leq \varphi < \frac{3\pi + \theta}{2} \right) \end{cases} . \quad (3.2)$$

Based on the previously defined reference direction of displacement current, the magnitude of displacement current flowing in the dielectric layer per radian, I_d , is given by:

$$I_d = \begin{cases} 0 & \left(0 \leq \varphi \leq \frac{\pi - \theta}{2}, \frac{\pi + \theta}{2} \leq \varphi \leq \frac{3\pi - \theta}{2}, \frac{3\pi + \theta}{2} \leq \varphi < 2\pi \right) \\ \frac{I_m}{2\theta} & \left(\frac{\pi - \theta}{2} < \varphi < \frac{\pi + \theta}{2} \right) \\ -\frac{I_m}{2\theta} & \left(\frac{3\pi - \theta}{2} < \varphi < \frac{3\pi + \theta}{2} \right) \end{cases} \quad (3.3)$$

If seeing the two conductor layers as a whole, the current will flow in the conductive loop continuously and constantly at all angular position. Then, the loop current I_0 of a unit is defined by adding I_{c1} and I_{c2} , i.e.,

$$I_0 = I_{c1} + I_{c2} = I_m \quad (0 \leq \varphi < 2\pi). \quad (3.4)$$

This definition is very helpful to simplify the equivalent circuit of a unit by using a lumped circuit model instead of the complex and distributed circuit model. The lumped circuit model for a unit is shown in Fig. 3.7.

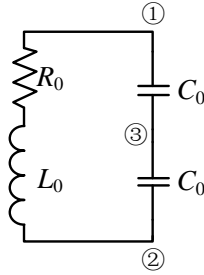


Fig. 3.7. Lumped circuit model for a unit.

The terminals of ①-③ in Fig. 3.7 correspond to the physical points ①-③ of the unit in Fig. 3.3, i.e., point ① and ② refer to the two edges of the upper conductor layer and point ③ refers to the middle of the non-overlapping area of the lower conductor layer. Circuit elements are the resultant properties of electrical parameters within the unit. R_0 and L_0 refer to the resistance and the inductance of the conductive loop in respect to the loop current I_0 , respectively.

C_0 refers to the capacitance of each overlapping area. The values of R_0 , L_0 , and C_0 are derived as follows.

As for a single conductive layer loop, the resistance R_{loop} is given by the integral of resistance from the inner diameter to the outer diameter, i.e.,

$$R_{loop} = \frac{1}{\int_{\frac{d_i}{2}}^{\frac{d_o}{2}} \frac{t_c dr}{2\pi\rho r}} = \frac{2\pi\rho}{t_c \ln \frac{d_o}{d_i}}, \quad (3.5)$$

where ρ is the resistivity of the conductor, t_c is the thickness of the layer, d_o and d_i are the outer and inner diameter of the layer. Since currents in conductor layers of the unit linearly increases or decreases over the distance of the overlap angle θ , the equivalent resistance of the unit at the overlapping areas is halved in terms of the maximum current I_m . Thus, the equivalent resistance of the unit is derived as:

$$R_0 = \frac{\theta R_{loop}}{2\pi} + \frac{(\pi - \theta) R_{loop}}{2\pi} = \frac{R_{loop}}{2} = \frac{\pi\rho}{t_c \ln \frac{d_o}{d_i}}. \quad (3.6)$$

The inductance L_0 , which is an approximation of a circular loop configuration, is given by:

$$L_0 = \frac{\mu_0 \mu_r (d_o + d_i)}{4} \left[\ln \frac{8(d_o + d_i)}{d_o - d_i} - 2 \right], \quad (3.7)$$

where μ_0 is the vacuum permeability, and μ_r is the relative permeability of ferrite core.

The capacitance C_0 , is calculated as a parallel-plate configuration:

$$C_0 = \frac{\epsilon_0 \epsilon_r \theta (d_o^2 - d_i^2)}{8t_d}, \quad (3.8)$$

where ϵ_0 is the vacuum permittivity, ϵ_r is the relative permittivity of dielectric, and t_d is the thickness of the dielectric layer.

3.3.3 Equivalent Circuit Model for Section Structure

The lumped circuit model for a section, as shown in Fig. 3.8, is a combination of circuit models for the units. The connections between units in Fig. 3.8 are the capacitors C_1 also caused by dielectric layers. Thus, C_1 has the same value as C_0 , i.e.,

$$C_1 = C_0 = \frac{\epsilon_0 \epsilon_r \theta (d_o^2 - d_i^2)}{8t_d}. \quad (3.9)$$

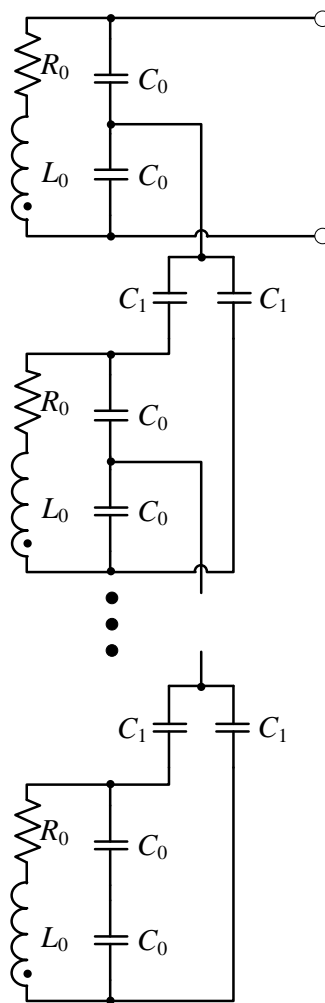


Fig. 3.8. Lumped circuit model for a section.

According to the equivalent circuit model for a section, units are connected by both mutual inductive coupling and capacitive coupling. Assuming strong

mutual inductive coupling between each two units, i.e., the coupling coefficient is close to 1, the mutual inductance M between each two units can be written as:

$$M = L_0 = \frac{\mu_0 \mu_r (d_o + d_i)}{4} \left[\ln \frac{8(d_o + d_i)}{d_o - d_i} - 2 \right]. \quad (3.10)$$

The assumption of identical L_0 and M is based on no leakage flux among conductor layers. If the resonant coil have many layers, multiple sections are employed with electrical connected in parallel to ensure effective current sharing through capacitors and strong inductive coupling with little leakage among layers. The following derivation are based on these assumptions so that C_0 are used for all capacitors for simplicity.

3.3.4 Resonant Frequency of the Resonant Coil

To calculate the resonant frequency of the resonant coil, the equivalent circuit model must be further simplified. In Fig. 3.8, the impedances of the units which has no electrical connection to the external circuit, denoted as $Z_{0,(2)}$ are reflected to the first top unit. The total reflected impedance is called Z' , as shown in Fig. 3.9. The resonant frequency of a stack with N units is derived as follows.

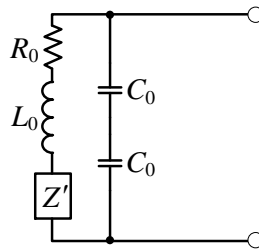


Fig. 3.9. Equivalent circuit for a resonant coil using reflected impedance.

As for the unit without galvanic connections, there exists:

$$Z_{0,(2)} = R_0 + j\omega L_0 + \frac{1}{j\omega C_0}, \quad (3.11)$$

$$0 = j\omega M \left[I_{0,(1)} + (N-2)I_{0,(2)} \right] + Z_{0,(2)} I_{0,(2)}, \quad (3.12)$$

where $I_{0,(1)}$ and $I_{0,(2)}$ are the loop currents flowing through the top unit and the rest units, respectively, and N is the number of total units. Substituting (3.11) to (3.12), $I_{0,(2)}$ can be rewrite in terms of $I_{0,(1)}$ as:

$$I_{0,(2)} = -\frac{j\omega M}{R_0 + j\left[\omega L_0 + \omega M(N-2) - \frac{1}{\omega C_0}\right]} I_{0,(1)}. \quad (3.13)$$

Then, the expression of the reflected impedance of one unit Z'_0 is:

$$Z'_0 = \frac{j\omega M I_{0,(2)}}{I_{0,(1)}} = \frac{\omega^2 M^2}{R_0 + j\left[\omega L_0 + \omega M(N-2) - \frac{1}{\omega C_0}\right]}. \quad (3.14)$$

Its real part and imaginary part are respectively given by:

$$\text{Re}(Z'_0) = \frac{\omega^4 C_0^2 M^2 R_0}{\left\{\omega^2 C_0 [L_0 + M(N-2)] - 1\right\}^2 + \omega^2 C_0^2 R_0^2}, \quad (3.15)$$

$$\text{Im}(Z'_0) = -\frac{\omega^3 C_0 M^2 \left\{\omega^2 C_0 [L_0 + M(N-2)] - 1\right\}}{\left\{\omega^2 C_0 [L_0 + M(N-2)] - 1\right\}^2 + \omega^2 C_0^2 R_0^2}. \quad (3.16)$$

In general, R_0 , L_0 and C_0 are of the order of milliohm, microhenry and nanofarad.

Thus, the reflected resistance and reactance can be approximately calculated as:

$$\text{Re}(Z'_0) \approx \omega^4 C_0^2 M^2 R_0, \quad (3.17)$$

$$\text{Im}(Z'_0) \approx \omega^3 C_0 M^2. \quad (3.18)$$

Since all the rest units are assumed to have the same influence on the top unit, the total reflected impedance are the linear addition of each reflected impedance:

$$Z' = (N-1)Z'_0. \quad (3.19)$$

Finally, the impedance of the coil, named Z_{coil} , as seen from its two terminals are derived as:

$$\begin{aligned} \operatorname{Re}(Z_{coil}) &= \frac{4[R_0 + (N-1)\omega^4 C_0^2 M^2 R_0]}{\left\{2 - \omega^2 C_0 [L_0 + (N-1)\omega^2 C_0 M^2]\right\}^2 + \omega^2 C_0^2 [R_0 + (N-1)\omega^4 C_0^2 M^2 R_0]^2}, \quad (3.20) \\ &\approx \frac{4R_0}{\left\{2 - \omega^2 C_0 [L_0 + (N-1)\omega^2 C_0 M^2]\right\}^2 + \omega^2 C_0^2 [R_0 + (N-1)\omega^4 C_0^2 M^2 R_0]^2} \end{aligned}$$

$$\begin{aligned} \operatorname{Im}(Z_{coil}) &= \frac{4\omega [L_0 + (N-1)\omega^2 C_0 M^2]}{\left\{2 - \omega^2 C_0 [L_0 + (N-1)\omega^2 C_0 M^2]\right\}^2 + \omega^2 C_0^2 [R_0 + (N-1)\omega^4 C_0^2 M^2 R_0]^2} \\ &\quad - \frac{2\omega C_0 \left\{[\omega L_0 + (N-1)\omega^3 C_0 M^2]^2 + [R_0 + (N-1)\omega^4 C_0^2 M^2 R_0]^2\right\}}{\left\{2 - \omega^2 C_0 [L_0 + (N-1)\omega^2 C_0 M^2]\right\}^2 + \omega^2 C_0^2 [R_0 + (N-1)\omega^4 C_0^2 M^2 R_0]^2}. \quad (3.21) \\ &\approx \frac{4\omega [L_0 + (N-1)\omega^2 C_0 M^2] - 2\omega^3 C_0 [L_0 + (N-1)\omega^2 C_0 M^2]^2}{\left\{2 - \omega^2 C_0 [L_0 + (N-1)\omega^2 C_0 M^2]\right\}^2 + \omega^2 C_0^2 [R_0 + (N-1)\omega^4 C_0^2 M^2 R_0]^2} \end{aligned}$$

When resonance happens, the impedance is purely resistive. By setting the imaginary part equal to zero, the resonant frequency f_0 can be derived by solving the following equation:

$$0 = 4[L_0 + (N-1)\omega^2 C_0 M^2] - 2\omega^3 C_0 [L_0 + (N-1)\omega^2 C_0 M^2]^2. \quad (3.22)$$

Typically, the number of units N is from tens to hundreds. Thus, the approximate solution of resonant frequency f_0 is:

$$f_0 \approx \frac{\sqrt[4]{2}}{2\pi \sqrt{L_0 C_0} \sqrt[4]{N}}. \quad (3.23)$$

3.4 Materials Selection

3.4.1 Conductor Layer

A major considerations for choosing conductive materials is to reduce energy loss caused by AC resistance. According to Section 2.8.1, the AC resistance of a conductor at a certain frequency is mainly determined by its resistivity and skin depth at this frequency. For some common conductors, Table 3.1 gives their resistivity and skin depth at various frequencies.

Table 3.1. Resistivity and skin depth of some common conductors.

Conductor	Resistivity ($\Omega \cdot \text{m}$)	Skin Depth (m)				
		$f=60 \text{ Hz}$	$f=10^3 \text{ Hz}$	$f=10^4 \text{ Hz}$	$f=10^5 \text{ Hz}$	$f=10^6 \text{ Hz}$
Silver	1.59×10^{-8}	8.19×10^{-3}	2.01×10^{-3}	6.35×10^{-4}	2.01×10^{-4}	6.35×10^{-5}
Copper	1.68×10^{-8}	8.42×10^{-3}	2.06×10^{-3}	6.52×10^{-4}	2.06×10^{-4}	6.52×10^{-5}
Aluminium	2.82×10^{-8}	1.09×10^{-2}	2.67×10^{-3}	8.45×10^{-4}	2.67×10^{-4}	8.45×10^{-5}
Iron	1.00×10^{-7}	6.50×10^{-4}	1.59×10^{-4}	5.03×10^{-5}	1.59×10^{-5}	5.03×10^{-6}
Tin	1.09×10^{-7}	2.14×10^{-2}	5.26×10^{-3}	1.66×10^{-3}	5.26×10^{-4}	1.66×10^{-4}
Lead	2.20×10^{-7}	3.05×10^{-2}	7.46×10^{-3}	2.36×10^{-3}	7.46×10^{-4}	2.36×10^{-4}

In Table 3.1, from top to bottom, conductors are arranged with increasing resistivity, but the skin depth is also increasing for a same frequency, except for iron, whose skin depth is comparatively small due to high relative permeability. Therefore, there is a tradeoff between low resistivity and large skin depth. Considering that the operating frequency does not exceed 1 MHz, the thickness of the conductor layer will not be less than 50 μm . Copper is chosen as the material of conductor layer because its resistivity is comparatively small and it is available for the thickness of 50 μm .

3.4.2 Dielectric Layer

As for dielectric materials, factors such as relative permittivity, dissipation factor and dielectric strength are major considerations. Relative permittivity of a material, defined as the ratio of its absolute permittivity to the permittivity of vacuum, is an important parameter when forming capacitors. The simplest capacitor is the parallel-plate model as shown in Fig. 3.10, consisting of two parallel conductive plates separated by a dielectric with permittivity ϵ . Its capacitance is given by:

$$C = \frac{\epsilon S}{d} = \frac{\epsilon_0 \epsilon_r A}{d}, \quad (3.24)$$

where ϵ_0 is the permittivity of vacuum, ϵ_r is the relative permittivity, A is the area of the conductive plate, and d is the distance between the plates. Therefore a large capacitance is determined by high permittivity of dielectric materials, large plate area, and small separation.

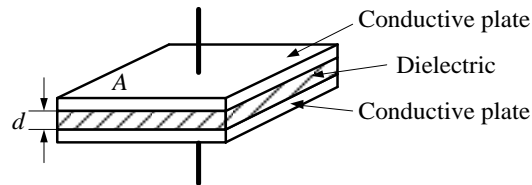


Fig. 3.10. Parallel-plate capacitor.

Dissipation factor, which is the reciprocal of quality factor, is a measure of loss-rate of energy of oscillation in a dissipative system. In dielectric materials, electrical potential energy is usually dissipated in the form of heat. A more practical lumped element model for a capacitor made of dielectric placed between conductors includes an ideal capacitor in series with a resistor named equivalent series resistance. A good capacitor usually has a small equivalent series resistance, so the loss-rate of energy is low, i.e., the dissipation factor is small. Typically, the dissipation factor of a dielectric material increases with increased thickness.

The dielectric strength of an insulating material is a measure of the capability of withstanding electric field without breaking down. It is defined as the maximum electric field which an insulating material can withstand under ideal conditions before breaking down. Generally, dielectric strength decreases with increased frequency and slightly increases with increased thickness. Therefore, the dielectric strength of the material chosen should be strong enough to endure the voltage across two successive conductor layers at a frequency up to 1 MHz.

Based on all above considerations, NOMEX[®] Type 410 insulation paper is chosen for dielectric layers. Its main properties are listed in Table 3.2.

Table 3.2. Main properties of NOMEX[®] Type 410 insulation paper.

Thickness (μm)	Relative permittivity	Dissipation factor	Dielectric strength (kV/mm)
50	2.5	4×10^{-3}	17

3.4.3 Ferrite Core

As introduced in Section 2.3, there are many parameters describing the property of ferromagnetic materials. For choosing ferrite core, permeability, frequency range and core losses are mainly considered. EPCOS[®] N87 MnZn is one of the ferrites recommended by WPC for IPT systems. Its products can be manufactured into many shapes, such as cylindrical rod, E-shape core, toroidal core, pot core and so on. The main properties of N87 are listed in Table 3.3.

Table 3.3. Main properties of EPCOS[®] N87 MnZn ferrite.

Initial permeability	Flux density ($H=1200$ A/m, $f=10$ kHz) (mT)	Coercive field strength ($f=10$ kHz) (A/m)	Frequency range (kHz)	Curie temperature ($^{\circ}\text{C}$)
2200 \pm 25%	490	21	25~500	>210

3.5 Prototypes of the Resonant Coil

According to the previous section, some main parameters of the prototypes of the resonant coil are summarized in Table 3.4.

Table 3.4. Main parameters of the resonant coil.

Parameter	Value	Parameter	Value
Outer diameter	59 mm	Overlap angle	170 $^{\circ}$
Inner diameter	29 mm	Relative permeability of ferrite core	2200
Thickness of conductor layer	50 μm	Relative permeability of dielectric	2.5
Thickness of dielectric layer	50 μm	Relative permeability of glue	2.0

Water-based glue is used to stick two adjunct layers together. The whole stack is compressed by high pressure until extra glue exudes from the edges of

the layers and solidifies. To verify little influence by the glue, the thickness of a 16-unit stack is measured by a vernier scale before and after glued. The average difference is less than 0.2 mm. Since every successive layers have a glue layer in between, the average thickness of a glue layer is less than 3.3 μm , which is 6.6% of that of a dielectric layer. The relative permittivity of the glue is measured to be 2.0, similar to that of dielectric layers. Thus, the glue layer has little influence on the capacitances of C_0 and C_1 [70].

Then, we can calculate the resistance R_0 , inductance L_0 and capacitance C_0 of each unit based on the previous derivations:

$$\begin{aligned} R_0 &= \frac{3.14 \times 1.68 \times 10^{-8}}{5 \times 10^{-5} \times \ln \frac{58}{30}} \\ &= 1.60 \times 10^{-3} \Omega \quad , \\ &= 1.60 \text{ m}\Omega \end{aligned} \quad (3.25)$$

$$\begin{aligned} L_0 &= \frac{4 \times 3.14 \times 10^{-10} \times 2300 \times (59+29)}{4} \left[\ln \frac{8(59+29)}{59-29} - 2 \right] \\ &= 7.03 \times 10^{-5} \text{ H} \quad , \\ &= 70.3 \mu\text{H} \end{aligned} \quad (3.26)$$

$$\begin{aligned} C_0 &= \frac{8.85 \times 10^{-12} \times 2.5 \times 170 \times 3.14 \times (59^2 - 29^2) \times 10^{-6}}{180 \times 8 \times 5 \times 10^{-5}} \\ &= 4.33 \times 10^{-10} \text{ F} \quad . \\ &= 0.433 \text{ pF} \end{aligned} \quad (3.27)$$

According to (3.23), the theoretical relationship between the resonant frequency and the number of units are illustrated using a dash line in Fig. 3.11. Correspondingly, the distributed circuit models are simulated in LTspice and prototypes with varying number of units are measured to verify the relationship. The results are also illustrated in Fig. 3.11. As shown, the simulation results are consistent with the theory curve. The discrepancies between the experiment and simulation are caused by the assumption that in the simulation the coil is tightly surrounded by a uniform ferrite, so the permeability of the ferrite is used when

calculating L_0 . However, in practice, the winding area of the ferrite core is not completely filled up and leaves an air space. When the number of units is small, some of the flux passes through the air space, resulting in a decrease of self-inductance. As the number of units increases, the winding area of the ferrite core is gradually filled up by the stack. The portion of the flux passing through the air space reduces so that the decrease of self-inductance is not significant and the prototyped coil is more closed to the model in the simulation.

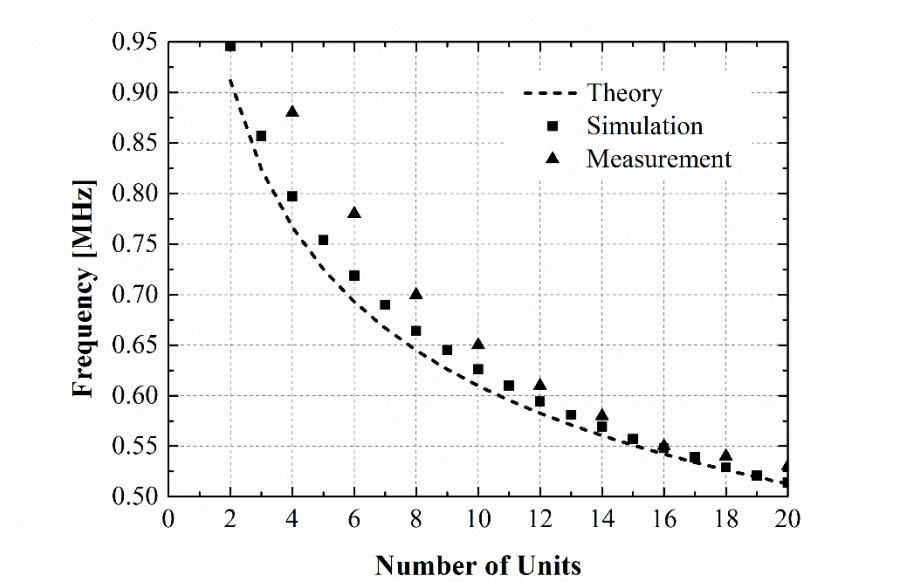


Fig. 3.11. The resonant frequency versus the number of coil units by theoretical calculations, simulations and experimental measurements.

In the simulation, if we reduce the self-inductance of each distributed inductor proportionally to the occupancy ratio of the air space, i.e., a large reduction for low unit count and a small reduction for high unit count, the resulting resonant frequencies are more closed to that of experiment results as shown in Fig. 3.12. Therefore, based on the above analysis, there is a relative large discrepancy between the simulation and measurement for low unit count, but an acceptable discrepancy less than 4% when the number of units is 14 or above.

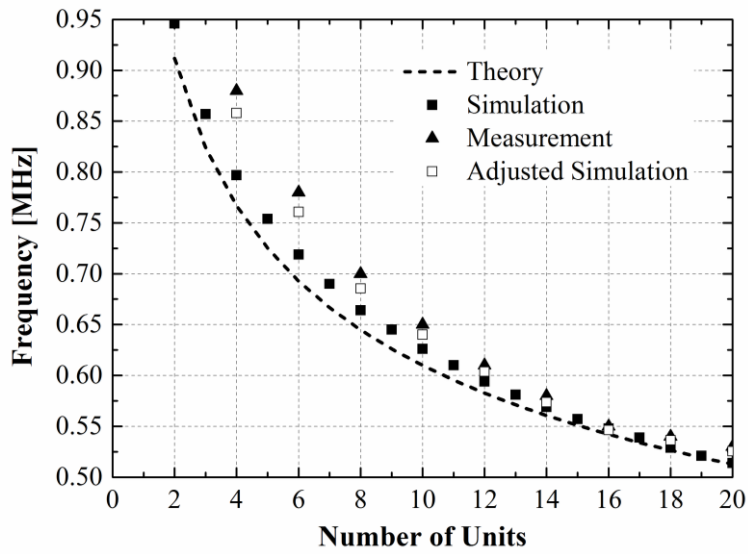


Fig. 3.12. The resonant frequency versus the number of coil units by theoretical calculations, simulations, experimental measurements, and adjusted simulations by decrease of self-inductance.

Considering the practical issues in coil construction, a 16-unit, 8-section resonant coil is prototyped. The whole stack is tightly compacted and assembled in the winding area of the ferrite core as shown in Fig. 3.13. In Fig. 3.14, the resonant coil is measured by an impedance analyzer showing that the value of Q is 1200 at the resonant frequency of 550 kHz.

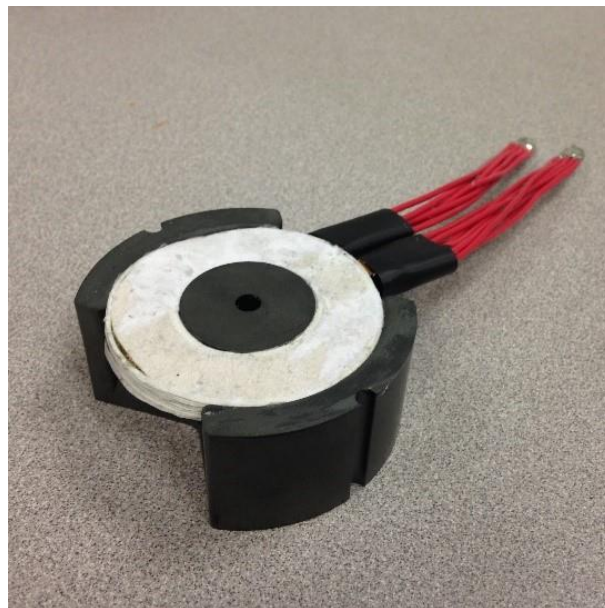


Fig. 3.13. Photograph of a 16-unit resonant coil prototype.

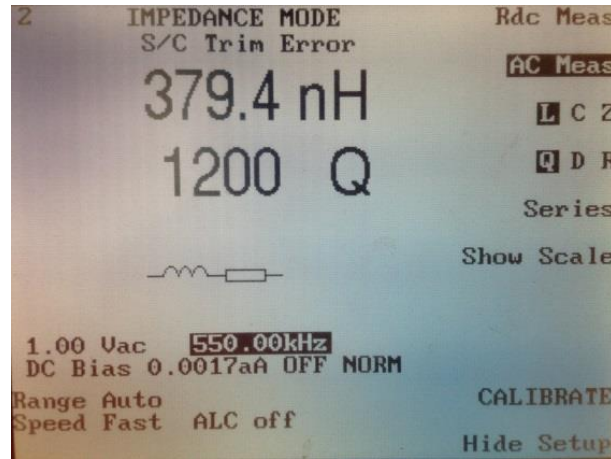


Fig. 3.14. Q of 1200 measured at the resonant frequency of 550 kHz.

3.6 Summary

In this chapter, the novel design on the structure of high-Q resonant coil is introduced and fabricated. To overcome the disadvantages of low Q and high cost at high frequencies of traditional coils made of litz wire, the proposed coil structure is an integration of C-shaped conductor layers and toroid-shaped dielectric layers alternately stacked. The stack usually contains several sections and only the top conductor layer in each section has terminals connected to the external circuit. A useful definition of unit, which consists of two successive conductor layers with an overlap angle θ and one dielectric layer in between, is given and its current distribution is simulated. Based on the simulation, the distributed circuit model for a unit is simplified by the lumped circuit model of RLC and the values of RLC components are derived. Further, the equivalent circuit for the coil is built and the function of resonant frequency is derived based on reflected impedance.

As for the materials of the coil prototypes, 50 μm thick copper sheet and 50 μm thick insulation paper are used for conductor layers and dielectric layers, respectively. The ferrite core used is N87 MnZn with a relative permeability of

2200. The resonant frequencies of prototypes with various numbers of units are measured to verify the theoretical derivation and simulation results. Finally, a 16-unit, 8-section resonant coil with a measured Q of 1200 at the resonant frequency of 550 kHz is fabricated and implemented in the proposed IPT system in the next chapter.

Chapter 4

Design and Construction of the IPT System

4.1 Introduction

In this chapter, the whole IPT system is established for portable device charging applications. Firstly, in Section 4.2, the overview of the structure of the IPT system, consisting of a primary subsystem and a secondary subsystem, is presented. Then, each module of the IPT system is introduced in detail. For the primary circuit, in Section 4.3, the half-bridge circuit is comprehensively analyzed for all states within one cycle, and the properties of MOSFET and gate driver chip chosen are given. In Section 4.4, series type of compensating is implemented in the resonant tank and the value of compensating capacitor is calculated. In order to maintain the resonant status when operating conditions vary, a frequency tracking unit is applied to counterbalance the change of resonant frequency in Section 4.5. In Section 4.6, a standby mode is designed to reduce energy consumption when the secondary side is absent. For the secondary circuit, properties of secondary coil are given in Section 4.7, and the value of secondary compensating capacitor is calculated. In Section 4.8, full-wave rectifier to convert sinusoidal AC output voltage of the secondary coil to DC voltage is introduced, and this variable high DC voltage is further converted to a constant and stable DC voltage by a DC/DC converter for portable device charging in Section 4.9. This chapter is concluded in Section 4.10.

4.2 Structure of the IPT System

The proposed IPT system is made of two subsystems, namely primary circuit subsystem and secondary circuit subsystem as shown in Fig. 4.1. In the primary circuit subsystem, the voltage output from a DC power supply is firstly converted to a high-frequency square wave by a half-bridge inverter. Then, the square-wave voltage is applied across the resonant tank, which contains a high-Q resonant coil and a compensating capacitor. The frequency of the square wave is controlled by a frequency tracking unit which uses the phase lock loop circuit as a feedback to ensure that the resonant status of the resonant tank is always maintained. In the secondary circuit subsystem, the secondary coil is also connected to a compensating capacitor and the induced AC voltage output is converted to a pulsating DC voltage by a full-wave rectifier and regulated by a DC/DC converter so as to generate a constant and suitable DC voltage for portable device charging. The primary circuit subsystem and the secondary subsystem are connected through inductive coupling of the primary coil and the secondary coil.

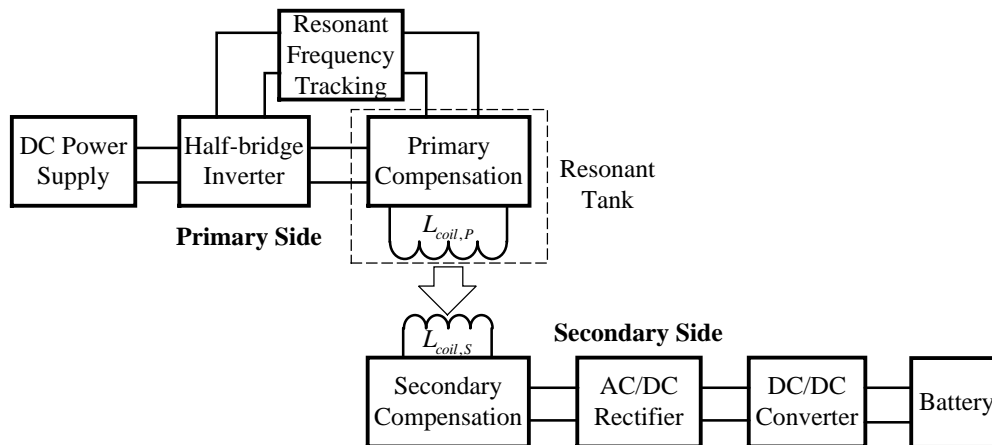


Fig. 4.1. Block diagram of the IPT system consisting of a primary circuit subsystem and a secondary circuit subsystem.

4.3 Drive Circuit

4.3.1 Half-Bridge Circuit

Half-bridge circuit implemented in the IPT system plays a role as a high-frequency AC voltage source across the resonant tank to generate the varying magnetic field. The half-bridge circuit consists of an upper and lower switch, typically MOSFETs, connected in a cascade arrangement as shown in Fig. 4.2. This 5-terminal circuit includes a DC bus voltage input (1), a mid-point between the two switches (2), a ground return (3), a low-side gate drive input (4), and a high-side gate drive input (5). The output capacitance and the anti-parallel diode of each switch are also included in the circuit.

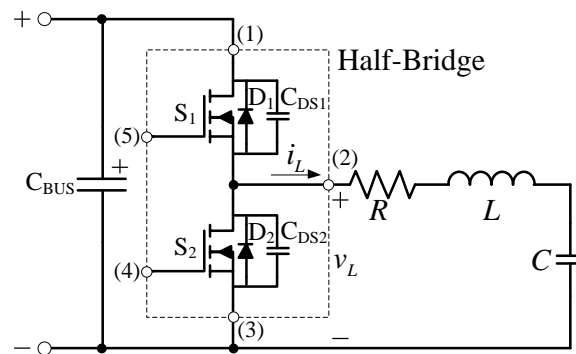


Fig. 4.2. Half-bridge circuit with a series RLC load.

The two switches are turned on and off complementary to each other with a non-overlapping dead-time by applying the correct voltage waveforms at each of the gate drive inputs. The output is a square-wave voltage at the mid-point which switches between the DC bus voltage and ground. With a series RLC load connected between the mid-point and ground, an AC current is produced through the load as the square-wave at the mid-point oscillates up and down. The voltage and current waveforms of the half-bridge circuit can be explained by dividing a cycle into the following six time zones in Fig. 4.3. Corresponding diagrams of switch states and current directions are given in Fig. 4.4.

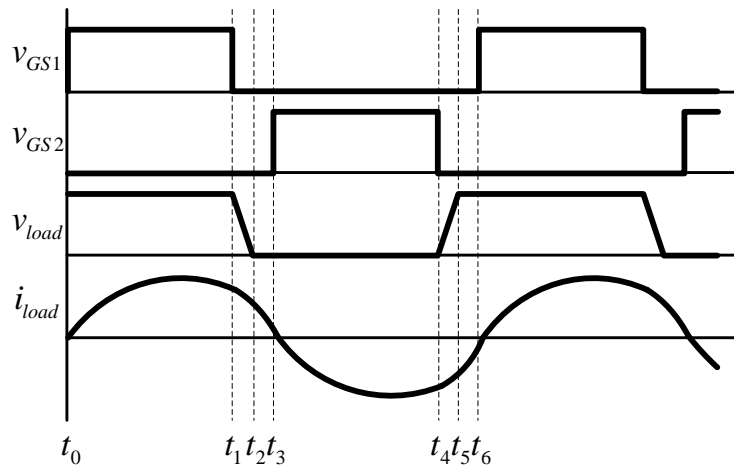


Fig. 4.3. Operating waveforms of the half-bridge circuit.

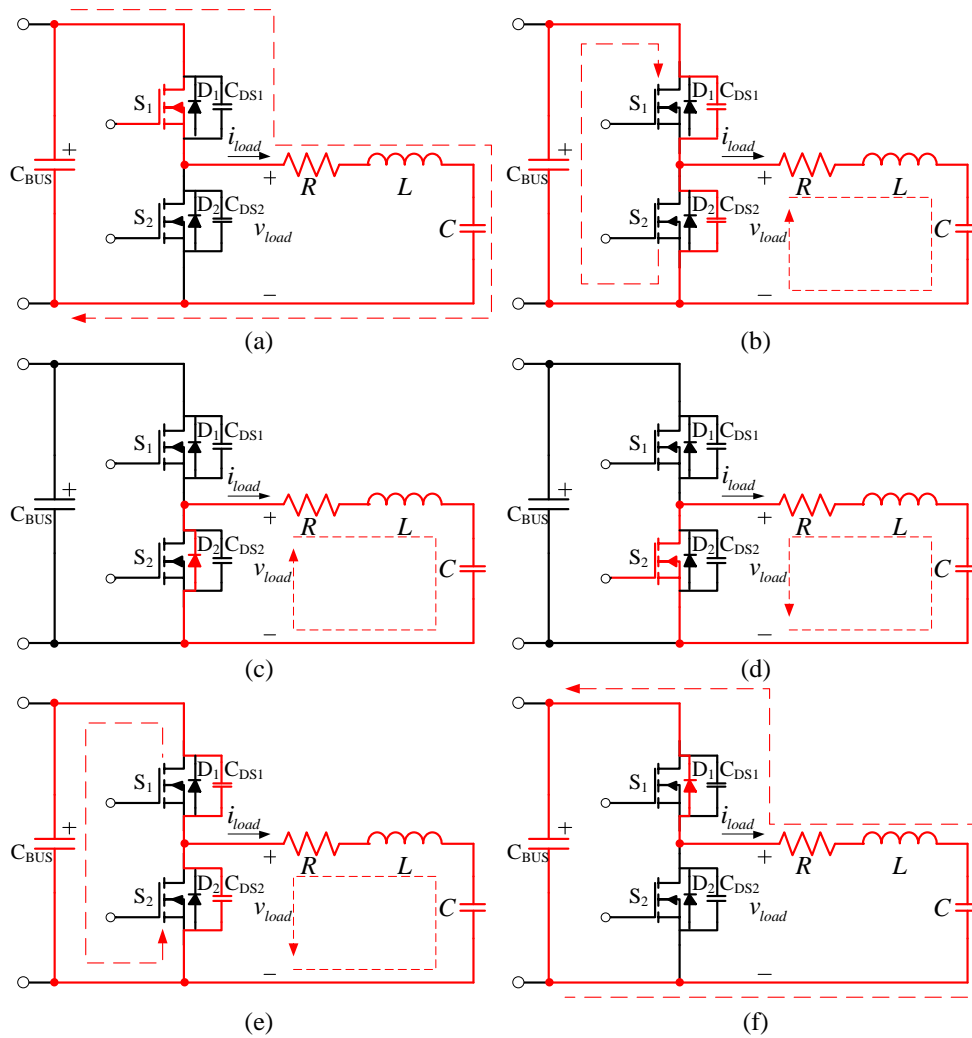


Fig. 4.4. Operating status and current paths (red) of the half-bridge circuit: (a) Zone I ($t_0 \sim t_1$), (b) Zone II ($t_1 \sim t_2$), (c) Zone III ($t_2 \sim t_3$), (d) Zone IV ($t_3 \sim t_4$), (e) Zone V ($t_4 \sim t_5$), and (f) Zone VI ($t_5 \sim t_6$).

Zone I ($t_0 \sim t_1$): This state is shown in Fig. 4.4(a), where S_1 is on and S_2 is off. When $t=t_0$, S_1 is on and the mid-point is connected to the DC bus voltage, as well as the output capacitance of S_2 . Current flows from the positive side of the DC bus, through the upper switch, through the RLC load, and back to the (-) ground return path. The current ramps up to a positive peak level during the on-time of S_1 . When $t=t_1$, S_1 turns off.

Zone II ($t_1 \sim t_2$): This state is shown in Fig. 4.4(b), where S_1 and S_2 both turn off during this short dead-time. The load current continues to flow out of the mid-point node. Part of the load current flows out of the top of the output capacitance of S_2 , and the other part flows out of the bottom of the output capacitance of S_1 , i.e., C_{DS1} is charging and C_{DS2} is discharging. This causes the mid-point voltage to slew down to ground. At the end of this state, C_{DS2} is fully discharged, so the mid-point voltage becomes 0.

Zone III ($t_2 \sim t_3$): This state is shown in Fig. 4.4(c), where S_1 and S_2 still remain off. When $t=t_2$, the voltage across C_{DS1} equals to DC bus voltage and the voltage across C_{DS2} equals to 0. The voltages across the two output capacitors will no longer change. The load current only flows through the internal antiparallel diode D_2 of the lower MOSFET. This diode, also known as the free-wheeling diode, allows the current to flow in the negative direction while the switch is off.

Zone IV ($t_3 \sim t_4$): This state is shown in Fig. 4.4(d), where S_1 is off and S_2 is on. When $t=t_3$, S_2 is on, the mid-point voltage continues to be at ground and current flow through the load from the channel of S_2 instead of the diode D_2 due to the lower resistance of the channel. The current crosses zero and continues to ramp down to a negative peak level during the on-time of S_2 . No current flows through the DC bus capacitor during this time.

Zone V ($t_4 \sim t_5$): This state is shown in Fig. 4.4(e), where S_1 and S_2 both turn off during this dead-time. Similar as Zone II, the load current continues to flow into the mid-point node and is split between C_{DS1} and C_{DS2} . Thus, C_{DS1} is discharging and C_{DS2} is charging. This causes the mid-point voltage to rise up to the DC bus voltage. At the end of this state, C_{DS1} is fully discharged, so the mid-point voltage becomes V_{DC} .

Zone VI ($t_5 \sim t_6$): This state is shown in Fig. 4.4(f), where S_1 and S_2 still remain off. Similar as Zone III, when $t=t_5$, the voltage across C_{DS2} equals to DC bus voltage and the voltage across C_{DS1} equals to 0. The voltages across the two output capacitors will no longer change. The load current only flows through the internal antiparallel diode D_1 of the upper MOSFET.

4.3.2 Power MOSFETs

The power MOSFETs implemented in the half-bridge circuit are IRF640N from International Rectifier [71]. It has characteristics of low on-resistance with the maximum value of 0.15Ω and fast switching speed. Its dynamic electrical characteristics are listed in Table 4.1 to verify that IRF640N is suitable for high-frequency applications. In order to reduce the switching loss, the switching frequency is chosen as 100 kHz.

Table 4.1. Dynamic electrical characteristics of IRF640N [71].

Turn-on delay time (ns)	Rise time (ns)	Turn-off delay time (ns)	Fall time (ns)
10	19	23	5.5

4.3.3 Gate Drive Circuit

The half-bridge requires a low-side gate driver, referenced to ground, for switching the lower MOSFET, and a “floating” high-side gate driver, referenced to the mid-point, for switching the upper MOSFET. The gate drive chip selected in this project is IR2111 from International Rectifier [72]. It is a high speed

power MOSFET driver with one logic input channel, IN, and two dependent high and low side referenced output channels, HO and LO. The input and output logic timing diagram is shown in Fig 4.5. Internal dead-time is provided to avoid short circuit in the half-bridge circuit and is proper for IRF640N power MOSFET.

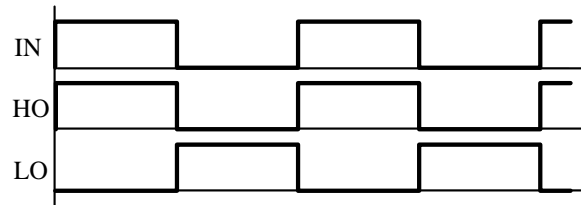


Fig. 4.5. Input and output logic timing of IR2111.

The circuit connection between the gate driver and the half-bridge is shown in Fig. 4.6. Anti-parallel diodes, D_{G1} and D_{G2} , are respectively placed in parallel with the gate resistor R_{G1} and R_{G2} to discharge the gate capacitances quickly during turn-off and minimize switching losses.

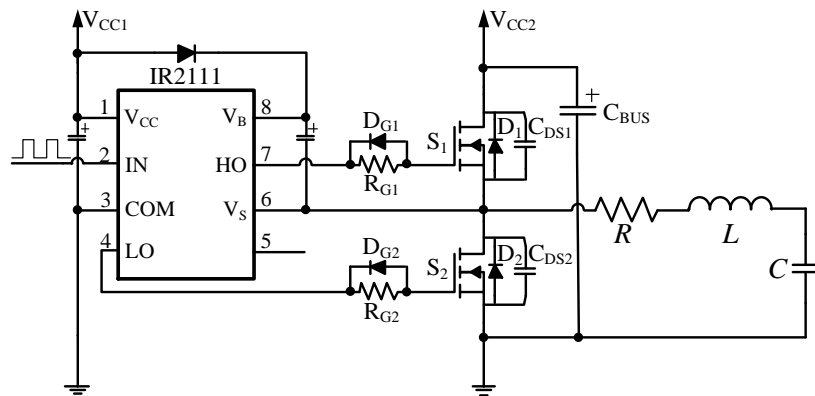


Fig. 4.6. Schematic diagram of the gate driver and the half-bridge with a series RLC load.

4.4 Resonant Tank

The resonant tank consists of a high-Q resonant coil proposed in the previous chapter and its compensating capacitor. A series type of compensation

is adopted here for the convenience of frequency tracking usage which is introduced in the next section.

In order to have a resonant frequency of 100 kHz, the value of the series compensating capacitor should be selected according to (2.60). For a measured inductance of 379.4 nH of the resonant coil used, the primary compensating capacitance is calculated by:

$$\begin{aligned} C_p &= \frac{1}{\omega_0^2 L_p} \\ &= \frac{1}{(2\pi \times 10^5)^2 \times 379.4 \times 10^{-9}}. \\ &= 6.68 \mu\text{F} \end{aligned} \quad (4.1)$$

4.5 Frequency Tracking Unit

According to Section 2.6, in order to maximize the power transfer efficiency and minimize the VA rating of the power supply in an IPT system, the operating frequency should be closely tuned to or near the resonant frequency of the system. However, in practice, changes of the resonant frequency can happen due to load varying, shift of the position between the coupled coils, temperature changing, deviations of electrical components and so on. Thus, a frequency tracking unit is necessary to be implemented to control the operating frequency of the system to follow the changes of the system resonant frequency. Firstly, the phase properties of the resonant circuit is investigated.

4.5.1 Phase Properties of the Resonant Circuit

In a series RLC resonant circuit, the voltage across the capacitor V_C is given in phasor form in reference to the source voltage V_S by:

$$V_c = \frac{1}{1 - \omega^2 LC + j\omega RC} V_s. \quad (4.2)$$

If the phase of source voltage θ_s is set to be 0, the phase of voltage across the capacitor θ_c is given by:

$$\theta_c = \begin{cases} -\arg\left(\frac{\omega RC}{1 - \omega^2 LC}\right) & \left(\omega < \frac{1}{\sqrt{LC}}\right) \\ -\frac{\pi}{2} & \left(\omega = \frac{1}{\sqrt{LC}}\right) \\ -\arg\left(\frac{\omega RC}{1 - \omega^2 LC}\right) - \pi & \left(\omega > \frac{1}{\sqrt{LC}}\right) \end{cases}. \quad (4.3)$$

The phase difference between V_s and V_c is:

$$\Delta\theta = \theta_s - \theta_c. \quad (4.4)$$

The relationship between the operating frequency and the phase difference is illustrated in Fig. 4.7.

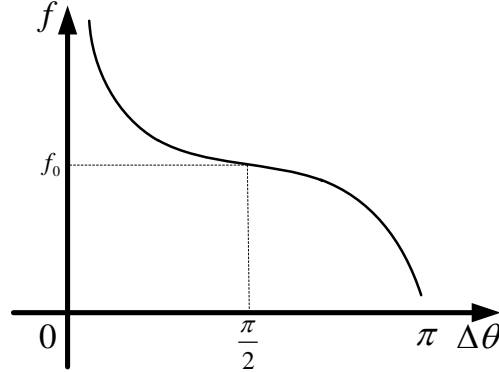


Fig. 4.7. Operating frequency versus the phase difference between the voltage source and capacitor in a series RLC circuit.

4.5.2 Phase-Locked Loop

The phase-locked loop (PLL) consists of three fundamental functional blocks as shown in Fig. 4.8 [73-75]:

- 1) A phase detector. (PD).
- 2) A loop filter. (LF).

3) A voltage-controlled oscillator. (VCO).

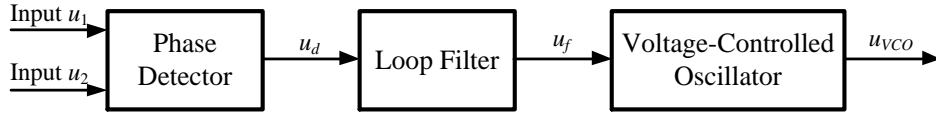


Fig. 4.8. Block diagram of the PLL.

The PD, also referred to as phase comparator, compares the phases of two signals and develops an output signal u_d consisting of a DC component and a super-imposed AC component. Its average value u_{d0} is approximately proportional to the phase difference $\Delta\theta$. This relationship can be written as:

$$\Delta\theta = \theta_1 - \theta_2, \quad (4.5)$$

$$u_{d0} = K_d \Delta\theta, \quad (4.6)$$

where K_d represents the gain of the PD. The AC component is undesired, so typically a first-order, low-pass filter is implemented to cancel it. The output signal of the filter is named u_f .

Then u_f is sent to the input of VCO. The VCO can oscillates at an angular frequency ω_{VCO} , which is determined by u_f . The angular frequency ω_{VCO} is given by:

$$\omega_{VCO} = \omega_0 + K_0 u_f, \quad (4.7)$$

where ω_0 is a pre-set angular frequency of the VCO and K_0 is the gain of the VCO.

4.5.3 PLL Chip

The PLL chip CD4046B [76] from Texas Instrument is applied in this project. Its block diagram is shown in Fig. 4.9. From the diagram, the CD4046B consists of a low-power, linear VCO and two phase comparators, having a common signal-input amplifier and a common comparator input.

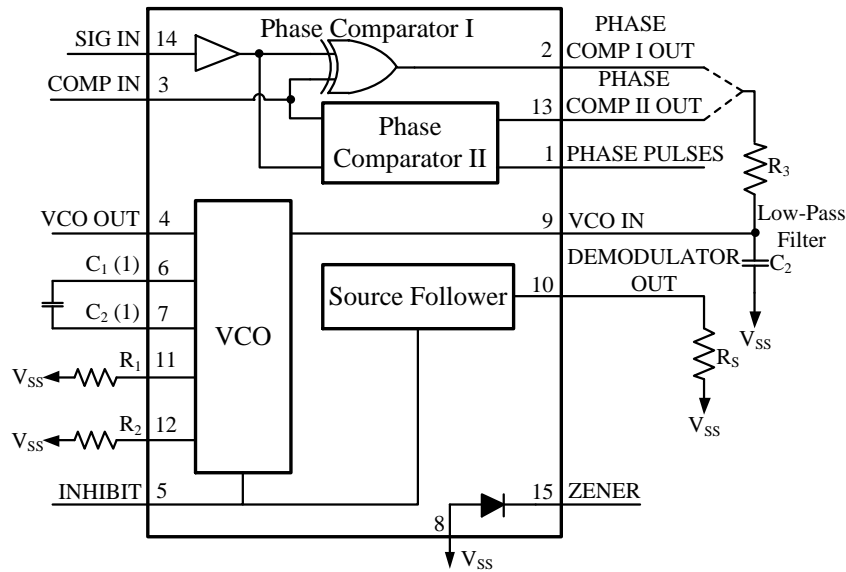


Fig. 4.9. Block diagram of the PLL chip CD4046B.

Phase comparator I is used in the design and it is an exclusive-OR network. The signal input (Pin 14) and comparator input (Pin 3) frequencies must have a 50% duty cycle to obtain the maximum lock range. When there is no signal or noise at the signal input, the average output voltage of the phase comparator is equal to $0.5V_{DD}$, which is supplied to the VCO input (Pin 9) by the low-pass filter connected to the output of phase comparator I (Pin 2). This $0.5V_{DD}$ voltage also causes the VCO to oscillate at the center frequency f_c . A typical behavior of Phase comparator I is that the average output voltage is proportional to the phase difference between the signal input and comparator input varying between 0° and 180° , and is $0.5V_{DD}$ at 90° . Fig 4.10 gives the operating waveforms of phase comparator I and Fig. 4.11 shows its phase-to-output response characteristic.

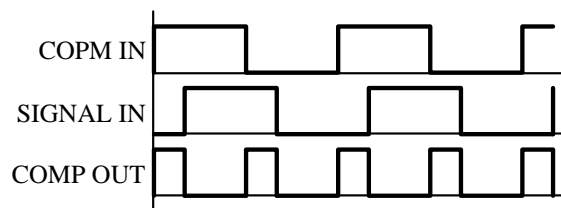


Fig. 4.10. Input and output waveforms of the phase comparator I.

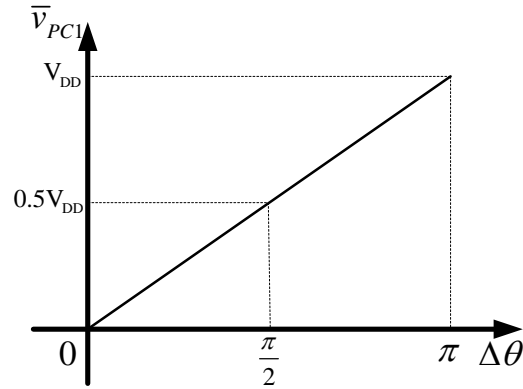


Fig. 4.11. The average output voltage of the phase comparator I versus the input phase difference.

An external low-pass filter is applied. The simplest low-pass filter is passive, first-order low-pass RC filter which consists of a resistor in series with a load, and a capacitor in parallel with the load as shown in Fig. 4.12. At lower frequencies, the capacitor exhibits reactance, and blocks low-frequency signals, forcing them through the load instead. At higher frequencies, the reactance drops, and the capacitor effectively functions as a short circuit. Thus, the average output voltage of phase comparator I can pass the filter with high-frequency ripples filtered out. The break frequency f_{break} , also called the turnover frequency or cutoff frequency, is determined by:

$$f_{break} = \frac{1}{2\pi RC} \quad (4.8)$$

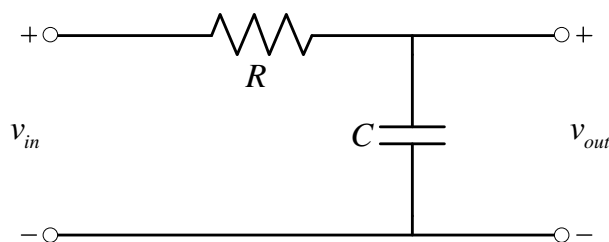


Fig. 4.12. Passive, first-order low-pass RC filter.

The VCO requires an external capacitor C_1 and resistor R_1 with an optional resistor R_2 . R_1 and C_1 determine the frequency range of the VCO, while R_2 enables the VCO to have a frequency offset if required. The center frequency f_c

at $0.5V_{DD}$ input and the frequency range, $f_{max}-f_{min}$, can be set by C_1 , R_1 and R_2 based on the datasheet [76]. The voltage-to-frequency response characteristics both with and without offset are plotted in Fig. 4.13, respectively. A low-level at the inhibit input (Pin 5) enables the VCO and the source follower, while a high-level turns both off to minimize standby power consumption.

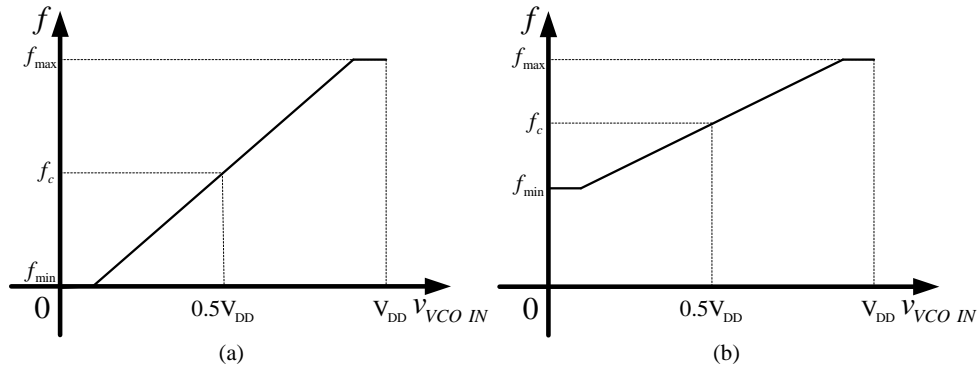


Fig. 4.13. The VCO output frequency versus the input voltage (a) without offset, and (b) with offset.

According to the analysis above, the overall relationship between the VCO output frequency and the input phase difference of phase comparator I is illustrated in Fig. 14.

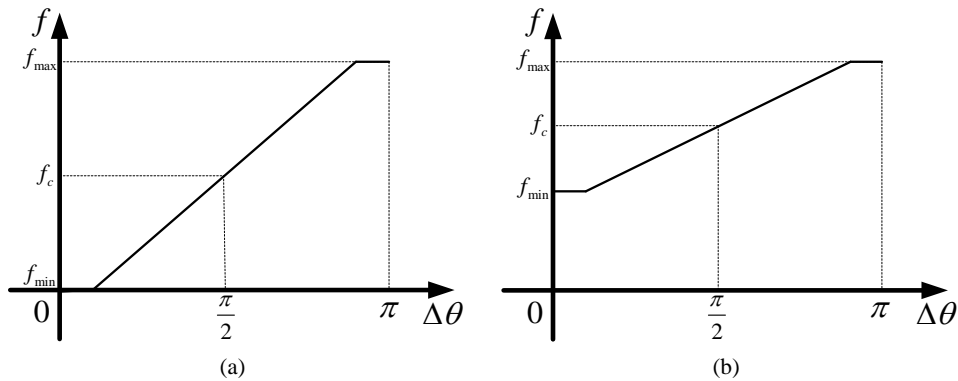


Fig. 4.14. The VCO output frequency versus the input phase difference (a) without offset, and (b) with offset.

The two phase inputs of the frequency tracking unit are from the voltage across the resonant tank and the voltage across the primary compensating capacitor. When resonance occurs, the phase of the voltage across the resonant

tank is 90° leading the phase of the voltage across the primary compensating capacitor. The center frequency of the PLL is set to be the resonant frequency when the secondary coil is best positioned next to the primary coil. When the secondary coil is moving away from the best position, the mutual inductance will decrease, which results in the increase of the system resonant frequency. The output of the frequency tracking unit will respond to compensate the change of the resonant frequency. This procedure is graphically explained in Fig. 4.15, which combines the phase difference-to-frequency characteristics of the resonant tank and frequency tracking unit. The operating point P is where the pre-set center frequency equals to the system resonant frequency at the best coil positioning. A movement of the secondary coil leads to a raise of the characteristic curve of the resonant tank. The new operating point is now the cross-over point P', which has a higher operating frequency than before to cater the change of the system resonant frequency. Within the frequency range, the frequency tracking unit can keep the system operating frequency very close to the system resonant frequency.

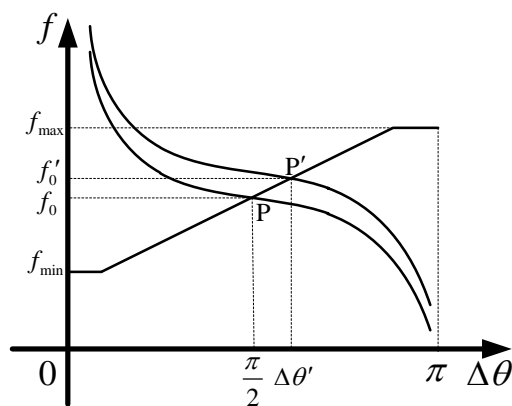


Fig. 4.15. Combined characteristic curves of the resonant tank and the frequency tracking unit.

4.6 Standby Unit

A standby mode is necessary for the IPT system to achieve low energy consumption when the secondary side is absent. The designed standby unit consists of a dual-limit window comparator and a 555 timer IC. Its schematic diagram is shown in Fig. 4.16.

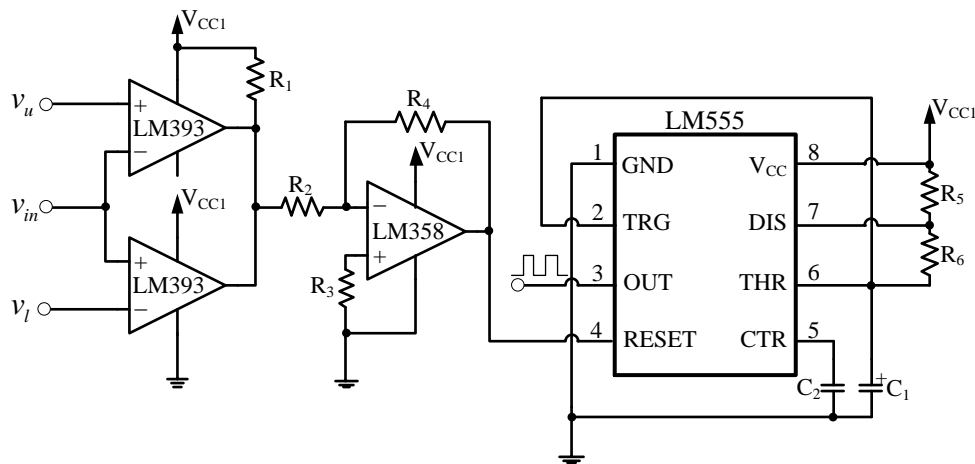


Fig. 4.16. Schematic diagram of the standby unit.

The dual-limit window comparator is built using LM393 with an upper voltage level v_u and a lower voltage level v_l . If the input voltage v_{in} is between the upper level and lower level, the output will swing to the logical low, otherwise the output will swing to the logical high. The operating waveforms are illustrated in Fig. 4.17.

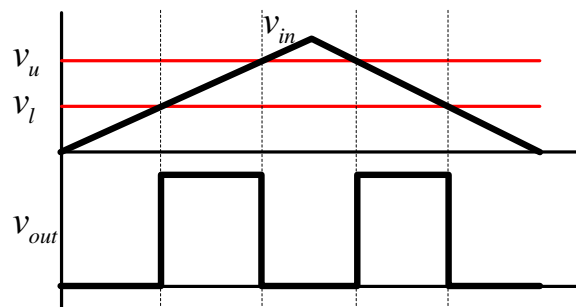


Fig. 4.17. Operating waveforms of the dual-limit window comparator.

The output of the window comparator passes through an inverting amplifier and are connected to the reset (Pin 4) of the 555 timer. When the reset is logical high, the 555 operates at the astable mode and puts out a continuous stream of rectangular pulses at the output (Pin 3) with a specific frequency. The frequency depends on the value of R_5 , R_6 and C_1 in Fig. 4.16 by:

$$f = \frac{1}{C_1 (R_5 + 2R_6) \ln 2}. \quad (4.9)$$

For each pulse, the high time T_h and the low time T_l are given by:

$$T_h = C_1 (R_1 + R_2) \ln 2, \quad (4.10)$$

$$T_l = C_1 R_2 \ln 2. \quad (4.11)$$

The standby unit is connected to the frequency tracking unit by the input from Pin 9 of the PLL chip and the output to Pin 5 of the PLL chip. When the secondary coil is absent, the resonant frequency of the system increases significantly, resulting that the operating point in Fig. 4.15 slips to the upper limit of the VCO output frequency. At this time, the VCO input voltage (Pin 9) is close to V_{DD} . If the upper voltage level of the window comparator is set slightly lower than V_{DD} , the output of the window comparator will flip to logical low and the 555 will begin to produce rectangular pulses. During the low time, the PLL chip will be inhibited by the output for energy saving. During the high time, the PLL chip will be enabled by the output to detect the existence of the secondary coil. Therefore, the standby unit shuts down the system when the secondary coil is absent, and enables the frequency tracking unit once in a while in case that the secondary coil is present.

4.7 Secondary Coil

The secondary coil is selected from the wireless power products of Würth Electronics [77]. The dimensions are illustrated in Fig .4.18. It matches the dimensions of primary coil and is suitable for placing into portable devices. Fig. 4.19 is a photograph of a real secondary coil.

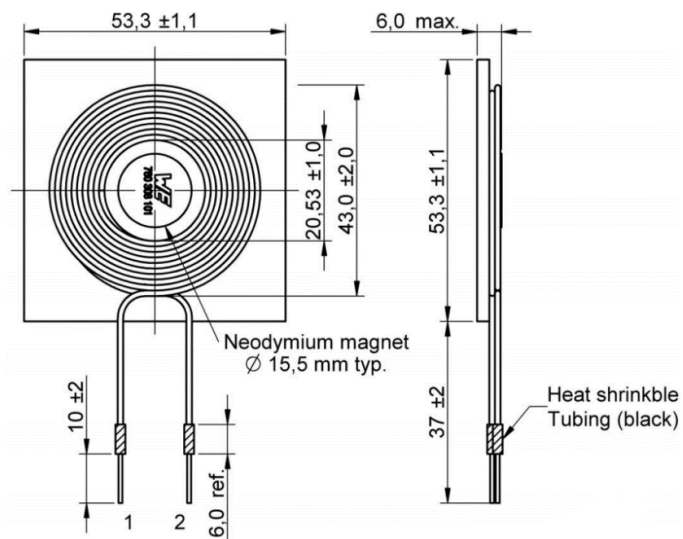


Fig. 4.18. Dimensions of the secondary coil (mm) [77].

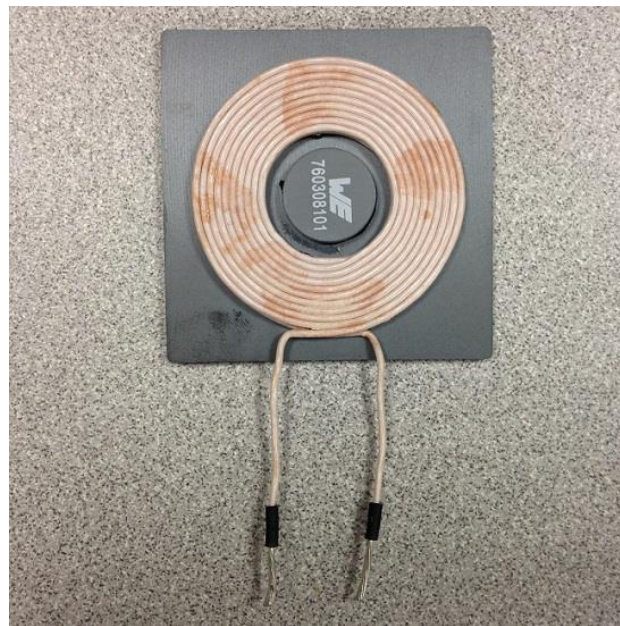


Fig. 4.19. Photograph of the secondary coil.

This two-layer secondary coil has a relatively small DC resistance and a relatively large inductance, which contribute to a good value of Q at resonance. The magnet in the center helps to align with the primary coil for better coupling. Its main electrical properties are listed in Table 4.2.

Table 4.2. Electrical properties of the secondary coil [75].

Properties	Value
Inductance (μH)	24 \pm 10%
DC resistance (Ω)	0.07
Q	90
Rated current (A)	6.0
Self-resonant frequency (MHz)	6

Parallel compensation is adopted for the secondary coil. For the resonant frequency of 100 kHz, the value of the secondary compensating capacitor is calculated according to (2.59):

$$\begin{aligned}
 C_s &= \frac{1}{\omega_0^2 L_s} \\
 &= \frac{1}{(2\pi \times 10^5)^2 \times 24 \times 10^{-6}}. \\
 &= 106 \text{ nF}
 \end{aligned} \tag{4.12}$$

4.8 Full-Wave Rectifier

A rectifier is an electrical circuit that converts AC current to DC current. A full-wave rectifier converts the whole of the input waveform to one of constant polarity, positive or negative, at its output, i.e., full-wave rectification converts both polarities of the input waveform to pulsating DC. For single phase AC current, four diodes in a bridge configuration form a full-wave rectifier as shown in Fig 4.20(a) and its waveforms are shown Fig. 4.20(b).

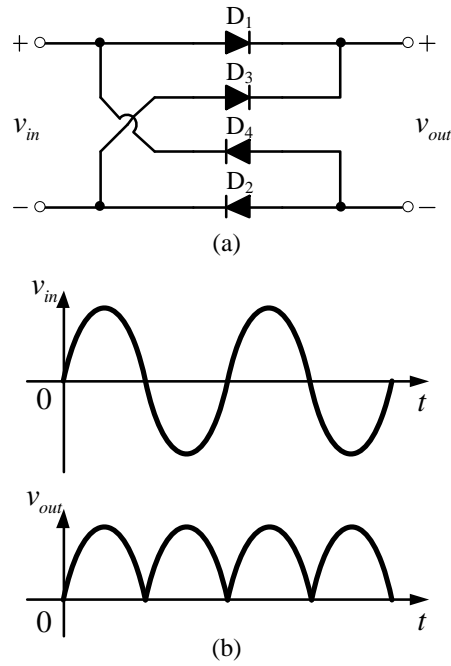


Fig. 4.20. Full-wave rectifier: (a) bridge configuration using four diodes, and (b) input and output waveforms.

Among these four diodes, only two diodes conduct current during each half cycle. During the positive half cycle of the input, diodes D_1 and D_2 conduct in series while diodes D_3 and D_4 are reverse biased. During the negative half cycle of the input, diodes D_3 and D_4 conduct in series while diodes D_1 and D_2 are reverse biased.

The average and root-mean-square output voltages of an ideal single-phase full-wave rectifier with a sinusoidal input are given by:

$$V_{avg} = V_{dc} = \frac{2V_p}{\pi}, \quad (4.13)$$

$$V_{rms} = \frac{V_p}{\sqrt{2}}, \quad (4.14)$$

where V_p is the peak value of the input voltage.

Although full-wave rectification can deliver unidirectional current, the voltage output is not constant. A smoothing circuit or filter is required to produce steady DC voltage output. In its simplest form this can be a reservoir

capacitor or smoothing capacitor, placed at the output of rectifier. The reservoir capacitor charges up when the voltage from the rectifier rises above that of the capacitor and then as the rectifier voltage falls, the capacitor provides the required current from its stored charge. The waveforms before and after smoothed are shown in Fig. 4.21.

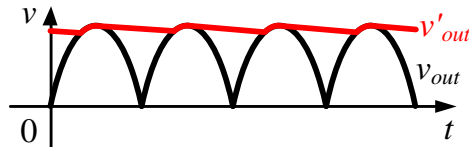


Fig. 4.21. The output waveform of the full-wave rectifier (black) and the waveform after smoothed (red).

The value of the reservoir capacitor must be chosen so that the time constant of the capacitor and the load resistance is much longer than the time of one ripple cycle to produce a smoothed enough DC voltage across the load, i.e.,

$$R_L C_r \gg \frac{1}{f_{ripple}}, \quad (4.15)$$

where f_{ripple} is the ripple frequency, which is twice the frequency of input sine wave if a full-wave rectifier is used.

4.9 DC/DC Converter

In order to convert the variable high DC voltage to a constant and stable DC voltage for portable device charging, A DC/DC converter should be applied. The DC/DC converter is an electrical circuit which converts a DC source from one voltage level to another. The chip selected for the DC/DC converter in this project is LM2576 [78]. The LM2576 is a step-down voltage regulator, capable of driving 3 A load with adjustable output voltage from 1.23 to 37 V. It also has

a wide input voltage range up to 60 V. A typical connection for a fixed 5 V output is shown in Fig. 4.22.

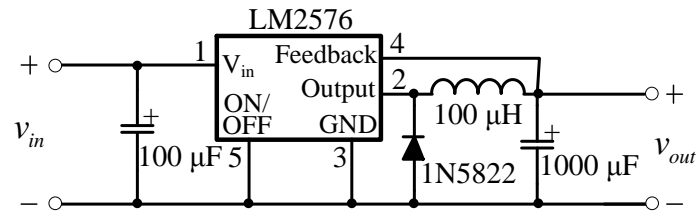


Fig. 4.22. Schematic diagram of LM2576 for a fixed 5 V output.

4.10 Summary

In this chapter, the proposed IPT system for portable device charging is designed. It consists of a primary circuit and a secondary circuit connected by inductive coupling. In the primary circuit, the voltage from a DC power supply is converted to a high-frequency square wave by an inverter using the half-bridge configuration and controlled by IR2111 gate driver. The high-frequency voltage is applied to the resonant tank, including the high-Q resonant coil in series with a 6.68 μF compensating capacitor for the resonant frequency of 100 kHz. In order to keep the resonant status, a frequency tracking unit is designed using PLL circuit. The voltages across the resonant tank and the primary compensating capacitor are sampled as the inputs of the frequency tracking unit. Based on the phase difference between the voltages, the operating frequency is controlled to cater the change of the resonant frequency caused by the movement of the secondary coil within a pre-set tracking range. The standby unit is implemented to reduce the power consumption by shutting down the system when the secondary coil is absent, and enabling the frequency tracking unit once in a while in case that the secondary coil is present.

In the secondary circuit, the coil is made of litz wire wound in a two-layer spiral shape on a ferrite plate with a cylindrical magnet in the center. For the resonant frequency of 100 kHz, the secondary coil is compensated by a 106 nF capacitor. The induced sinusoidal voltage is converted to a pulsating DC voltage by the full-wave rectifier using four-diode configuration. After smoothed by the reservoir capacitor, the high variable DC voltage is regulated by the DC/DC converter LM2576 to obtain a constant and stable 5 V for device charging.

The complete schematic diagram of the IPT system is shown in the appendix, as well as the PCB layout.

Chapter 5

Experimental Results and Discussion

5.1 Introduction

This chapter presents the experimental performances and results of the proposed IPT system. Firstly, the hardware implementation on PCB is presented in Section 5.2. Then, in Section 5.3, testing on the IPT system is conducted and the performances are evaluated based on the resulting waveforms and measurements. In Section 5.4, the overall power transfer efficiency and the coupling efficiency are defined and measured at different coil distances. In Section 5.5, the load power is evaluated and two important characteristics of the IPT system, the power transfer efficiency and transmission distance capability, are compared with related works. This chapter is concluded in Section 5.6.

5.2 Hardware Implementation

Fig. 5.1 shows the hardware implementation of the proposed IPT system on PCB. It contains two separate boards, the primary side and the secondary side. At the primary side, the control circuits, including the gate driver, frequency tracking unit, and standby unit, are built on PCB. The half-bridge circuit and resonant tank are built on busbar outside the PCB due to high-current rating. The primary circuit has two power supply inputs. V_{CC1} is a 12 V DC voltage source supplying the control circuit on the PCB. V_{CC2} is also a DC

power supply applied across the half-bridge circuit for the resonant tank. At the secondary side, the coil is stuck to the board and its two terminals are soldered to the circuit on the PCB. V_{out} is the output of secondary circuit to provide a constant and stable 5 V DC voltage. The dimension of the secondary PCB is 12.5 cm in length and 6.3 cm in width, which is suitable for the fitting in most portable devices. The load in the test is a constant 5 Ω resistor.

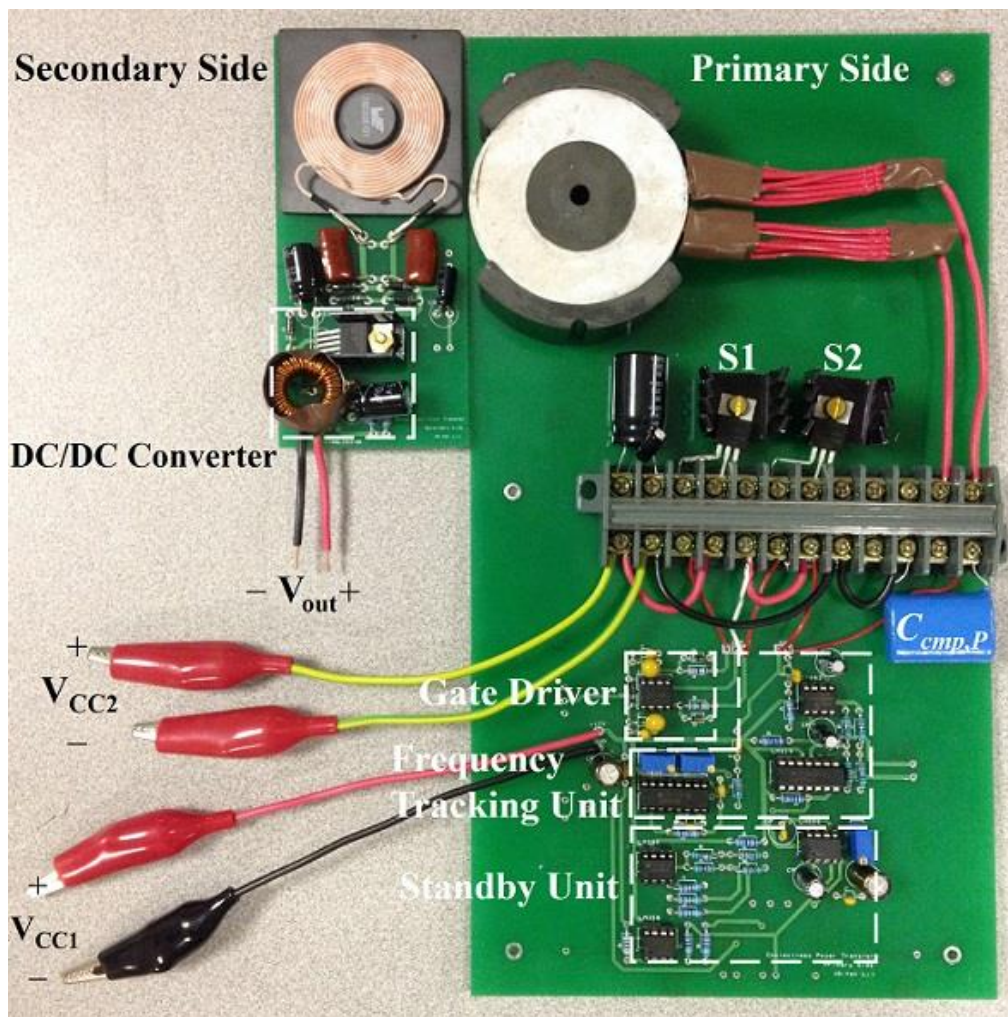


Fig. 5.1. Photograph of the hardware implementation of the IPT system.

5.3 System Testing

5.3.1 Testing of the Half-Bridge Circuit and the Resonant Tank

Fig. 5.2 shows the waveforms of the high-side and low-side gate voltages in the half-bridge circuit. The dead-time measured is about 300 ns. When resonance occurs, the current flowing through the resonant tank I_{tank} gets the maximum value, and the voltage across the compensating capacitor $V_{cmp,P}$ is lagging behind the voltage across the tank V_{tank} by 90° . The experimental resonant frequency is 106 kHz. Relevant waveforms are measured and shown in Fig 5.3.

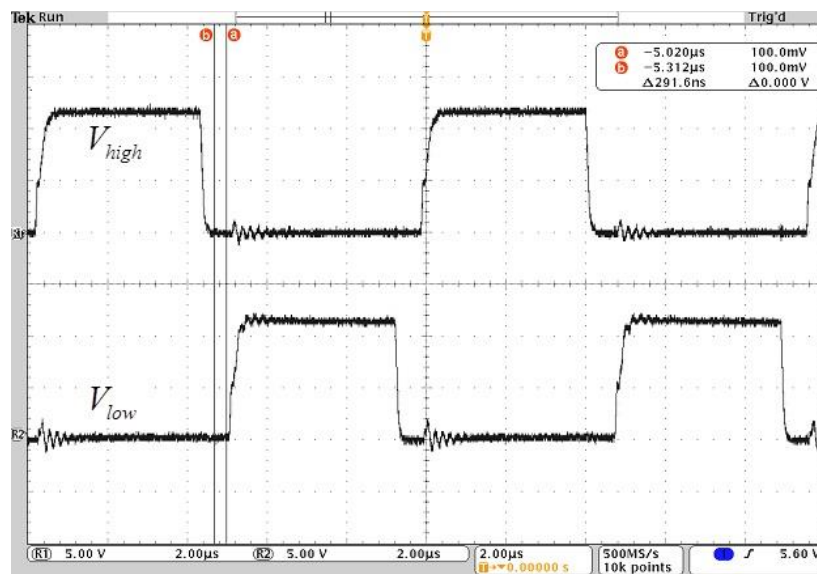


Fig. 5.2. Measured voltage waveforms of the high-side (upper trace, 5 V/div) and low-side (lower trace, 5 V/div) of the gate driver with a measured dead-time of 291.6 ns.

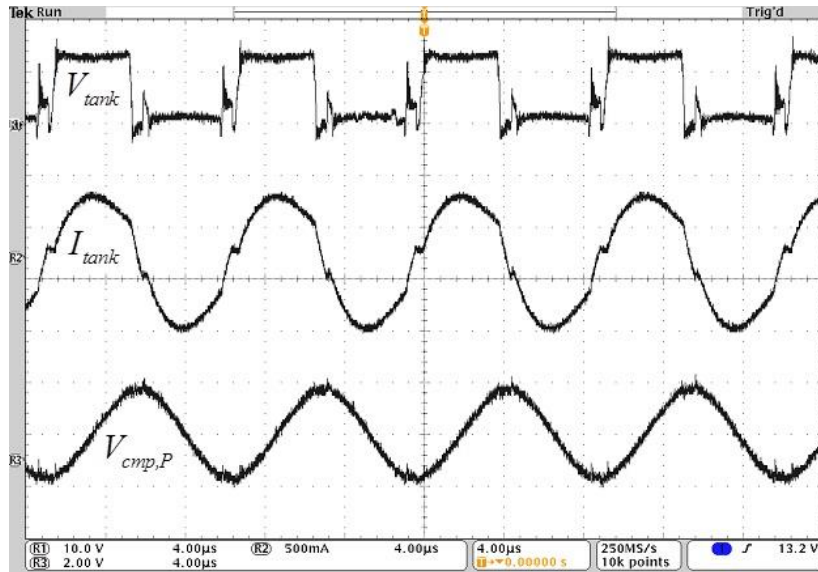


Fig. 5.3. Measured voltage waveforms across the resonant tank (upper trace, 10 V/div) and compensating capacitor (lower trace, 2 V/div), and the current waveforms (middle trace, 500 mA/div) through the resonant tank at time scale of 4 μ s/div.

5.3.2 Testing of the Frequency Tracking Unit

The external circuit of the PLL chip is initially adjusted to ensure that the center frequency is equal to the resonant frequency when the secondary coil is best aligned. By varying the phase difference between two inputs, the VCO output frequency is measured to test the property of the PLL circuit. The characteristic curve is shown in Fig. 5.4, indicating that the center frequency is 106 kHz and the frequency tracking range is from 62.2 to 157.8 kHz.

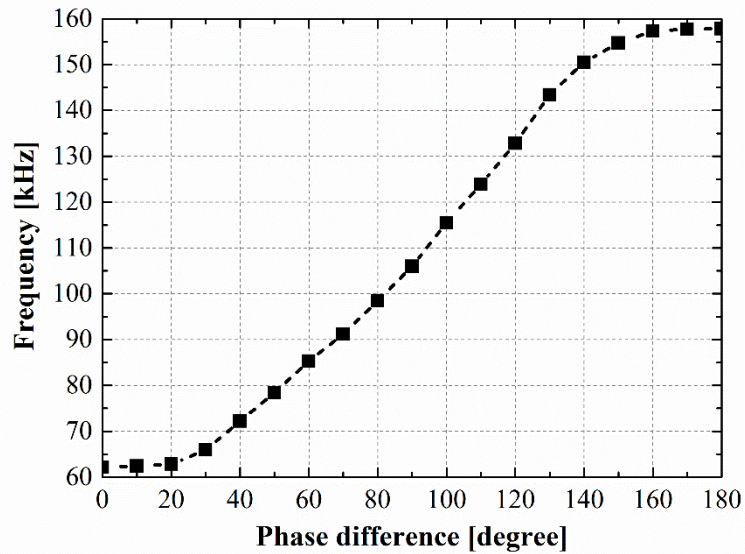


Fig. 5.4. The VCO output frequency versus the phase difference between input voltages.

When the distance between the primary coil and the secondary coil increases, the resonant frequency of the system changes to be higher. The resonant frequency tracking unit tries to tune the operating frequency following the change of the resonant frequency. The tracking of the resonant frequency tracking unit is shown in Fig. 5.5, with the 7.6% maximum difference at the separation distance of 9 cm.

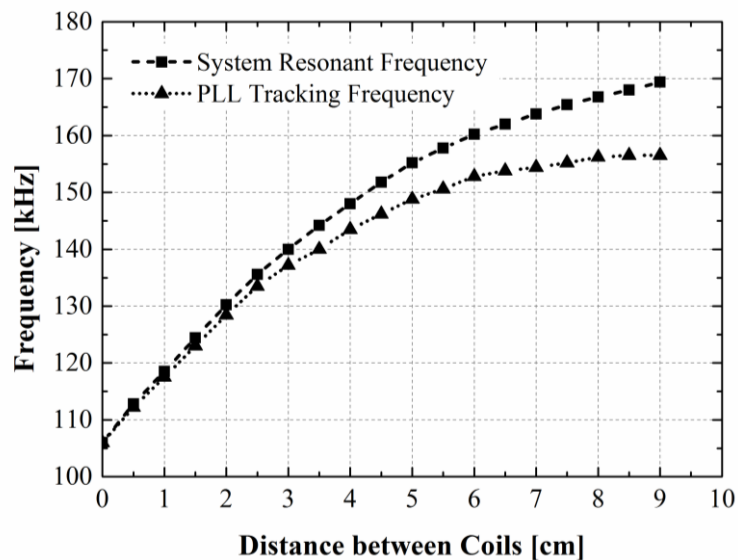


Fig. 5.5. The resonant frequency and the tracking frequency versus the coil distance.

5.3.3 Testing of the Secondary Circuit

In the secondary circuit, the induced AC voltage across the secondary coil, $V_{coil,S}$, is rectified by the full-wave rectifier and converted to a constant and stable 5 V DC voltage V_{out} . The waveforms of these two voltages are measured and shown in Fig. 5.6.

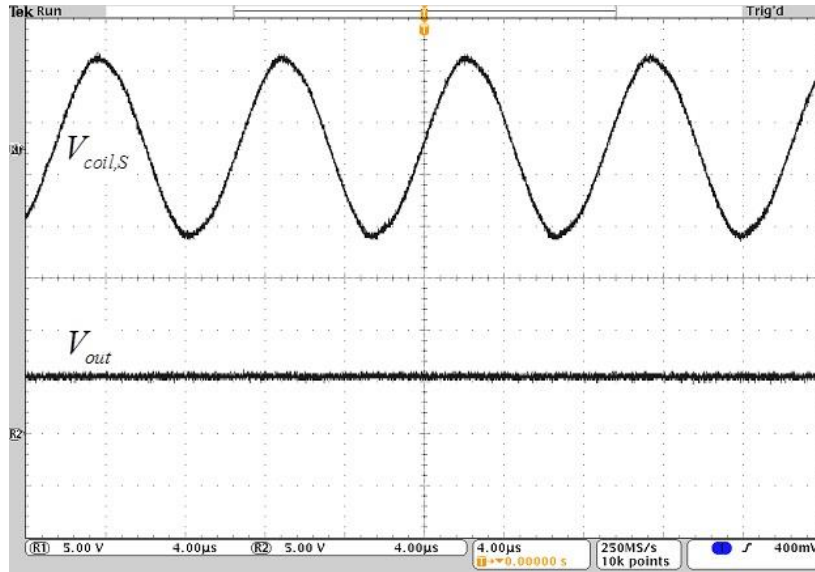


Fig. 5.6. Measured AC voltage across the secondary coil (upper trace, 5 V/div) and DC voltage across the output of DC/DC converter (lower trace, 5 V/div) at the time scale of 4 μ s/div.

5.4 Efficiency of the IPT System

The overall power transfer efficiency η_o of an IPT system is an end-to-end efficiency from the DC power supply to the load, defined as the ratio of the power consumed by the load to the power supplied by the source. The coupling efficiency η_c is from the primary coil to the secondary coil, defined as the ratio of the output power of the secondary coil to the input power of the primary coil. η_o and η_c are expressed as follows:

$$\eta_o = \frac{P_{load}}{P_{source}}, \quad (5.1)$$

$$\eta_c = \frac{P_s}{P_p}. \quad (5.2)$$

Factors which influence the overall power transfer efficiency are the efficiency of the half-bridge circuit and resonant tank, the efficiency of the coupling, and the efficiency of the secondary circuit. Among them, the coupling efficiency is the key factor which determines the overall power transfer efficiency, especially when the distance between the primary and secondary coil increases. These two efficiencies are measured at varying distance between the primary and secondary coil as shown in Fig. 5.7.

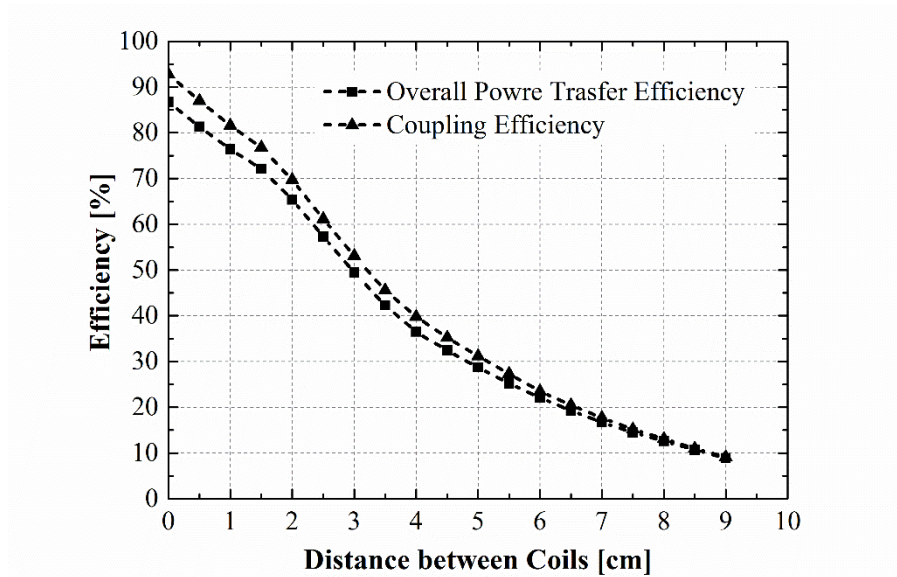


Fig. 5.7. The coupling efficiency and the overall power transfer efficiency versus the coil distance.

The results show that the highest coupling efficiency is 93% and the highest overall power transfer efficiency is 87%, where the two coils are placed closely without gap. The workable distance is up to 8.6 cm between the primary coil and the secondary coil with a power transfer efficiency of 10%.

5.5 Evaluation of the IPT System

The load power at different coil distances are measured and plotted in Fig. 5.8. When the distance between two coils is 0, the output voltage from the DC/DC converter is 5 V, and the current through the load is 1 A. As the distance increases, the 5 W load power is maintained until the increasing current in the primary circuit reaches its limitation of 2.8 A. This current limitation is determined by the permissible rms current of 3.0 A through the primary compensating capacitor at 100 kHz and 85 °C [79]. From 6.5 cm, the output voltage begins to drop, as well as the load power. The minimum load power measured is about 1.5 W at 9 cm.

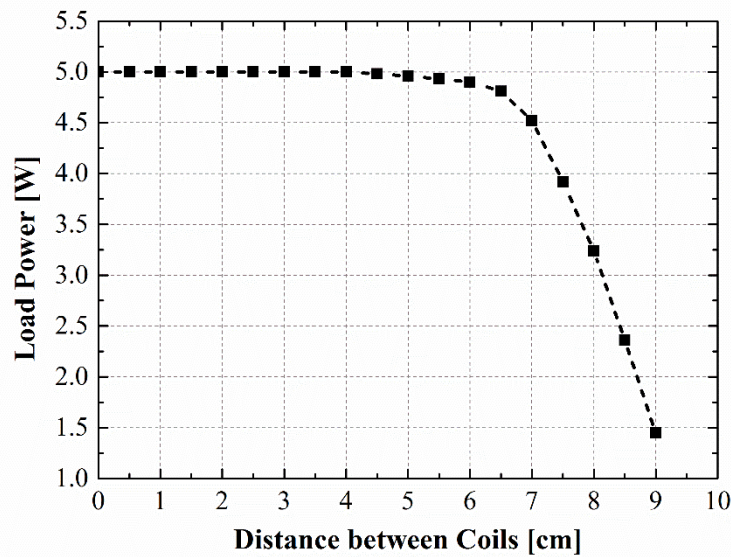


Fig. 5.8. Load power versus the distance between two coils.

Fig. 5.9 gives performance comparison between the proposed IPT system and other related works on the maximum power transfer efficiency and the transmission distance ratio, which is the ratio of the maximum transmission distance (8.6 cm) to the coil equivalent dimension (5.9 cm). The proposed IPT with a maximum efficiency of 87% and the transmission distance ratio of 1.46 shows a relatively high performance compared to other works cited. This also

verifies that the proposed IPT system is effective enough for portable device charging.

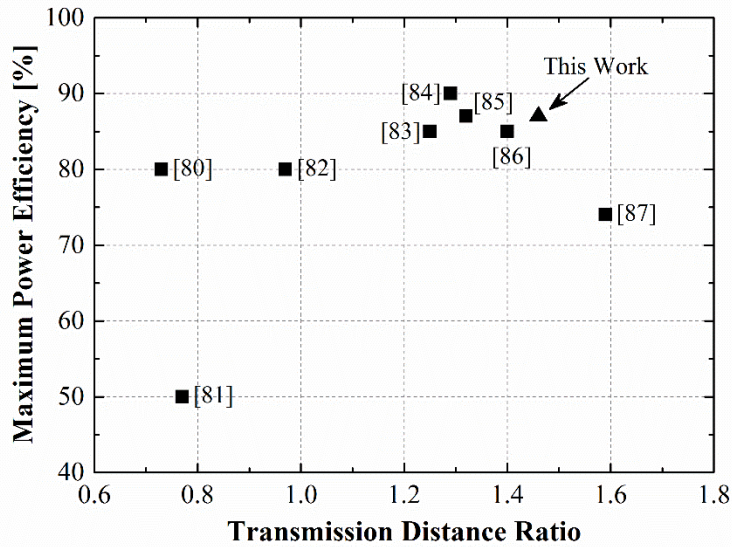


Fig. 5.9. The comparison of the maximum power efficiency and transmission distance ratio with related works from [80]-[87].

5.6 Summary

In this chapter, tests and measurements on the proposed IPT system is performed and the results are recorded and analyzed. The primary and secondary sides of the IPT system are built on two separate boards respectively with control circuits on PCB and high-current circuits on busbar outside the PCB. When the coil distance is 0, at the resonant frequency of 106 kHz, 5 V DC voltage is obtained across the 5 Ω resistive load with the maximum coupling efficiency of 93% and the maximum overall power transfer efficiency of 87%. As the distance increases, the load power is maintained constant at 5 W and drops after the increasing current in the resonant tank reaches the limitation. At the separation of 9 cm, both the coupling efficiency and overall efficiency decrease below 10% and the frequency tracking difference is 7.6%. If we define the maximum transmission distance as that where the overall efficiency reduce

to 10%, the transmission distance ratio, which is the ratio of the maximum transmission distance to the primary coil dimension, is 1.46. The proposed IPT system is bench-marked with other related works to demonstrate its performance in effective power transfer for the charging of portable devices.

Chapter 6

Conclusions and Future Work

6.1 Conclusions

Since the first experiment on wireless power transfer conducted in the beginning of 20th century, research interest in near-field and far-field wireless power transfer continued through the whole century. As portable electronic and communication devices mushroom at the turn of the 20th century, wireless power transfer as a novel charging technology is applied due to many advantages. Inductive power transfer as one of the wireless charging methods is widely investigated to improve its power transfer efficiency.

Theoretical analysis is conducted in Chapter 2. Based on electromagnetic laws and circuit models using reflected impedance, the key component of IPT systems, coupled inductors, is analyzed. It is necessary to implement compensating capacitors, including SS, SP, PS and PP, for primary and secondary inductors and operate at the only resonant frequency of the system to achieve maximum power transfer efficiency and minimum VA rating of the supply.

The high-Q resonant coil is designed in Chapter 3. The topology of alternately stacked C-shaped conductor layers and toroid-shaped dielectric layers is adopted to overcome the disadvantages of litz wire at high frequencies. Based on the current distribution by simulations, the lumped circuit model for the defined unit structure is established and used as a basic component for stack

model. The function of resonant frequency is derived and verified by both simulations and experiments. A 16-unit, 8-section prototype with a measured Q of 1200 at the resonant frequency of 550 kHz is finally chosen for the IPT system.

The IPT system is designed in Chapter 4. Energy from the DC power supply at the primary side is converted by the half-bridge circuit to a high-frequency magnetic field coupling the primary and secondary coils. The induced AC voltage at the secondary side is converted to the DC voltage by the full-wave rectifier and regulated by the DC/DC converter for the constant and stable 5 V output. The frequency tracking unit adjusts the operating frequency to follow the varying resonant frequency to maintain resonant status. The standby unit reduces the system power consumption when the secondary coil is absent.

The IPT system is tested in Chapter 5. Building on two separate PCBs, 5 W power can be transferred at the maximum transmission distance of 6.5 cm for the highest overall power transfer efficiency of 87% at the resonant frequency of 106 kHz. The proposed IPT system with the transmission ratio of 1.46 is bench-marked with other related works to demonstrate its performance in effective power transfer for the charging of portable devices.

6.2 Future Work

Recommendations for future work are listed as follows.

- 1) For coil fabrication, use dielectric materials with higher relative permittivity adhesive with higher relative permittivity instead of glue. More layers to reduce the value of compensating capacitor.

- 2) Build 3D physical model for the high-Q resonant coil and simulate using finite element method to examine the current and flux distribution within the coil for a more accurate calculation of inductance, capacitance, resonant frequency and Q.
- 3) Adopt soft switching technology, ZVS or ZCS, instead of hard switching to increase the operating frequency and improve the overall efficiency by reducing the switching losses.
- 4) Use circuit components and PCB route with high-current rating for higher output power and current to charge tablets or laptop computers.

References

- [1] H. W. Secor, "Tesla apparatus and experiments—How to build both large and small Tesla and Oudin coils and how to carry on spectacular experiments with them," *Practical Electricians*, Nov. 1921.
- [2] W. C. Brown, "The history of wireless power transmission," *Solar Energy*, vol. 56 (1), pp. 3-21, 1996.
- [3] M. Budhia, J. T. Boys, G. A. Covic, and C. Y. Huang, "Development of a Single-Sided Flux Magnetic Coupler for Electric Vehicle IPT Charging Systems," *IEEE Trans. Ind. Electron.*, vol. 60, pp. 318-328, Jan. 2013.
- [4] M. Budhia, G. Covic, and J. Boys, "A New IPT Magnetic Coupler for Electric Vehicle Charging Systems," in *Proc. IEEE 36th Ind. Electron. Conf.*, Glendale, AZ, 2010, pp. 2487-2492.
- [5] U. K. Madawala and D. J. Thrimawithana, "A Bidirectional Inductive Power Interface for Electric Vehicles in V2G Systems," *IEEE Trans. Ind. Electron.*, vol. 58, pp. 4789-4796, Oct. 2011.
- [6] K. Sugimori, H. Sakamoto, and K. Harada, "A one-converter contactless charger for electric vehicles," *Elect. Eng. in Japan*, vol. 132, pp. 73-81, Jul. 2000.
- [7] I. S. Suh and J. Kim, "Electric Vehicle On-Road Dynamic Charging System with Wireless Power Transfer Technology," in *Proc. IEEE Int. Electric Mach. Drives Conf.*, Chicago, IL, 2013, pp. 234-240.
- [8] C. S. Wang, O. H. Stielau, and G. A. Covic, "Design considerations for a contactless electric vehicle battery charger," *IEEE Trans. Ind. Electron.*, vol. 52, pp. 1308-1314, Oct. 2005.
- [9] S. C. Yang, S. Z. Song, Y. G. Cao, W. Z. Gou, and F. Z. Ji, "Research on Efficiency of High Power Resonant Electric Vehicle Contactless Power Transfer Charger," *Advances in Mech. Eng.*, vol. 2014, pp. 1-8, 2014.
- [10] C. Zheng, R. Chen, E. Faraci, Z. U. Zahid, M. Senesky, D. Anderson, *et al.*, "High Efficiency Contactless Power Transfer System for Electric Vehicle Battery Charging," in *Proc. IEEE ECCE*, Denver, CO, 2013, pp. 3243-3249.
- [11] Y. L. Ban, J. H. Chen, J. L. W. Li, and W. Hu, "Printed wideband notched antenna for wireless USB dongle attached to laptop computer," *J. of Electromagn. Waves Applicat.*, vol. 27, pp. 257-266, Jan. 2013.
- [12] S. Pu and H. T. Hui, "A New Definition of Power Transmission Efficiency for Wireless Charging Systems by Using Coil Arrays," in *Proc. IEEE APSURSI*, Orlando, FL, 2013, pp. 1434-1435.
- [13] V. Boscaino, F. Pellitteri, L. Rosa, and G. Capponi, "Wireless battery

- chargers for portable applications: design and test of a high-efficiency power receiver,” *IET Power Electron.*, vol. 6, pp. 20-29, 2013.
- [14] M. Fareq, M. Fitra, M. Irwanto, S. Hasan, and M. Arinal, “Low wireless power transfer using Inductive Coupling for mobile phone charger,” in *Proc. Int. Conf. Sci. Engi. Math., Chemistry Physics*, 2014, vol. 495.
- [15] M. Fareq, M. Fitra, M. Irwanto, H. S. Syafruddin, N. Gomesh, S. Farrah, *et al.*, “Solar wireless power transfer using inductive coupling for mobile phone charger,” in *Proc. IEEE 8th Int. PEOCO*, Langkawi, 2014, pp. 473-476.
- [16] S. Y. R. Hui and W. W. C. Ho, “A new generation of universal contactless battery charging platform for portable consumer electronic equipment,” *IEEE Trans. Power Electron.*, vol. 20, pp. 620-627, May 2005.
- [17] C. G. Kim, D. H. Seo, J. S. You, J. H. Park, and B. H. Cho, “Design of a contactless battery charger for cellular phone,” *IEEE Trans. Ind. Electron.*, vol. 48, pp. 1238-1247, Dec. 2001.
- [18] L. Olvitz, D. Vinko, and T. Svedek, “Wireless power transfer for mobile phone charging device,” in *Proc. IEEE 35th Int. Conv. MIPRO*, Opatija, 2012, pp. 141-145.
- [19] R. Selvakumaran, W. Liu, B. H. Soong, L. Ming, and S. Y. Loon, “Design of Inductive Coil for Wireless Power Transfer,” in *Proc. IEEE/ASME Int. Adv.Intell. Mechatron. Conf.*, Singapore, 2009, pp. 584-589.
- [20] X. Zhang, S. L. Ho, and W. N. Fu, “Quantitative Design and Analysis of Relay Resonators in Wireless Power Transfer System,” *IEEE Trans. Magn.*, vol. 48, pp. 4026-4029, Nov. 2012.
- [21] X. Zhu, X. D. Zhang, and Q. Y. Wu, “Wireless charging system based on switched beam smart antenna technique,” In *Proc. IEEE Int. Symp. Microwave, Antenna, Propag. Emc Tech. for Wireless Commun.*, Hangzhou, 2007, pp. 486-489.
- [22] Y. T. Jang and M. M. Jovanovic, “A contactless electrical energy transmission system for portable-telephone battery chargers,” *IEEE Trans. Ind. Electron.*, vol. 50, pp. 520-527, Jun. 2003.
- [23] S. Y. Hui, “Planar Wireless Charging Technology for Portable Electronic Products and Qi,” *Proc. IEEE*, vol. 101, no. 6, pp. 1290-1301, Jun. 2013.
- [24] T. Zink, F. Maker, R. Geyer, R. Amirtharajah, and V. Akella, “Comparative life cycle assessment of smartphone reuse: repurposing vs. refurbishment,” *Int. J. Life Cycle Assessment*, vol. 19, pp. 1099-1109, May 2014.
- [25] Wireless Power Consortium. (2015). [Online]. Available: <http://www.wirelesspowerconsortium.com/>.
- [26] Pike Research. (2012, July 5). *Energy star, google and facebook will*

- help to boost wireless power to \$15.6bn by 2020, Pike says [Online]. Available: <http://www.environmentalleader.com/2012/07/05/energy-star-google-and-facebook-will-help-to-boost-wireless-power-to-15-6bn-by-2020-pike-says/>.
- [27] X. Liu and S. Y. R. Hui, "Optimal design of a hybrid winding structure for planar contactless battery charging platform," *IEEE Trans. Power Electron.*, vol. 23, pp. 455-463, Jan. 2008.
- [28] W. X. Zhong, X. Liu, and S. Y. R. Hui, "A Novel Single-Layer Winding Array and Receiver Coil Structure for Contactless Battery Charging Systems With Free-Positioning and Localized Charging Features," *IEEE Trans. Ind. Electron.*, vol. 58, pp. 4136-4144, Sep. 2011.
- [29] U. M. Jow and M. Ghovanloo, "Geometrical Design of a Scalable Overlapping Planar Spiral Coil Array to Generate a Homogeneous Magnetic Field," *IEEE Trans. Magn.*, vol. 49, pp. 2933-2945, Jun. 2013.
- [30] R. Haldi, K. Schenk, I. Nam, and E. Santi, "Finite-Element-Simulation-Assisted Optimized Design of an Asymmetrical High-Power Inductive Coupler with a Large Air Gap for EV Charging," in *Proc. IEEE ECCE*, Denver, CO, 2013, pp. 3635-3642.
- [31] M. Chigira, Y. Nagatsuka, Y. Kaneko, S. Abe, T. Yasuda, and A. Suzuki, "Novel Core Structure and Iron-Loss Modeling for Contactless Power Transfer System of Electric Vehicle," *Elect. Eng. in Japan*, vol. 184, pp. 61-70, Jul. 2013.
- [32] A. Zaheer, H. Hao, G. A. Covic, and D. Kacprzak, "Investigation of Multiple Decoupled Coil Primary Pad Topologies in Lumped IPT Systems for Interoperable Electric Vehicle Charging," *IEEE Trans. Power Electron.*, vol. 30, pp. 1937-1955, Apr. 2015.
- [33] R. Carta, J. Thone, and R. Puers, "A wireless power supply system for robotic capsular endoscopes," *Sensors and Actuators a-Physical*, vol. 162, pp. 177-183, Aug. 2010.
- [34] B. M. Song, R. Kratz, and S. Gurol, "Contactless inductive power pickup system for Maglev applications," in *Proc. IEEE Ind. Applicat. Conf.*, Pittsburgh, PA, 2012, pp. 1586-1591.
- [35] A. Abdolkhani, A. P. Hu, and N. K. C. Nair, "A Double Stator Through-hole Type Contactless Slipping for Rotary Wireless Power Transfer Applications," *IEEE Trans. Energy Conv.*, vol. 29, pp. 426-434, Jun. 2014.
- [36] C. Park, S. Lee, G. H. Cho, and C. T. Rim, "Innovative 5-m-Off-Distance Inductive Power Transfer Systems With Optimally Shaped Dipole Coils," *IEEE Trans. Power Electron.*, vol. 30, pp. 817-827, Feb. 2015.
- [37] J. Achterberg, E. A. Lomonova, and J. de Boeij, "Coil array structures compared for contactless battery charging platform," *IEEE Trans.*

- Magn.*, vol. 44, pp. 617-622, May 2008.
- [38] M. Budhia, G. A. Covic, and J. T. Boys, "Design and Optimization of Circular Magnetic Structures for Lumped Inductive Power Transfer Systems," *IEEE Trans. Power Electron.*, vol. 26, pp. 3096-3108, Nov. 2011.
- [39] W. Chen, D. Zhao, Z. J. Bai, G. H. Bruck, P. Jung, S. Kang, *et al.*, "Optimization Spatial Multiple Coil Transmitter Structure for Wireless Power Transfer," in *Proc. IEEE APSURSI*, Orlando, FL, 2013, pp. 854-855.
- [40] R. Bosshard, J. Muhlethaler, J. W. Kolar, and I. Stevanovic, "Optimized magnetic design for inductive power transfer coils," in *Proc. IEEE 28th Annual APEC*, Long Beach, CA, 2013, pp. 1812-1819.
- [41] H. T. Hui, S. Pu, and M. C. A. Loong, "Improving the Transfer Efficiency of a Wireless Energy Transfer System Using Multiple Coils," *Energy Develop., Pts 1-4*, vol. 860-863, pp. 2275-2278, 2014.
- [42] D. Kurschner, C. Rathge, and U. Jumar, "Design Methodology for High Efficient Inductive Power Transfer Systems With High Coil Positioning Flexibility," *IEEE Trans. Ind. Electron.*, vol. 60, pp. 372-381, Jan. 2013.
- [43] W. S. Lee, W. I. Son, K. S. Oh, and J. W. Yu, "Contactless Energy Transfer Systems Using Antiparallel Resonant Loops," *IEEE Trans. Ind. Electron.*, vol. 60, pp. 350-359, Jan. 2013.
- [44] X. Z. Shi, C. Qi, M. L. Qu, S. L. Ye, G. F. Wang, L. L. Sun, *et al.*, "Effects of coil shapes on wireless power transfer via magnetic resonance coupling," *J. of Electromagn. Waves and Applicat.*, vol. 28, pp. 1316-1324, Jul. 2014.
- [45] B. H. Waters, B. J. Mahoney, G. Lee, and J. R. Smith, "Optimal Coil Size Ratios for Wireless Power Transfer Applications," in *Proc. IEEE ISCAS*, Melbourne VIC, 2014, pp. 2045-2048.
- [46] S. Wielandt and N. Stevens, "Influence of Magnetic Design Choices on the Quality Factor of Off-the-Shelf Wireless Power Transmitter and Receiver Coils," in *Proc. 2013 IEEE WPT*, Perugia, 2013, pp. 151-154.
- [47] D. C. Ng, C. Boyd, S. Bai, G. Felic, M. Halpern, and E. Skafidas, "High-Q flexible spiral inductive coils," in *Proc. Electromagn. Compatibility Symp.* Melbourne, VIC, 2010, pp. 1-4.
- [48] Y. H. Pai, Z. Y. Yan, and P. H. Fu, "Enhanced saturation magnetization of Fe₃Si nanodot-embedded Fe₈₀Si₁₇Nb₃ flexible film for efficient wireless power transfer," *Materials Chemistry Physics*, vol. 140, pp. 570-574, Jul. 2013.
- [49] J. E. James, D. J. Robertson, and G. A. Covic, "Improved AC Pickups for IPT Systems," *IEEE Trans. Power Electron.*, vol. 29, pp. 6361-6374, Dec. 2014.
- [50] J. Lee, Y. S. Lim, W. J. Yang, and S. O. Lim, "Wireless Power Transfer

- System Adaptive to Change in Coil Separation,” *IEEE Trans. Antennas Propag.*, vol. 62, pp. 889-897, Feb. 2014.
- [51] D. J. Thrimawithana and U. K. Madawala, “A Three-Phase Bi-Directional IPT System for Contactless Charging of Electric Vehicles,” in *Proc. IEEE ISIE*, Gdansk, 2011, pp. 1957-1962.
- [52] Q. W. Zhu, L. F. Wang, and C. L. Liao, “Compensate Capacitor Optimization for Kilowatt-Level Magnetically Resonant Wireless Charging System,” *IEEE Trans. Ind. Electron.*, vol. 61, pp. 6758-6768, Dec. 2014.
- [53] R. Azambuja, V. J. Brusamarello, S. Haffner, and R. W. Porto, “Full Four Capacitor Circuit Compensation for Inductive Power Transfer,” in *Proc. IEEE Int. Instrumentation and Measurement Technol. Conf.*, Minneapolis, MN, 2013, pp. 183-187.
- [54] B. Gu, J. Dominic, B. F. Chen, L. H. Zhang, and J. S. Lai, “Hybrid Transformer ZVS/ZCS DC-DC Converter With Optimized Magnetics and Improved Power Devices Utilization for Photovoltaic Module Applications,” *IEEE Trans. Power Electron.*, vol. 30, pp. 2127-2136, Apr. 2015.
- [55] S. Hussmann and A. P. Hu, “Power efficiency improvement of a contactless power supply for moving sensors using a soft switched detuning technique,” in *Proc. 6th IPEC*, 2003, pp. 947-951.
- [56] Z. Pantic, S. Bai, and S. M. Lukic, “ZCS LCC-Compensated Resonant Inverter for Inductive-Power-Transfer Application,” *IEEE Trans. Ind. Electron.*, vol. 58, pp. 3500-3510, Aug. 2011.
- [57] C. Sen Tang, Y. Sun, Y. G. Su, S. K. Nguang, and A. P. Hu, “Determining Multiple Steady-State ZCS Operating Points of a Switch-Mode Contactless Power Transfer System,” *IEEE Trans. Power Electron.*, vol. 24, pp. 416-425, Jan-Feb. 2009.
- [58] X. Ju, L. Dong, X. Huang, and X. Liao, “Switching technique for inductive power transfer at high-Q regimes,” *IEEE Trans. Ind. Electron.*, vol. 62, pp. 2164-2173, Apr. 2015.
- [59] S. Hasanzadeh and S. Vaez-Zadeh, “Efficiency analysis of contactless electrical power transmission systems,” *Energy Convers. Manag.*, vol. 65, pp. 487-496, Jan. 2013.
- [60] B. L. Ni, C. Y. Chung, and H. L. Chan, “Design and Comparison of Parallel and Series Resonant Topology in Wireless Power Transfer,” in *Proc. IEEE 8th ICIEA*, Melbourne, VIC 2013, pp. 1832-1837.
- [61] C. S. Wang, G. A. Covic, and O. H. Stielau, “Power transfer capability and bifurcation phenomena of loosely coupled inductive power transfer systems,” *IEEE Trans. Ind. Electron.*, vol. 51, pp. 148-157, Feb. 2004.
- [62] J. I. Agbinya, *Wireless Power Transfer*. Aalborg: River Publishers, 2012.
- [63] B. D. Cullity, *Introduction to Magnetic Materials*, 2nd ed. New York:

- Wiley–IEEE, 2008.
- [64] A. E. Fitzgerald, Jr. Charles Kingsley, and S. D. Umans, *Electric Machinery* 6th ed, New York: McGraw-Hill, 2003.
 - [65] S. Chopra, “Contactless power transfer for electric vehicle charging application,” M.S. thesis, Dept. Elect. Eng., Math. Comput. Sci., Delft Univ. of Tech., Delft, Netherlands, 2011.
 - [66] G. Bertotti, “General-Properties of Power Losses in Soft Ferromagnetic Materials,” *IEEE Trans. Magn.*, vol. 24, pp. 621-630, Jan. 1988.
 - [67] Y. T. Kim, G. W. Cho, and G. T. Kim, “The Estimation Method Comparison of Iron Loss Coefficients through the Iron Loss Calculation,” *J. Elect. Eng. Technol.*, vol. 8, pp. 1409-1414, Nov. 2013.
 - [68] J. Takacs, G. Kovacs, and L. K. Varga, “Modeling the Steinmetz's law for soft steel,” *European Physical Journal-Applied Physics*, vol. 51, Aug. 2010.
 - [69] C. R. Sullivan, and L. Beghou, “Design methodology for a high-Q self-resonant coil for medical and wireless-power applications,” in *Proc. 14th IEEE Workshop Contr. Model. Power Electron. (COMPEL)*, Salt Lake City, UT, 2013, pp. 1-8.
 - [70] Baoyun Ge; Ludois, D.C.; Perez, R., “The use of dielectric coatings in capacitive power transfer systems,” in *Proc. IEEE ECCE*, Pittsburgh, PA, 2014, pp.2193-2199.
 - [71] International Rectifier, “HEXFET power MOSFET,” IRF640N datasheet, Aug. 2010.
 - [72] International Rectifier, “Half-bridge driver,” IR2111 datasheet, Mar. 1999.
 - [73] J. L. Stensby, “Elementary theory and applications,” in *Phase-Locked Loops: Theory and Applications*, Boca Raton: CRC Press, 1997.
 - [74] W. F. Egan, “The basic loop” in *Phase-Lock Basics*, New York: Wiley, c1998.
 - [75] R. E. Best, “Introduction to PLLs,” in *Phase-Locked Loops: Design, Simulation, and Applications*, 5th ed, New York: McGraw-Hill, 2003.
 - [76] Texas Instruments, “CMOS micropower phase-locked loop,” CD4046B datasheet, Jul. 2003.
 - [77] Würth Electronics, “Wireless power charging coil,” WE-WPC Series datasheet, Sep. 2012.
 - [78] Texas Instruments, “LM2576/LM2576HV series SIMPLE SWITCHER® 3 A step-down voltage regulator,” LM2576 datasheet, Jun. 1999 [Revised Apr. 2013].
 - [79] Panasonic, “Film capacitors-caution about safety in use,” ECQE(F) datasheet, Jan. 2015.
 - [80] I. F. Zambari, C. Y. Hui, and R. Mohamed, “Development of Wireless Energy Transfer Module for Solar Energy Harvesting,” in *Proc. 4th Int.*

- Conf. Electr. Eng. Inf. (ICEEI)*, 2013, pp. 882-894.
- [81] Q. W. Yuan, Q. Chen, L. Li, and K. Sawaya, "Numerical Analysis on Transmission Efficiency of Evanescent Resonant Coupling Wireless Power Transfer System," *IEEE Trans. Antennas Propag.*, vol. 58, pp. 1751-1758, May 2010.
- [82] A. O. Di Tommaso, F. Genduso, and R. Miceli, "A Small Power Transmission Prototype for Electric Vehicle Wireless Battery Charge Applications," in *Proc. Int. Conf. Renewable Energy Res.*, Nagasaki, 2012, pp. 1-6.
- [83] S. Hasanzadeh, S. Vaez-Zadeh, and A. H. Isfahani, "Optimization of a Contactless Power Transfer System for Electric Vehicles," *IEEE Trans. Veh. Technol.*, vol. 61, pp. 3566-3573, Oct. 2012.
- [84] H. Takanashi, Y. Sato, Y. Kaneko, S. Abe, and T. Yasuda, "A Large Air Gap 3 kW Wireless Power Transfer System for Electric Vehicles," in *Proc. IEEE ECCE*, Raleigh, NC, 2012, pp. 269-274.
- [85] W. S. Lee, W. I. Son, K. S. Oh, and J. W. Yu, "Contactless Energy Transfer Systems Using Antiparallel Resonant Loops," *IEEE Trans. Ind. Electron.*, vol. 60, pp. 350-359, Jan. 2013.
- [86] T. C. Beh, M. Kato, T. Imura, S. Oh, and Y. Hori, "Automated Impedance Matching System for Robust Wireless Power Transfer via Magnetic Resonance Coupling," *IEEE Trans. Ind. Electron.*, vol. 60, pp. 3689-3698, Sep. 2013.
- [87] J. Huh, S. W. Lee, W. Y. Lee, G. H. Cho, and C. T. Rim, "Narrow-Width Inductive Power Transfer System for Online Electrical Vehicles," *IEEE Trans. Power Electron.*, vol. 26, pp. 3666-3679, Dec. 2011.

List of Publications

1. Q. Li, and Y. C. Liang, “An inductive power transfer system with a high-Q resonant tank for mobile device charging,” *IEEE Trans. Power Electron.*, accepted on Apr. 8th, 2015.
2. Astrid, Q. Li, and Y. C. Liang, “Contactless power delivery for mobile device charging applications”, in *Proc. Int. Conf. Renewable Energy Res.*, Milwaukee, WI, 2014, pp. 659-662.

Appendix

1. Schematic diagram of the IPT system.
2. PCB layout of the IPT system.

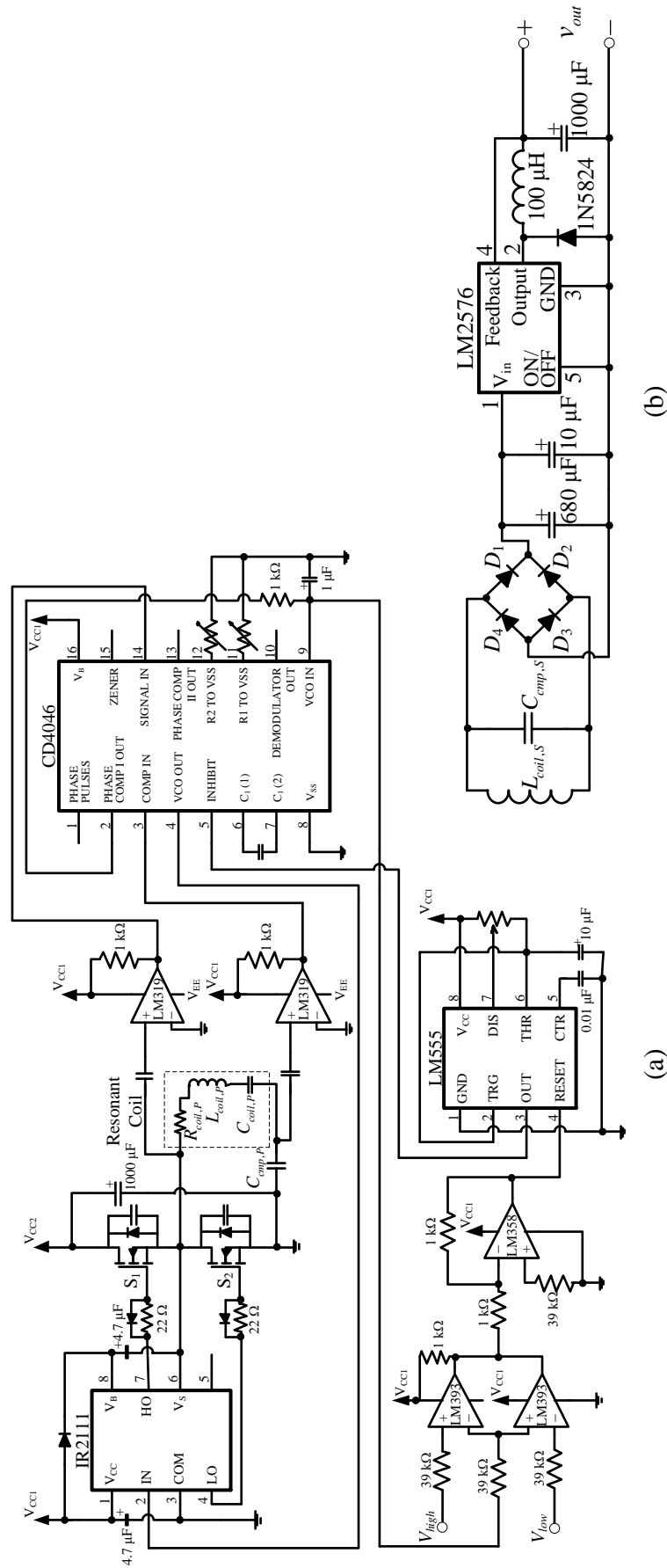
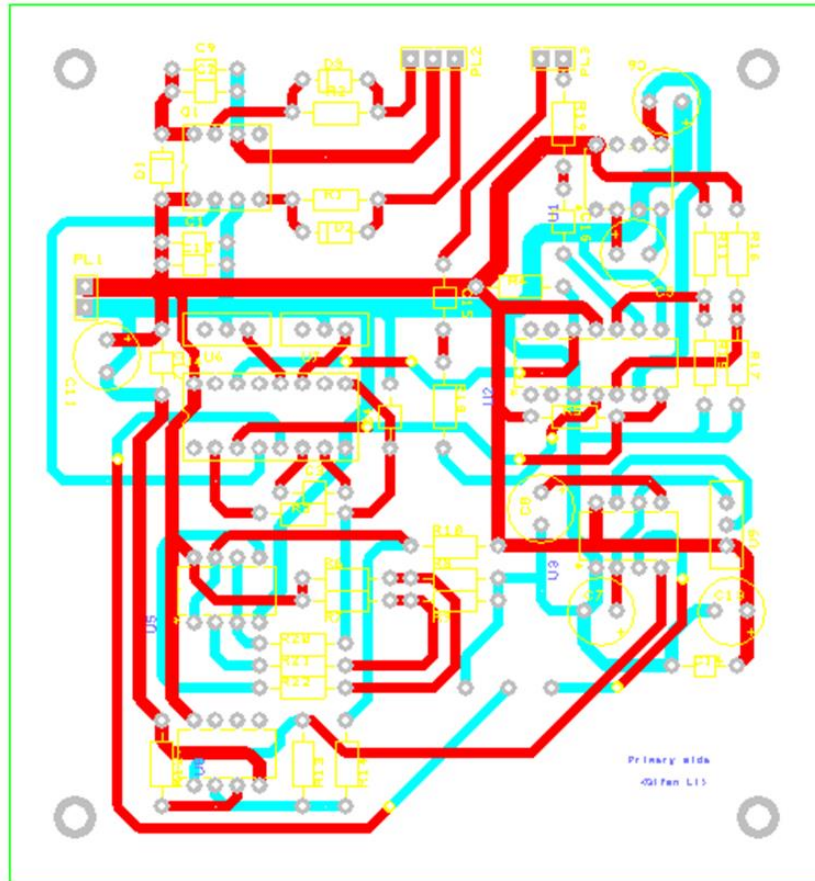
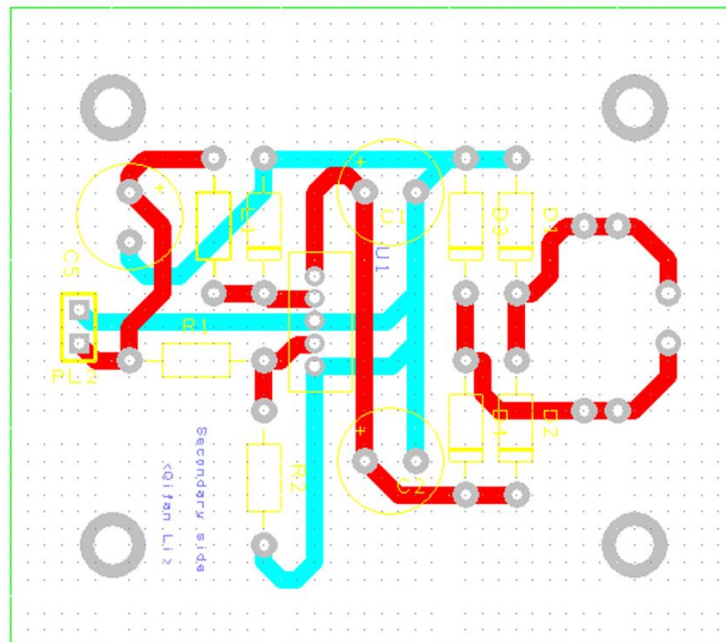


Fig. A.1. Schematic diagram of the IPT system: (a) the primary circuit, and (b) the secondary circuit.



(a)



(b)

Fig. A2. PCB layout of the IPT system: (a) the primary circuit, and (b) the secondary circuit.